TALLINN UNIVERSITY OF TECHNOLOGY
DOCTORAL THESIS
50/2020

$MoSi_2$-based Composites by Selective Laser Melting

TATEVIK MINASYAN

TAL TECH PRESS

TALLINN UNIVERSITY OF TECHNOLOGY
School of Engineering
Department of Mechanical and Industrial Engineering
This dissertation was accepted for the defence of the degree 12/11/2020

Supervisor: Prof. Irina Hussainova
School of Engineering
Tallinn University of Technology
Tallinn, Estonia

Co-supervisor: Dr. Sofiya Aydinyan
School of Engineering
Tallinn University of Technology
Tallinn, Estonia

Opponents: Prof. Olga Kurapova
Department of Physical Chemistry
Institute of Chemistry
Saint Petersburg University
Saint Petersburg, Russia

Prof. Filipe Samuel Silva
School of Engineering
University of Minho
Guimaraes, Portugal

Defence of the thesis: 16/12/2020, Tallinn

Declaration:
Hereby I declare that this doctoral thesis, my original investigation and achievement, submitted for the doctoral degree at Tallinn University of Technology has not been submitted for doctoral or equivalent academic degree.

Tatevik Minasyan

---

signature

European Union
European Regional
Development Fund

Investing
in your future

ISSN 2585-6898 (publication)
ISBN 978-9949-83-633-8 (publication)
ISSN 2585-6901 (PDF)
ISBN 978-9949-83-634-5 (PDF)
Printed by Koopia Niini & Rauam

TALLINNA TEHNIKAÜLIKOOL
DOKTORITÖÖ
50/2020

Selektiivse lasersulatuse teel valmistatud $MoSi_2$ baasil komposiidid

TATEVIK MINASYAN

TAL TECH
KIRJASTUS

Contents

List of publications

I. **Minasyan, T.**, Aghayan, M., Liu, L., Aydinyan, S., Kollo, L., Hussainova, I., & Rodríguez, M. A. (2018). Combustion synthesis of $MoSi_2$ based composite and selective laser sintering thereof. Journal of the European Ceramic Society, 38(11), 3814-3821.

II. **Minasyan, T**., Liu, L., Holovenko, Y., Aydinyan, S., & Hussainova, I. (2019). Additively manufactured mesostructured $MoSi_2$-Si_3N_4 ceramic lattice. Ceramics International, 45(8), 9926-9933.

III. **Minasyan, T.**, Aydinyan, S., Liu, L., Volubujeva, O., Toyserkani, E., & Hussainova, I. (2020). Mo $(Si_{1-x},Al_x)_2$-based composite by reactive laser powder-bed fusion. Materials Letters, 128776.

IV. **Minasyan, T.**, Aydinyan, S., Toyserkani, E., & Hussainova, I. (2020). In Situ $Mo(Si,Al)_2$-based composite through selective laser melting of a $MoSi_2$-30 wt.% AlSi10Mg mixture. Materials, 13(17), 3720.

V. **Minasyan, T.**, Aydinyan, S., Toyserkani, E., Hussainova, I. (2020) Parametric study on in-situ laser powder-bed fusion of $Mo(Si_{1-x},Al_x)_2$. Materials, 13(21), 4849.

Author's contribution to the publications

I. First author. Methodology. Design of experiments. Powder preparation. Conducting experiments. Formal analysis. Data analysis. Discussion of the results. Manuscript preparation

II. First and corresponding author. Methodology. Design of experiments. Powder synthesis. Conducting experiments. Data analysis. Discussion of the results. Manuscript preparation

III. First author. Methodology. Design of experiments. Conducting experiments. Formal analysis. Data analysis. Manuscript preparation.

IV. First and corresponding author. Design of experiments. Conducting experiments. Data analysis. Manuscript preparation.

V. First and corresponding author. Design of experiments. Conducting experiments. Data analysis. Manuscript preparation.

List of publications not included in this thesis

1. **Minasyan, T.**, Liu, L., Aghayan, M., Kollo, L., Kamboj, N., Aydinyan, S., & Hussainova, I. (2018). A novel approach to fabricate Si_3N_4 by selective laser melting. Ceramics International, 44(12), 13689-13694.
2. **Minasyan, T.**, Liu, L., Aydinyan, S., Kollo, L., Aghayan, M., Hussainova, I. (2020). Lattice of $MoSi_2/Si_3N_4$ by selective laser melting. In: EuroPM 2018, Congress and Exhibition, 14-18 October, Bilbao, Spain. European Powder Metallurgy Association. (156875).
3. **Minasyan, T.**, Liu, L., Aghayan, M., Rodriguez, M. A., Aydinyan, S., & Hussainova, I. (2019). Mesoporous fibrous silicon nitride by catalytic nitridation of silicon. Progress in Natural Science: Materials International, 29(2), 190-197.
4. **Minasyan, T.**, Liu, L., Aydinyan, S., Antonov, M., & Hussainova, I. (2019). Selective Laser Melting of Ti/cBN Composite. In Key Engineering Materials (Vol. 799, pp. 257-262). Trans Tech Publications Ltd.
5. **Minasyan, T.**, Kirakosyan, H., Aydinyan, S., Liu, L., Kharatyan, S., & Hussainova, I. (2018). Mo–Cu pseudoalloys by combustion synthesis and spark plasma sintering. Journal of Materials Science, 53(24), 16598-16608.
6. Hussainova, I., **Minasyan, T.**, Liu, L., & Aydinyan, S. (2020, April). ZrC-TiC-$MoSi_2$ ceramic composite by spark plasma sintering. In Journal of Physics: Conference Series (Vol. 1527, No. 1, p. 012028). IOP Publishing.
7. Aydinyan, S., **Minasyan, T.**, Liu, L., Cygan, S., & Hussainova, I. (2019). ZrC Based Ceramics by High Pressure High Temperature SPS Technique. In Key Engineering Materials (Vol. 799, pp. 125-130). Trans Tech Publications Ltd.
8. Liu, L., Aydinyan, S., **Minasyan, T.**, & Hussainova, I. (2020). SHS Produced TiB_2-Si Powders for Selective Laser Melting of Ceramic-Based Composite. Applied Sciences, 10(9), 3283.
9. Liu, L., **Minasyan, T.**, Ivanov, R., Aydinyan, S., & Hussainova, I. (2020). Selective laser melting of TiB_2-Ti composite with high content of ceramic phase. Ceramics International, 21128-21135.
10. Liu, L., **Minasyan, T.**, Kamboj, N., Aydinyan, S., & Hussainova, I. (2020). Bio-inspired TiB_2-TiB-TiN lattices by selective laser melting. Materials Letters, 128337.

Introduction

Additive manufacturing (AM) via selective laser melting (SLM) has matured as a promising technique providing straightforward part fabrication with high level precision and design freedom. SLM adopts a layer-wise production of simple to sophisticated structures, outrunning the conventional manufacturing technologies, such as extruding, molding or assembling. Although the SLM process includes series of steps starting from powder selection and 3D model preparation until the removal of the printed shape; as well as the understanding of complex physics guiding the process sequel, while it is overpowering with the whole basket of advantages, including fast prototyping and production launch, new customized applications, etc. (Patel, 2020; Attaran, 2017).

Powder preparation and respective characteristics are the cornerstones for the SLM process. Self-propagating high-temperature synthesis (SHS), also known as combustion synthesis (CS), is a widely acknowledged energy-saving powder preparation technique, allowing control over the synthesized powders' size and shape by regulating the initial composition of reactive mixture, gas pressure and additives (Minasyan, 2018), thus, ensuring powder viability for the SLM process.

The refractory metal-silicides have attracted plenty of research interest due to promising properties demanded for high temperature structural applications. $MoSi_2$ is a recognized refractory transition metal silicide used for applications ranging from heating elements for high-temperature furnaces to protective coatings (Sundberg, 2004; Zhang, 2019). However, the limited machinability of $MoSi_2$ because of low fracture toughness at room temperature, and severe oxidation above 500^{o}C has narrowed the application field of the material. To overcome these limitations of $MoSi_2$, two main approaches are known: reinforcing $MoSi_2$ with chemically compatible compounds (ZrO_2, WSi_2, TiB_2, Si_3N_4, SiC, etc.) or alloying $MoSi_2$ with metals or alloys (Nb, Cr, Ti, Ta, V, etc.) Using Si_3N_4 as an additive enhances the fracture toughness and high thermal shock resistance of the overall $MoSi_2$-Si_3N_4 composite (Gabrielyan, 2008); alloying $MoSi_2$ with Al leads to formation of $Mo(Si,Al)_2$ (molybdenum aluminosilicide), which increases the oxidation resistance of the material at intermediate and high temperatures, without suppressing its high temperature nature (Sharif, 2001).

Thus, this work focuses on the design and preparation of $MoSi_2$-Si_3N_4 and $Mo(Si,Al)_2$ based composite structures, using the combination of SHS and SLM technologies for powder feedstock and part preparation, respectively.

Accordingly, this thesis reports:

(i) A novel approach for the preparation of $MoSi_2$-Si_3N_4 composites, including selective laser melting of combustion synthesized $MoSi_2$-Si composite powders, and subsequent nitridation;

(ii) The preparation of hexagonal C40 $Mo(Si,Al)_2$-based composites by reactive selective laser melting of $MoSi_2$-AlSi10Mg and Mo-Si-AlSi10Mg powders mixtures;

(iii) Powders and parts characterization along with parametric study aiming at process optimization.

The SLM parametric study considers the laser power and the laser scanning speed as essential variables to establish their influence on microstructure, densification behavior, surface quality and mechanical properties of as-printed parts.

List of abbreviations

Abbreviation	Full Description
bct	Body centered tetragonal
SHS	Self-propagating high-temperature synthesis
SLM	Selective laser melting
SPS	Spark plasma sintering
DIP	Direct inkjet printing
CS	Combustion synthesis
AM	Additive manufacturing
2D	2 dimensional
3D	3 dimensional
3DP	3D printing
MJ	Material jetting
BJ	Binder jetting
SLA	Stereolithography
FDM	Fused deposition modelling
PBF	Powder-bed fusion
DED	Direct energy deposition
LOM	Laminated object manufacturing
SLS	Selective laser sintering
DMLS	Direct metal laser sintering
EBM	Electron beam melting
CAD	Computer aided design
YAG	Yttrium aluminum garnet
SS	Stainless steel
AMC	Aluminum matrix composite
MMC	Metal matrix composite
CBN	Cubic boron nitride
PPM	Pacific particulate materials
BFE	Basic flowability energy
SI	Stability index
CPR-3.5L	Constant pressure reactor -3.5 liters
DSC	Differential scanning calorimetry
TG	Thermogravimetric
EDS	Energy Dispersive X-Ray Spectroscopy
XRD	X-ray diffractometer
SEM	Scanning electron microscope
CT	Computed tomography
LVED	Laser volumetric energy density
HV	Vickers hardness number
ppm	Part per million
rpm	Rotation per minute
sccm	Standard cubic centimeters per minute
wt.%	Weight percentage
at.%	Atomic percentage

List of symbols

Symbol	Explanation
σ_y	Yield strength
σ_u	Ultimate strength
µm	Micrometer
µs	Microsecond
ρ	Density
ρ [◦]	Initial bulk density of the powder
ρ [n]	Packed density
ρ [∞]	Extrapolated powder bulk density
λ	Wavelength
∅	Diameter

1 Review of the literature

1.1 $MoSi_2$ properties, limitations, ways to offset the limitations

The research direction of metal-silicides has always revolved around establishing a material threshold with higher operating temperatures (1100-1500 °C) pertinent to gas turbine components in jet engines and the lucrative aerospace sector (Pan, 2018). Other potential applications include heating elements for combustion furnaces, molten metal plants and the diesel engine spark plugs. The key attributes for those materials are high melting point, strength retention at such operating temperatures and their resistance to creep tension during oxidation (Pan, 2017). $MoSi_2$ is an attractive binary silicide for elevated-temperature structural applications. It has outstanding oxidation resistance (between 1000-1700 °C) and an electrical resistivity that increases proportional to temperature, making it a perfect heating element (Mitra, 2015)*(Fig.1).*

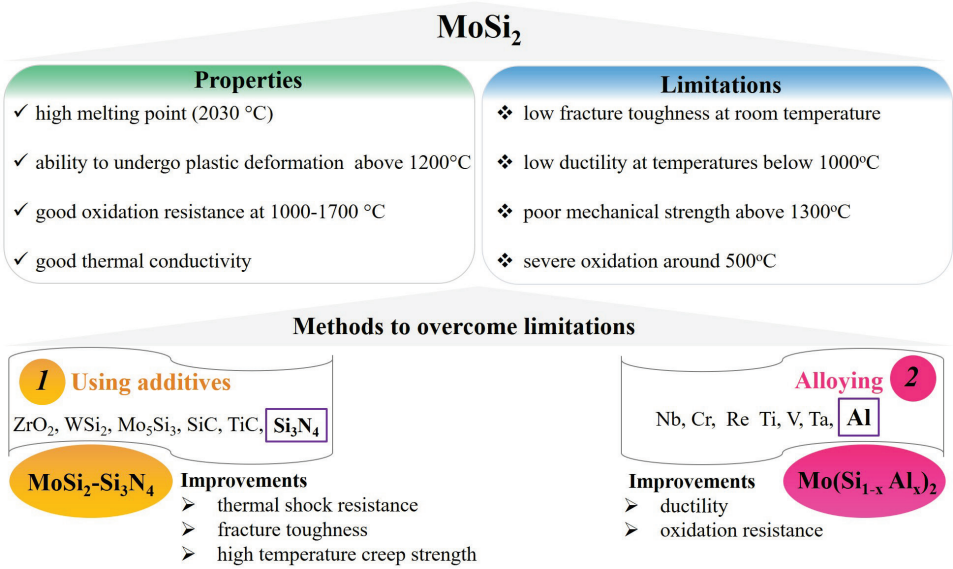

Figure 1. $MoSi_2$: Properties, drawbacks and methods to overcome the limitations.

However, $MoSi_2$ is not readily machinable in regard to its low fracture toughness at room temperature and weak creep resistance above 1200 °C (Sun, 2017a). Moreover, $MoSi_2$ disintegrates (pesting) due to severe oxidation from 500 °C, which restricts the scope of its applications (Nanko, 2001; Vasudevan, 1992).

There are 2 methods to offset $MoSi_2$ limitations:

(i) ***Adding chemically compatible compounds (either ZrO_2, WSi_2, Mo_5Si_3, SiC, TiC, Si_3N_4, etc.)***

(ii) ***Alloying $MoSi_2$ with metals or alloys (Nb, Cr, Re, Ti, V, Ta, Al, etc.) (Fig. 1)***

Method 1- $MoSi_2$ with chemically compatible additives: $MoSi_2$ shows thermodynamic stability when combined with a ceramic reinforcement, including SiC, Si_3N_4, ZrO_2, Al_2O_3, TiC and TiB_2, as a composite. It was reported that creep resistance and fracture toughness of $MoSi_2$ can be remarkably improved when reinforced with SiC, Si_3N_4 and ZrO_2

(Yeh, 2007). Among mentioned additives, **Si_3N_4** has garnered a huge research interest (Kushan, 2012; Hebsur, 2001; Manukyan, 2009); and a wide range of Si_3N_4 additions was found to enhance $MoSi_2$ based material quality.

Method 2- $MoSi_2$ with metallic additives: The body centered tetragonal (bct) structure of C11b $MoSi_2$ is unchanged during minor alloying up to a threshold concentration of 3 at.%, while exceeding the limit of alloying element, the bct structure stability is affected, leading to formation of C40 primitive hexagonal structure. Depending on the atomic radius and electronic structure of the alloying elements, they can substitute either Mo or Si sublattice sites in $MoSi_2$. Alloying $MoSi_2$ with transition metals (W, Nb, Ti, Ta, V, Re, Cr) Mo sites replacement occurs, meanwhile Al with atomic radius proportionate to Si occupies the Si sites (Ingemarsson, 2011; Ghayoumabadi, 2009; Harada, 1998; Wang, 2015). Alloying $MoSi_2$ with aluminum has shown to remarkably improve $MoSi_2$ oxidation resistance at above 500 °C, yielding alumina forming $Mo(Si,Al)_2$, which provides the formation of protective, more stable and adherent Al_2O_3 scale during oxidation. Unlike silica forming $MoSi_2$ based materials, there is no evidence of oxide scale spalling for $Mo(Si,Al)_2$. Moreover, aluminum addition stabilizes the $Mo(Si,Al)_2$ C40 structure and accords a "metallic qualities" to the molybdenum disilicide, improving its ductility (Sharif, 2001; Liu, 2000).

1.2 Synthesis and consolidation methods of $MoSi_2$, $MoSi_2$-Si_3N_4, $Mo(Si,Al)_2$

The rundown of fabrication methods for the synthesis and consolidation of $MoSi_2$, $MoSi_2$-Si_3N_4 and $Mo(Si,Al)_2$ is given in Table 1.

Traditionally, molybdenum disilicide is produced using mechanical alloying (Lee, 1995) (Liu, 1995; Zakeri, 2005), arc melting (Sharif, 2010) and shock synthesis methods (Yen, 1997). Most recently, self-propagating high-temperature synthesis (SHS) was perceived as a promising route for $MoSi_2$ and $MoSi_2$ based composite powders production (Yeh, 2007; Deevi, 1992; Jo, 1996). Self-propagating high-temperature synthesis of $MoSi_2$, when compared to conventional processing techniques, has a favored position being extremely time- and energy-efficient. Consolidation of powdered $MoSi_2$ can be achieved by hot pressing (Cotton, 1991) and additive manufacturing techniques (Hagihara, 2017; Cappi, 2011).

$MoSi_2$-Si_3N_4 composite powder preparation is largely conducted by SHS technique (Gabrielyan, 2008; Manukyan, 2008), meanwhile for consolidation hot pressing (Choe, 1997; Suryanarayana, 2008; Bartlett, 1998; Choi, 1998) and pulse current-activated sintering methods are prevailing (Ko, 2010).

For powdered $Mo(Si,Al)_2$ preparation, SHS is an acknowledged technique (Ghayoumabadi, 2009; Hou, 2016), and for the compaction arc melting (Sharif, 2001; Maruyama, 1997; Stergiou, 1994), hot pressing (Costa e Silva, 1993; Dasgupta, 2007; Ramberg, 2000), spark plasma sintering (Wang, 2015) and other (Nanko, 2001) techniques are used.

Table 1. Fabrication of $MoSi_2$, $MoSi_2$-Si_3N_4 and $Mo(Si,Al)_2$

$MoSi_2$ preparation
Mechanical alloying (Liu, 1995; Zakeri, 2005) ❑ Mechanical alloying of Mo and Si → $MoSi_2$/$MoSi_2$-Mo_5Si_3 → hot pressing **Arc melting** (Sharif, 2010) ❑ Arc melting of Mo and Si → $MoSi_2$ **Shock synthesis** (Yen, 1997) ❑ Prealloyed Mo and Si →shock synthesis→ $MoSi_2$ **Self-propagating high-temperature synthesis (SHS)** ❑ Mo+2Si powder mixture → SHS → $MoSi_2$ powder (Deevi, 1992) ❑ Mo+45.5-66.7 at.% Si powder mixture →SHS →$MoSi_2$/$MoSi_2$-Mo_5Si_3 powder (Jo, 1996) **Hot pressing** (Yeh, 2007; Cotton, 1991) ❑ Arc melting of Mo and Si → $MoSi_2$→ hot pressing **Selective laser melting (SLM)** ❑ $MoSi_2$ powder → SLM → bulk $MoSi_2$ (Hagihara, 2017) **Direct inkjet printing (DIP)** ❑ Aqueous suspension of $MoSi_2$ → Direct inkjet printing → bulk $MoSi_2$ (Cappi, 2011)
$MoSi_2$-Si_3N_4 preparation
SHS ❑ SHS of Mo + 2.4Si mixture under N_2 pressure → $MoSi_2$-Si_3N_4 (Gabrielyan, 2008) ❑ SHS of Mo-5Si-NaCl-Si_3N_4 in N_2 environment → hot pressing (Manukyan, 2008) **Hot pressing** ❑ Ball milled $MoSi_2$-10-40 vol.% Si_3N_4 → hot pressing (Choe, 1997) ❑ Prealloyed $MoSi_2$-Si_3N_4 powder/ball milled Mo and Si and Si_3N_4 → vacuum hot pressing (Suryanarayana, 2008) ❑ SHS $MoSi_2$-10-20 vol% Si_3N_4 → hot pressing/plasma spray processing (Bartlett, 1998) **Pulse current-activated sintering** ❑ Ball milling of Mo_2N and Si → 8$MoSi_2$–Si_3N_4 powder → pulse current-activated sintering (Ko, 2010)
$Mo(Si,Al)_2$ preparation
SHS ❑ SHS of Mo, Si and Al powders → $Mo(Si_{1-x}, Al_x)$ with x= 0-0.5 (Hou, 2016) ❑ SHS of Mo+2(1-x) Si+2xAl (x=0-0.5) → $Mo(Si,Al)_2$ (Ghayoumabadi, 2009) **Arc melting** ❑ Arc melting of Mo, Si, Al → bulk Mo(2at.%Al,Si)$_2$ (Sharif A. A., 2001) ❑ Arc melting of plates of Mo, Si, Al→ C40 $Mo(Si_{1-x},Al_x)_2$ (0.11<x<0.55) (Maruyama, 1997) ❑ Arc melting of Mo, Si, Al→C40 $Mo(Al_{0.5}Si_{0.5})_2$ and the C54 $MoAl_{1.3}Si_{0.7}$ (Stergiou, 1994) **Hot pressing** ❑ Hot pressing of $MoSi_2$+0-8.1 wt.% Al → dense C11 or C40 $Mo(Al,Si)_2$+SiO_2/Al_2O_3 (Costa e Silva, 1993) ❑ Arc melting of Si+Al alloy+hot pressing of Si-Al with Mo → $Mo(Si_{1-x},Al_x)_2$ (x=0-0.1) (Dasgupta, 2007) ❑ SHS of elemental Mo, Si, Al + hot pressing → dense $Mo(Al_x,Si_{1-x})_2$ (Ramberg, 2000) **Spark plasma sintering (SPS)** ❑ SHS of Mo, Si and Al +spark plasma sintering → $Mo(Si_{1-x},Al_x)_2$ (x=0-0.3) (Wang, 2015) **Other** ❑ Dipping Mo plate into Al liquid with saturated Si → Mo covered with $Mo(Si,Al)_2$ (Nanko, 2001)

1.3 Self-propagating high-temperature synthesis (SHS)

Self-propagating high-temperature synthesis (SHS), also recognized as combustion synthesis (CS), is a cutting-edge technique to produce engineering ceramics and refractory materials. The rapid heating and cooling rates during SHS provide a potential to produce materials with unique phase and microstructure features and enhanced properties. SHS is based on the ignition of a powdered material in either atmospheric or an inert environment, leading to a self-supporting exothermic chemical reaction, which provides heat for reaction completion. In this method, the exothermic nature of products' formation reactions provides primary heat source (requiring external heat only for reaction ignition), propelling the production of high-quality materials in a very short period, as the temperature of the combustion can reach up to 4700°C, and the velocity of combustion wave propagation up to 25 $cm \cdot s^{-1}$ (Merzhanov, 2004; Mossino, 2004; Vorotilo, 2018). Usually, in combustion synthesis, the reactants are powdered materials, dry mixed and compressed into a tablet to increase packing density and decrease the heat loss. The tablet is then set in a graphite or metallic boat in the reaction chamber and ignited with a coil either in vacuum, reactive gas or inert atmosphere. The schematic representation of the process is illustrated in Fig. 2. SHS process' advantages, materials and applications are depicted in Fig. 3.

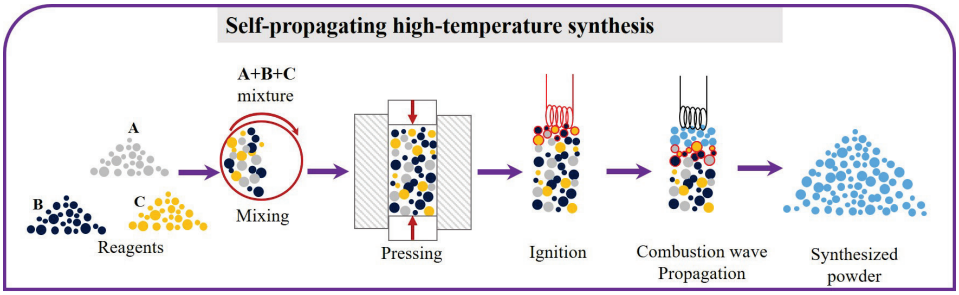

Figure 2. The simplified scheme of self-propagating high-temperature synthesis process.

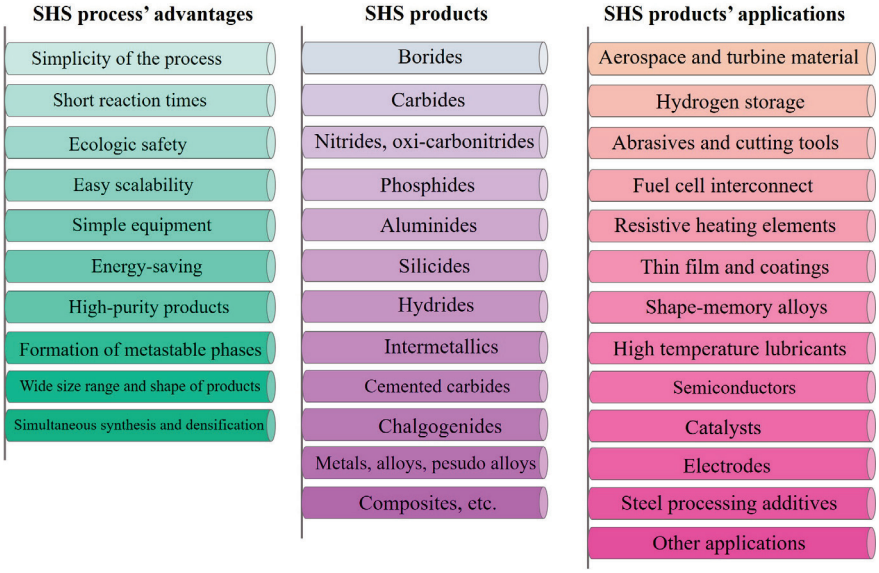

Figure 3. SHS process' advantages, typical SHS produced materials and their applications.

1.4 Additive manufacturing (AM): Selective laser melting (SLM)

Additive manufacturing (AM) is a layer-wise technology enabling the construction of complex shapes generated from digital 3D models. AM technologies have been matured to comply with the demand of printing complex and intricate structures. Fast and cost-effective prototyping, defect minimization and part production with promising properties are the crucial driving factors for the evolution of AM techniques (Guo, 2013; Szost, 2016; Ngo, 2018). The state of industry for 2019 and main benefits of AM are shown in Fig. 4.

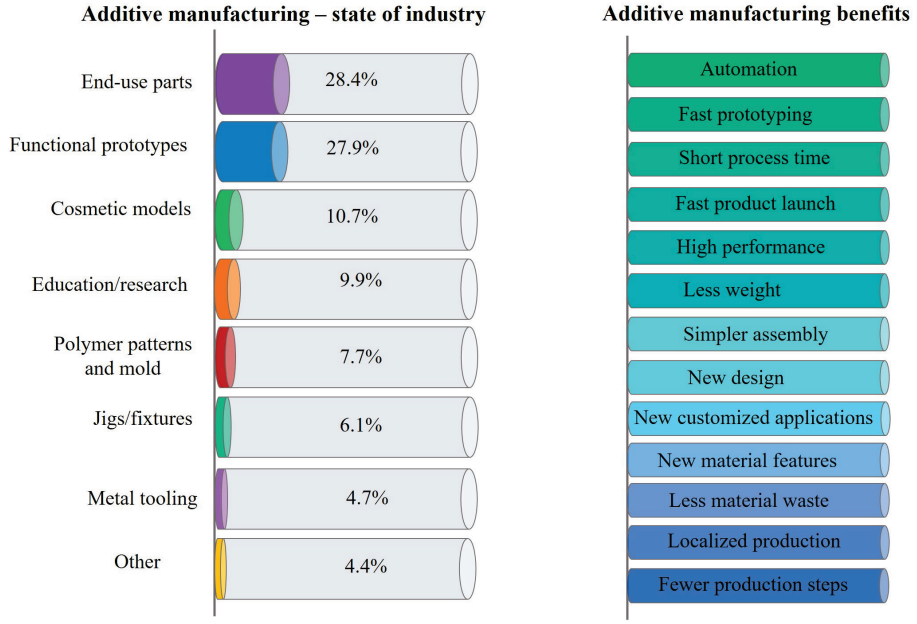

Figure 4. Additive manufacturing state of industry and main benefits (Wohlers Report , 2019), (Attaran, 2017), (Ford, 2016).

AM technology includes seven different types of processes: vat photopolymerization, material jetting (MJ), binder jetting (BJ), fused deposition modelling (FDM) or material extrusion, powder bed fusion (PBF), direct energy deposition (DED) and laminated object manufacturing (LOM) (Pinkerton, 2016; Revilla-León, 2017).

The performance of AM is driven by printing parameters, materials, binding agents and post treatment.

To improve and optimize the AM process performance the following are considered:

1. To tune process parameters accordingly, considering the characteristics of materials. The optimized process parameters will reduce the process variability while enhancing the process performance and reproducibility.
2. To synthesize new materials with distinct desirable properties suitable for additive manufacturing.

Powder bed fusion has 4 subcategories including selective laser melting (SLM), selective laser sintering (SLS), direct metal laser sintering (DMLS) and electron beam melting (EBM) (Prakash, 2018).

In selective laser melting (SLM) a laser in either continuous or pulse mode scans the powders in a predetermined pattern to generate layers with given size and shapes (Salarian, 2020; Patel, 2020). A 3D computer-aided design mathematically slices model

into 2D cross sections, which act as a blueprint for the SLM machine. The roller (or recoater) smoothly distributes a thin powder layer onto the build platform, subsequently, a laser beam precisely melts the powder in a pattern following the execution of the build file from a computer-aided design (CAD) part model. Each lasering sequence forms a novel cross-section slice of the constructed object, the work platform is gradually lowered by a set thickness of a layer, after which a scraper distributes the new portion of free-packed powder (Fig. 5).

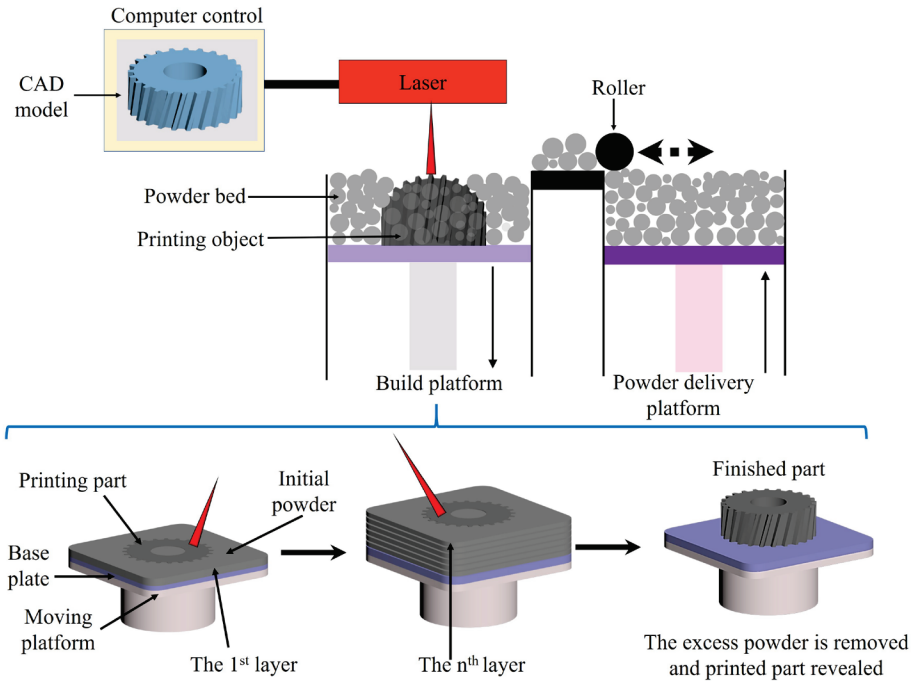

Figure 5. The simplified schematic illustration of selective laser melting process.

The process repeats growing the build layers until the part is complete. The finished object is removed and cleaned from the unused recyclable powder. SLM and SLS (or mainly DMLS) are sister technologies, while in SLM, a relatively high-power Nd:YAG and Yb:YAG - fiber lasers fully melt each layer of powder instead of sintering as in SLS.

The number of processing parameters have an influence on SLM outcome. The microstructural features, physical and mechanical properties of the printed parts rely upon the careful selection of SLM parameters and the starting materials, involving:

(i) laser absorptivity, reflectivity, thermal expansion coefficient, particle size, shape and distribution, powder bed density/packing density, layer slice thickness, powder flowability, powder melting point, chemical composition, thermal conductivity, specific heat (Brandt, 2016; Munir, 2017);

(ii) laser type, laser working mode (continuous or pulse), wavelength, power, radius/effective diameter, beam shape, pulse duration, pulse repetition rate (if pulsed laser is used) (King, 2015);

(iii) scanning speed, scanning strategy, scan raster rotating angle, hatching distance, hatching angle (Jhabvala, 2010);

(iv) powder bed and feeder heating (Aboulkhair, 2014; Munir, 2017),

(v) reaction chamber atmosphere – flooding inert gas type, flow rate, flow direction, gas pressure (Patel, 2020; Sames, 2016);
(vi) build plate type, chemical composition, probable reactiveness with feedstock, thickness (Sames, 2016);
(vii) build file setup: location, orientation, building angle (Esmaeilizadeh, 2019; Simonelli, 2014);
(viii) feedstock recycle (Slotwinski, 2014; Tang, 2015);
(ix) other variables **(Paper V)**

The SLM process has been investigated with numerous metals and alloys for fabricating cellular structured and high-performance parts, including aluminum (Anwar, 2017; Ding, 2017; Delroisse, 2017), stainless steel (Sun, 2016; Zhong, 2016; Yan, 2014), high speed steel (Kempen, 2014; Liu, 2013), titanium (Zhang, 2016; Attar, 2014a), nickel (Harrison, 2015; Yap, 2017), tungsten (Iveković, 2018; Zhou, 2015), as well as high entropy alloys (Luo, 2020; Zhou, 2019), etc. Metal-ceramic composites are mainly produced via SLM by (i) mixing the required individual ceramic and metal components, or (ii) in-situ chemical reactions that yield the desired product. In (Gu, 2012) and (AlMangour, 2016) the SLM fabrication of Ti-TiC and 316L SS-TiC MMCs via SLM with improved wear resistance and microhardness is reported. Manufacturing of almost full dense AlSi10Mg-15 wt.% Al_2O_3 aluminum matrix-oxide ceramic composite by SLM was presented in (Liao, 2019). Al-Fe_2O_3 aluminum matrix composite (AMC) was fabricated in (Dadbakhsh, 2014). Ti-cBN composite with improved mechanical properties was produced via SLM, as described in (Minasyan, 2019). In (Attar, 2014b) it is stated the fabrication of almost fully dense Ti-TiB composite bulks by SLM, starting with Ti-TiB_2 powder. In (Kühnle, 2012) the SLM of a high-energy ball milled Ti-B_4C powder mixture was conducted resulting in the in-situ formation of TiB_2 and TiC. The in-situ formation of metal-ceramic composites holds more promise, in comparison with pre-added compounds, due to better wettability between ceramic and metal in addition with chemical homogeneity of the product.

1.4.1 SLM of ceramics and ceramic based materials

AM technologies have historically been aimed at fabricating polymer or metal-based prototypes. In the recent past, new generation materials have been imported to the global market that cannot be manufactured by other techniques, rather than additively. Ceramic materials have always been a sought-after substitution to polymers or metals for AM. Ceramic materials possess high melting temperature and hardness compared to polymers or metals, and thereby open up multifunctional applications in the AM field, as AM empowers the fabrication of intricate shaped cellular frameworks with a highly restrained dimensional accuracy, target shape and cell sizes, not attained by other techniques used for the manufacturing of full dense bulk or macroporous structures (Zocca, 2015).

In fact, the laser absorptivity of ceramic materials is vulnerable to the laser wavelength (Nd:YAG (λ = 1.06 μm), Yb:YAG (λ = 1.07 μm) and CO_2 fiber laser (λ = 10.6 μm)), as for example, carbides show higher absorbance when lasers with short wavelength are used, while in case of oxide ceramics, the laser absorbance proportionally increases when a long wavelength laser is used (Tolochko, 2000). Moreover, ceramic materials are also innately brittle and possess low fracture toughness, which make them difficult to manufacture, especially for producing parts with complex geometries.

A few industrial ceramics (e.g. oxides, nitrides and diborides), advanced ceramics and biocompatible ceramics have been investigated to be manufactured as net-shaped and dense parts using indirect AM approaches such as FDM, SLS, 3DP and stereolithography (SLA).

However, all these techniques usually result in a green body using excessive organic or inorganic binders. The binder is burnt out and final densification of the part is achieved by conventional sintering way (Guo, 2013).

Direct laser processing of ceramic (ceramic-metal) powders (part build by partial or full melting of the constituents) offers a processing alternative without using binding materials.

SLM is thus far the only 3D printing process allowing single step production of ready-to-use individualized ceramic parts with intricate geometries and good mechanical properties (Deckers, 2014). However, the short exposure of laser during direct melting leads to wide temperature gradient, resultant thermal stresses and rapid thermocapillary flow. As a result, ceramics, unlike metals, defined with poor thermal-shock resistance and thermal conductivity, are prone to cracking. Another problem associated with ceramics is the high viscosity of ceramic melt, as it suppresses the merge of smaller droplets into a larger melt, hindering the consolidation process (Sing, 2017).

One way to circumvent thermal shock and to increase surface tension of the melt and promote the droplet merging, is to preheat powders before SLM, as in the case with dense oxide ceramics. Crack free, almost full density zirconia-alumina composite was achieved by selective laser melting process, when powder was preheated up to 1600 ^{o}C (Wilkes, 2013). Likewise, Al_2O_3 samples with 94% relative density were prepared via SLM, while in case of feedstock preheating up to 1600 ^{o}C for 5h, the relative density of produced part was increased up to 98% (Balla, 2008).

SLM can successfully showcase the advantages of using ceramic-metal composites, as they possess valuable properties sought-after in the aerospace industry, biomedicine, energy generation, etc. The ceramic-metal composites are more tolerant to temperature gradient and their laser absorptivity might be adjusted via proper selection of ceramic-metal pair. Quite a few authors had reported the preparation of ceramic-metal/metalloid composites via selective laser melting technique. For example, Liu. et al. report the successful preparation of TiB_2-Si and TiB_2-Ti ceramic-metal/metalloid composite bulks with high density and promising mechanical properties through selective laser melting technique (Liu, 2020a; Liu, 2020b).

1.4.2 Powder requirements for SLM

These are basic criteria for powder feedstock in the SLM process to form a thin and even powder layer, to ensure good processability and high-quality of the products.

- ***High and uniform sphericity***
  Highly spherical particles possess smoother surfaces which alleviate inter-particle motion to provide better rheology performance. Quality feedstock requires spherical particles with few irregularities (Attar, 2015; Bourell, 2011).
- ***Sufficient flowability***
  Homogeneous spherical powders with Gaussian size distribution provide smooth coating of the build area in the granular feedstock. Particle shape irregularity, increase in surface area due to the reduction of particle size, rough oxide skin, as well as high humidity result in powder flow deterioration.

- ***High packing density***
  The powder granules with a wide size distribution and optimal amounts of fine grains (multi-modal or negatively skewed Gaussian distribution) contribute to display high packing densities. Non-uniform powder packing properties will lead to disordered irradiation of powder particles by the laser beam causing an inhomogeneous material coalescence and defective parts (Tan, 2017).
- ***Avoiding powder surface contamination***
  Despite the fact, that the SLM process is carried out in a highly controlled inert environment, residual oxygen in the flooded gas and oxygen pick-ups are still inevitable, especially for the powders showing high affinity to oxygen. The surface oxidation of the powders disturbs the stability of the melt pool, splitting it into smaller drops, which is recognized as balling effect (Tan, 2017).
- ***Sufficient thermal absorptivity and thermal conductivity***
  A powder's laser absorptivity alters with the sum of particles irradiated by the laser and is greatly affected by powder's thermal conductivity and tapped density. High packing density of the powders would allow more irradiated energy transmission reaching the underlying substrate (Tan, 2017; Sun, 2017b).

1.5 Objectives of the study

For industrial applications engaging to manufacture novel customised products, the SLM/SLS processing of composites with specific and tailored properties has become a viable commercial business. Taking into consideration the rapid development of SLM/SLS, the fabrication of composites remains the challenging issue as the use of the products depends upon the quality of the produced items. By tailoring the material properties, more efficient engineering structures can be offered to the market.

Therefore, the overall objective of the current PhD study is development and manufacturing of novel $MoSi_2$-containing powder feedstock suitable for SLM/SLS processing and printing reliable items using the developed powders.

The main aims are as the following:

1. Development and preparation of SLM applicable $MoSi_2$-Si composite powders, by self-propagating high-temperature synthesis technique.
2. Manufacturing and characterization of SLM prepared $MoSi_2$-Si based bulks and lattices.
3. Manufacturing and characterization of $MoSi_2$- Si_3N_4 ceramic lattices.
4. Consolidation of $Mo(Si,Al)_2$ based composites from Mo-Si-AlSi10Mg and $MoSi_2$-AlSi10Mg powder mixtures by SLM.
5. Process optimization for selective laser melting of Mo-2Si-30 wt.% AlSi10Mg and $MoSi_2$-30 wt.% AlSi10Mg powders.
6. Evaluation of the effect of process parameters on mechanical properties, microstructure, phase composition and surface finish of the printed $Mo(Si,Al)_2$ based composite bulks.

2 Materials and methods

2.1 Design of the systems and powder feedstock preparation

The preparation pathways of $MoSi_2$-Si_3N_4 and $Mo(Si,Al)_2$-based composites (by two different routines) are depicted in Fig. 6. The raw materials used for powder feedstock preparation are listed in Table 2.

Considering the challenges of direct selective laser melting of $MoSi_2$-Si_3N_4 powder mixture, a novel approach was proposed for $MoSi_2$-Si_3N_4 part fabrication, including SLM applicable $MoSi_2$-Si powder preparation by self-propagating high-temperature synthesis, selective laser melting of $MoSi_2$-Si powder feedstock and further nitridation. This work has focused on the preparation of $MoSi_2$-15.6 wt.% Si_3N_4 and $MoSi_2$-20 wt.% Si_3N_4 parts, from powders prepared by SHS technique (Fig. 6a).

For the feedstock preparation aiming at fabrication of $Mo(Si,Al)_2$-based composites by routine 1 (Fig. 6b), elemental Mo, Si and AlSi10Mg powders with 44.2:25.8:30 wt.% ratio (Mo+2Si+30 wt.% AlSi10Mg) were dry mixed for 3 h at 20 rpm mechanical rotation speed. The feedstock for the fabrication of $Mo(Si,Al)_2$-based composites by routine 2 (Fig. 6c) was prepared by mixing combustion synthesized $MoSi_2$ powder with AlSi10Mg alloy with 70:30 wt.% ratio, respectively following the mixing procedure as for routine 1. Prepared powders were characterized with different analyses techniques.

Table 2. Raw materials (powders)

Name	Composition	Particle size	Purity	Producer
Molybdenum	Mo	1-5 µm	99.9%	Aldrich
Molybdenum	Mo	<5 µm	99%	Pacific Particulate Materials
Silicon	Si	<20 µm	99%	Silgrain-Elkem
Aluminum alloy	AlSi10Mg	15-63 µm	99%	SLM Solutions

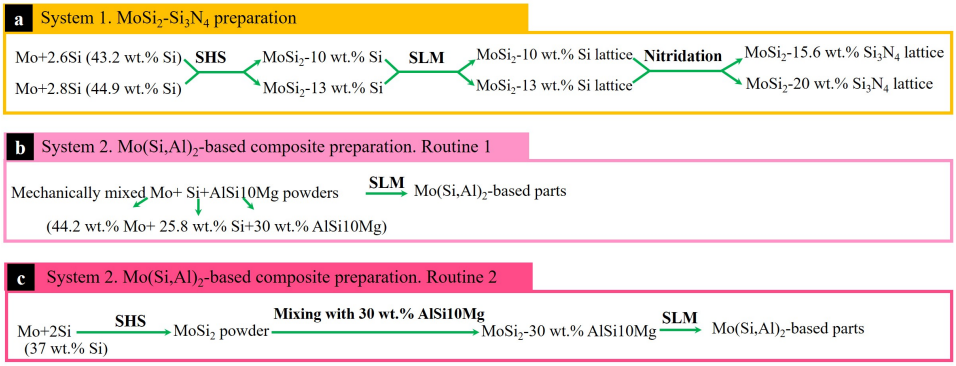

Figure 6.The preparation pathways for $MoSi_2$-Si_3N_4 (a) and $Mo(Si,Al)_2$-based composites by routine 1 (b) and routine 2 (c).

For $MoSi_2$, $MoSi_2$-10 wt.% Si and $MoSi_2$-13 wt.% Si powders, the combustion synthesis of 3 various compositions of powder mixtures with elemental Mo:Si molar ratio of 1:2, 1:2.6 and 1:2.8 was conducted (Fig. 6a and c). The homogenized powders mixtures were poured into a reaction boat and placed into the CPR-3.5 liters reaction chamber. Afterwards the chamber was purged and flooded with nitrogen (purity 99.97%, oxygen content not exceeding 0.02%) to the pressure of 0.2 MPa. The combustion process was

launched by short heating of ignition coil (18 V, 3 s) from the side corner of the specimen (Fig. 7). $MoSi_2$, $MoSi_2$-10 wt.% Si and $MoSi_2$-13 wt.% Si products (Table 3) were crushed into powders and sieved with a 45 µm openings.

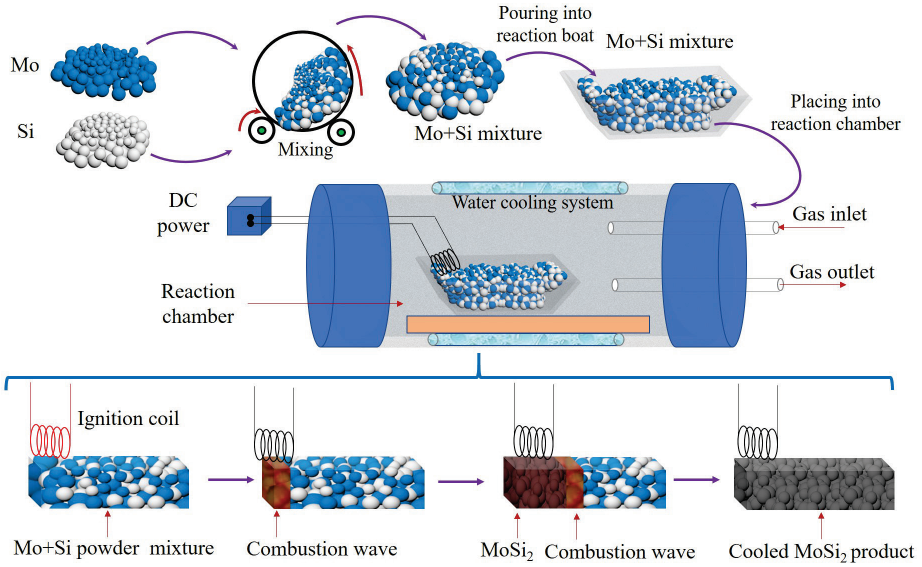

Figure 7. Schematic representation of $MoSi_2$ preparation by self-propagating high-temperature synthesis technique.

Table 3.The composition of elemental powders mixture of reactants and the SHS products

Raw materials		SHS Product			
Mo	Si	$MoSi_2$	Si	$MoSi_2$	Si
(moles)	(moles)	(moles)	(moles)	(wt.%)	(wt.%)
1	2	1	0	100	0
1	2.6	1	0.6	90	10
1	2.8	1	0.8	87	13

2.2 Powders characterization

The particle size analysis of the powders was carried out by CAMSIZER X2 (Retsch Technology, Haan, Germany) instrument using the digital image processing principle.

The FT4 Powder Rheometer (Freeman Technology, Tewkesbury, UK) was utilized to determine the flowing behavior of the powders by means of basic flowability energy (BFE). To determine the resistance of powder to flow 8 tests were performed. For each of the tests the precision blade is rotating downwards (100 $mm \cdot s^{-1}$ speed) and upwards through the powder creating a particle flow. BFE is calculated from the BFE = E_{test8} equation, where E_{test8} is the energy registered during 8^{th} test. Stability Index (SI) is calculated according to SI= E_{test8}/E_{test1} formula.

Powder cohesion and the flowing angle were measured by GranuDrum (GranuTools, Awans, Belgium). The powder was half-filled into the cylindrical drum and placed in the device. The drum rotated around its axis with 2-10 rpm speed producing particle flow.

Installed cameras were collecting images after each rotation, revealing the air/powder interface position by edge detection.

The powders' packing density was estimated by GranuPack (GranuTools, Awans, Belgium). Powder was filled in the vessel and device taped the powder for 2000 times. The actual values for average bulk density at the end of each trial (ρ[n]) are defined, and the bulk density values were extrapolated (ρ[∞]).

Differential scanning calorimetry (DSC) analysis were conducted to investigate the thermal behavior of feedstock powders by NETZSCH-STA 449 F1 Jupiter (NETZSCH-Gerätebau GmbH, Selb, Germany) thermal analyzer at 25 °C to 1450 °C operating temperature and with 20 °C·min^{-1} heating rate in argon environment.

2.3 SLM for powder consolidation

The consolidation of $MoSi_2$/10-13 wt.% Si (System 1) and Mo+2Si+30 wt.% AlSi10Mg powder mixture (System 2 routine 1) was performed in Metal 3D Printer SLM-50 (Realizer GmbH, Germany) employing Yb:YAG fiber laser (120 W max power and 1.07 µm wavelength). A "zig-zag" scan strategy was applied and the laser scan pattern rotation angle for each layer was set 90°.

The consolidation of $MoSi_2$-30 wt.% AlSi10Mg powder mixture (System 2, routine 2) was conducted in Renishaw AM400 (Renishaw, UK), which employs an Ytterbium laser with continuous-wave (CW) emission strategy of power (maximum power of 400 W, 1.07 µm wavelength), while adjusted to operate like a pulse wave (PW) laser system. The Meander scan pattern was used as scan strategy, and the angle of scanning was alternated by 67° with respect to the precedent layer. Prior to laser treatment, the chamber was filled with inert gas (N_2 or Ar); at oxygen level below 500 ppm. Figs. 8-10 demonstrate the process parameters applied for the consolidation of $MoSi_2$/10-13 wt.% Si, Mo+2Si+30 wt.% AlSi10Mg and $MoSi_2$-30 wt.% AlSi10Mg powders mixtures via selective laser melting.

System 1

To determine the printability of the $MoSi_2$-Si composite powders, bulk cylindrical samples with ∅10 mm x 5 mm dimensions were prepared by SLM technique. Afterwards, for $MoSi_2$-Si_3N_4 composite preparation, $MoSi_2$-Si cellular lattice structures (designed by Magics software) with ∅10 mm x 5 mm height and with definite porosity level (66%) were produced and subjected to nitridation in the furnace (WEBB, Greensboro, USA) at 1350 °C with 10 °C min^{-1} heating rate, in nitrogen flow of 200 sccm (standard cubic centimeters per minute).

In System 1, lattices and bulks of $MoSi_2$-10 wt.% Si are labeled as L1-L6 and B1-B2, and lattices and bulks of $MoSi_2$-13 wt.% Si are labeled with L1*-L6* and B1*-B2*, respectively (Fig. 8). For bulk samples laser power of 26.4 W and 31.2 W and for lattices 36 W, 40.8 W, 48 W, 60 W, 72 W and 84 W (corresponding to 1500-3500 W laser current), was used at fixed 80 mm·s^{-1} scanning speed (ν). The hatching distance (h) was set as 60 µm and layer thickness (d) as 25 µm.

Laser volumetric energy density (LVED) was estimated according to E=P/νhd formula, where P is the laser power, ν-scanning speed, h-hatching space and d speaks for the layer thickness. Process parameters and samples' labels are represented in Fig. 8.

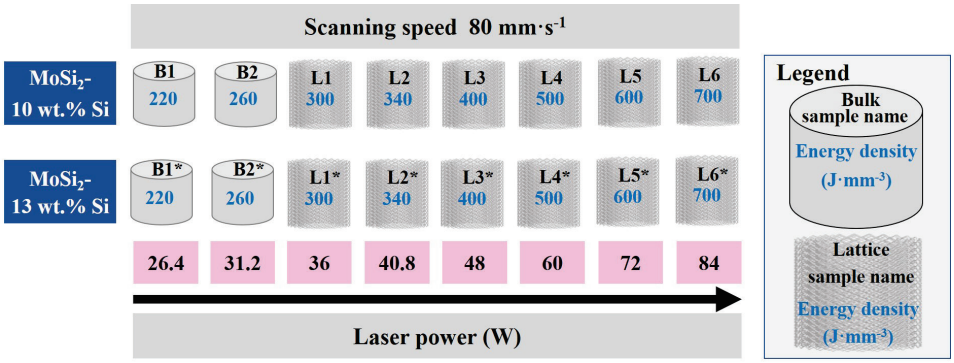

Figure 8. SLM process parameters for consolidation of $MoSi_2$-10 wt.% Si (first row) and $MoSi_2$-13 wt.% Si (second row) composite powders for bulk and lattice sample preparation (Note, process was carried out in Realizer SLM-50 device).

System 2. Routine 1

$Mo(Si,Al)_2$ based composite bulks with ∅ 10 mm x 5 mm dimensions prepared by SLM of Mo+2Si+30 wt.% AlSi10Mg powder mixture are labeled as A1-A4. Specimens were prepared at 100 W laser power, at fixed point distance (85 µm), hatching distance (85 µm) and layer thickness (35 µm). The scanning speed was altered to 300, 350, 400 and 500 $mm \cdot s^{-1}$. The energy density was in 67.2-112.0 $J \cdot mm^{-3}$ range. Build rate was derived from BR=νhd formula, where ν is scanning speed, h-hatching distance and d-layer thickness.

Sample's labels and respective process parameters are illustrated in Fig. 9.

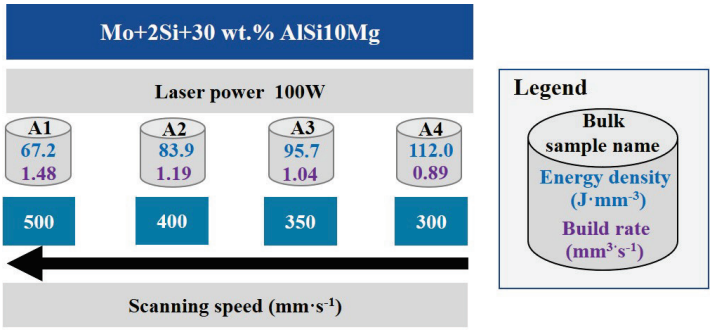

Figure 9. SLM process parameters for consolidation of Mo+2Si+30 wt.% AlSi10Mg powder mixture (Note, process was carried out in Realizer SLM-50 device).

System 2. Routine 2

$Mo(Si,Al)_2$ based composite bulk samples with 7 mm of height and diameter ∅ were prepared. The hatching distance and laser spot size were correspondingly set as 85 µm and 90 µm. Laser power was changed from 100 to 300 W with the step size of 50 W. Point distance was chosen 85 µm and exposure time accordingly to achieve 400-1500 $mm \cdot s^{-1}$ scan speed. The layer thickness was set 35 µm, as the D50 of $MoSi_2$-30 wt.% AlSi10Mg powder particles was less than 35 µm. The labels for each sample and corresponding scheme of process parameters are depicted in Fig. 10.

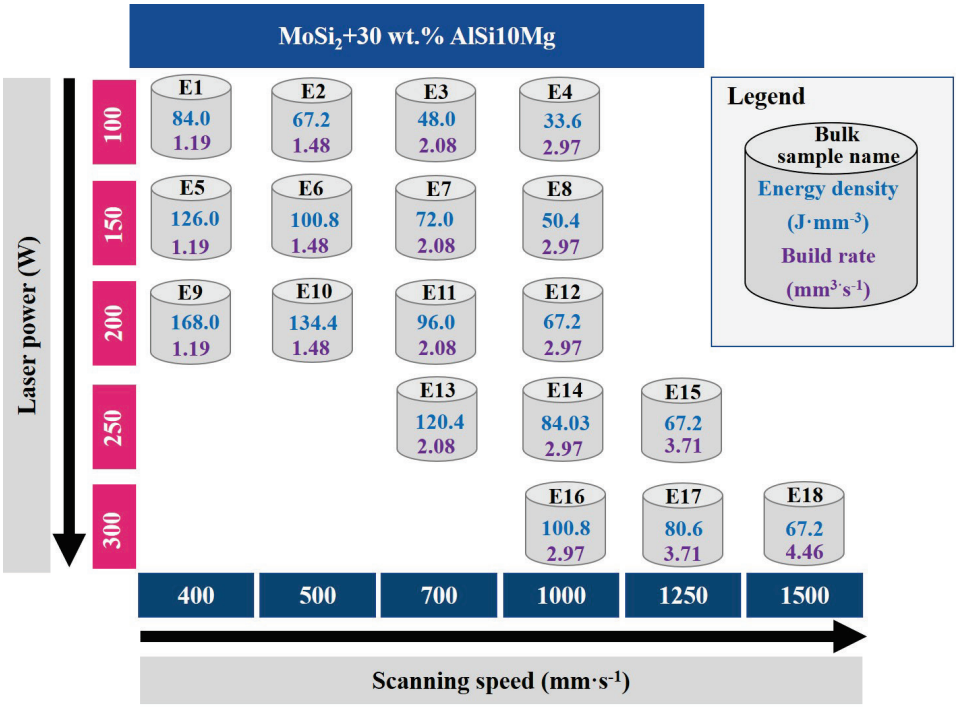

Figure 10. SLM process parameters for consolidation of $MoSi_2$-30 wt.% AlSi10Mg powder mixture (Note, process was carried out in Renishaw AM400 device) ***(adapted from Paper V)****.*

2.4 Characterization of printed parts

Density values of the as-printed parts were measured by Archimedes' principle (Mettler Toledo ME204, Australia) and by measuring volume (Digital Caliper, 0.01 mm accuracy, KS Tools Werkzeuge-Maschinen GmbH, Germany) and weight (Eltra 84 analytical balance, 0.1 mg accuracy, Haan, Germany) of the samples. For porosity evaluation in the SLM-fabricated samples, the X-ray computed tomography (CT) was performed by 3D X-ray microscope (ZEISS Xradia 520 Versa, Carl Zeiss Microscopy GmbH, Jena, Germany). The surface roughness analysis was performed by Keyence VK-X250 3D laser scanning microscope (Keyence Corporation, Osaka, Japan) using 20x lens. The average values of maximum height (Sz) and arithmetical mean height (Sa) were defined.

Zeiss EVO MA15, HR-SEM Zeiss Merlin and TESCAN VEGA3 scanning electron microscopes (SEM) equipped with INCA Energy, Bruker EDX-XFlash6/30 and Bruker QUANTAX 200 (USA) EDS detectors, respectively, were used to study the morphology and chemical composition of the powders, as well as the microstructural development in as-built and polished parts.

Phase identification of the samples was conducted with X-ray diffractometers (Siemens/Bruker, D5005 (USA) and Rigaku SmartLab SE (Japan)) with CuKα1 radiation (λ= 1.5406 Å). The phase and elemental composition of the samples were evaluated via Rietveld refinement method. The Indentec 5030 SKV tester (Brierley Hill, UK) was used for hardness measurements. Compression tests were performed by Instron 5869 test machine (Norwood, USA) with maximum force of 550 N. And the strain rate of 0.1 min^{-1} was chosen following ISO 13314:2011 standard (ISO 13314:2011).

3 Results and discussion

3.1 System 1. $MoSi_2$-Si_3N_4 preparation

Powders

The combustion synthesized $MoSi_2$-10 wt.% Si and $MoSi_2$-13 wt.% Si porous bulk products, represent agglomerates of 2-3 µm particulates (Fig. 11 a-d). The powdered $MoSi_2$/10-13 wt.% Si embody up to 20 µm agglomerates (Fig. 11 e-h). According to EDS mapping (Fig. 11i), during SHS process the $MoSi_2$ particulates are bonded by silicon melt.

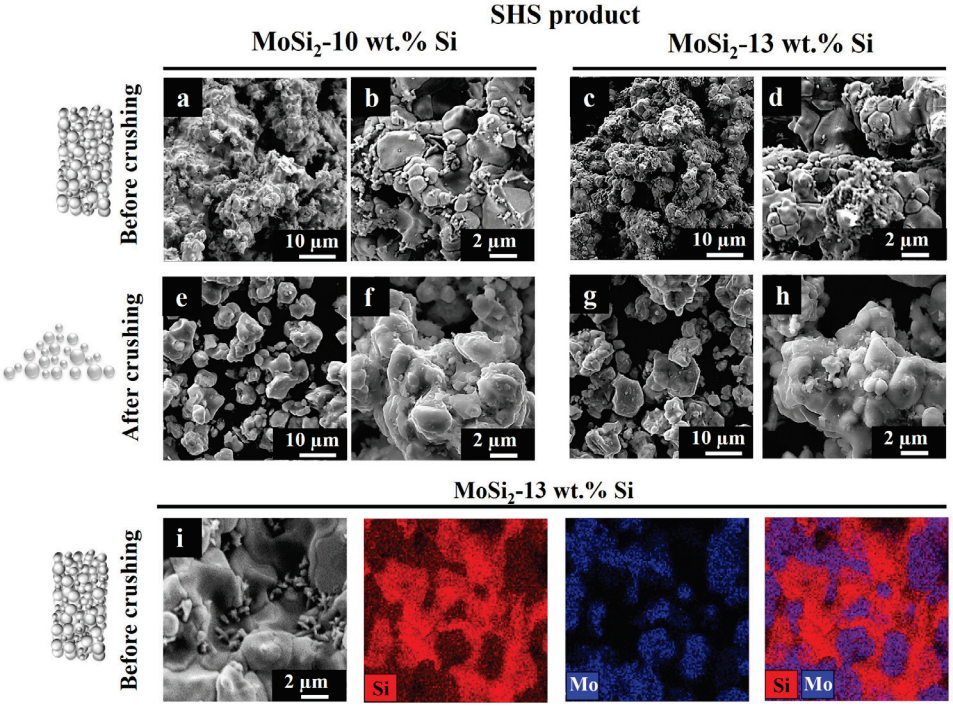

Figure 11. SEM images of combustion synthesized $MoSi_2$-10 wt.% Si (a, b) and $MoSi_2$-13 wt.% Si product (c, d), crushed powders of $MoSi_2$-10 wt.% Si (e, f) and $MoSi_2$-13 wt.% Si (g, i). EDS mapping of $MoSi_2$-13 wt.% Si (i) combustion product ***(adapted from Paper I).***

The diffractograms of combustion synthesized $MoSi_2$-10 wt.% Si (Fig. 12a) and $MoSi_2$-13 wt.% Si (Fig. 12b) composite powders show the distinctive peaks of tetragonal $MoSi_2$ and face centered cubic Si. No other phases are detected. The EDS maps of the respective secondary electron image (Fig. 12c) of the $MoSi_2$-13 wt.% Si composite powder (Fig. 12, d-f) show the $MoSi_2$ particles are smoothly covered and bonded with a layer of molten silicon (Fig. 12d, green map), making the impression of "core-shell" structure.

Fig. 13 shows the $MoSi_2$-13 wt.% Si composite powder/air interfaces captured during drum rotation, pointing that the angle of repose is ~47-48° at 2-10 rpm drum rotation speed. This states the applicability of the chosen powder for SLM. Similar results were obtained for $MoSi_2$-10 wt.% Si composite powder. The initial bulk density of $MoSi_2$-13 wt.% Si was 1.91±0.010 $g \cdot ml^{-1}$, after 2000 taps 2.75±0.042 $g \cdot ml^{-1}$ and the extrapolated value was calculated to be 2.93±0.034 $g \cdot ml^{-1}$. For $MoSi_2$-10 wt.% Si powder almost similar results were achieved.

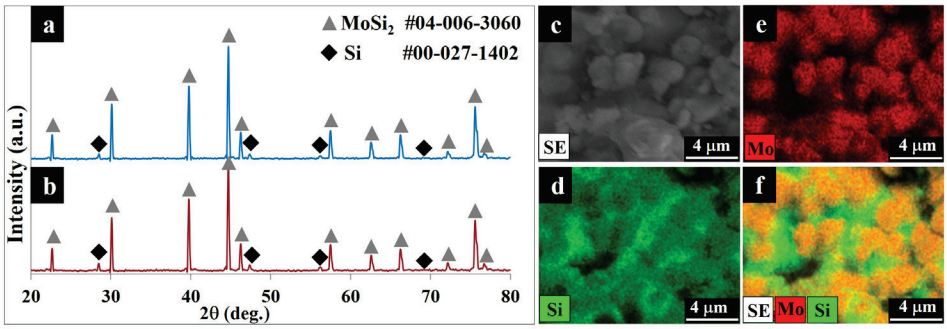

Figure 12. XRD patterns of powdered $MoSi_2$-10 wt.% Si (a), $MoSi_2$-13 wt.% Si (b) and EDS mapping of $MoSi_2$-13 wt.% Si (c-f) ***(adapted from Paper II).***

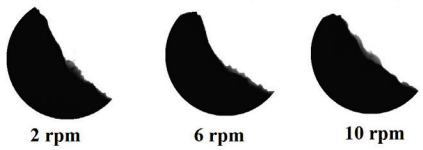

Figure 13.Captured images of the $MoSi_2$-13 wt.% Si powder repose at drum rotation speed of 2, 6 and 10 rpm.

Bulks

The top view micrographs of $MoSi_2$-10 wt.% Si and $MoSi_2$-13 wt.% Si composites consolidated at 26.4W and 31.2W laser power are shown in Fig. 14.

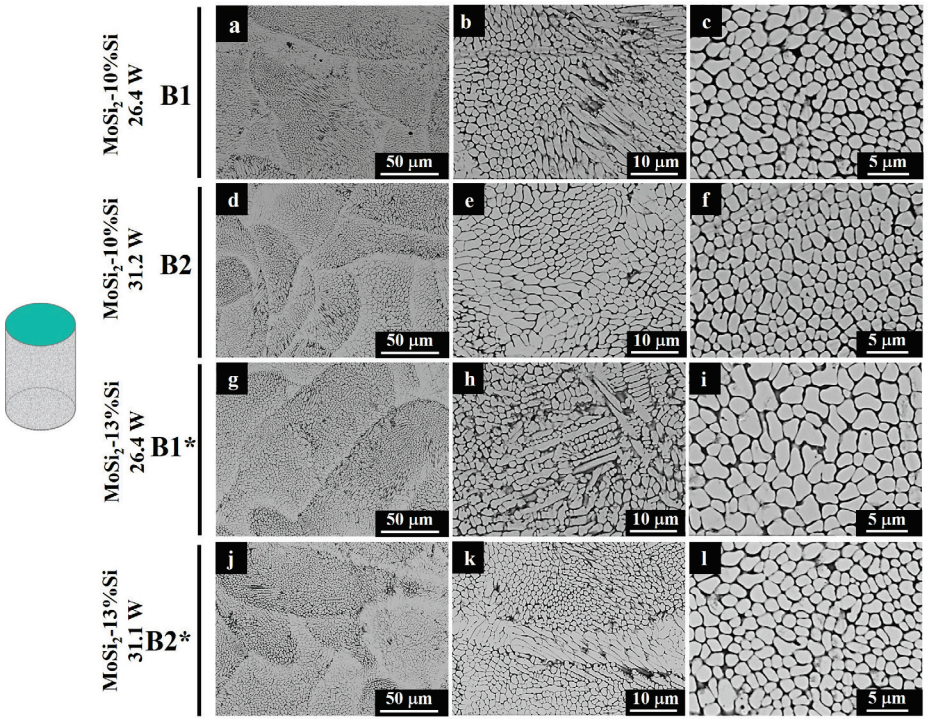

Figure 14. Backscattered electron images of polished top surfaces of samples B1(a-c), B2(d-f), B1 (g-i) and B2* (j-l) with various magnifications.*

The long scanning tracks composed of half-cylindrical shaped horizontal cross sections of the melt pools from different scanned layers are visible. The melt pool solidification mode is observed to be mostly cellular, but periodically, several side-branching was observed. The samples mainly consist of 1-3 µm size $MoSi_2$ cellular grains (Fig. 14 c, f, i, l) enveloped and bonded by submicron layer of molten silicon shell, as shown by the EDS maps of the fabricated sample B1* (Fig. 15).

The change in cell size and frequent edge segregation of silicon implements to differentiation of the melt pool tracks from low magnification images (Fig. 14 a, d, g, j). In Fig. 14 b and k the presence of infrequent elongated $MoSi_2$ grains and in Fig. 14h misoriented columnar dendritic $MoSi_2$ crystals with occasional secondary arming were observed.

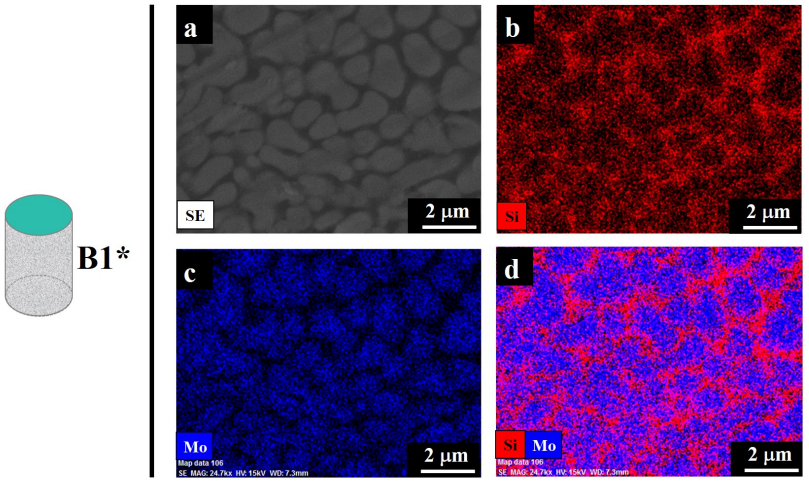

Figure 15. Top surface secondary electron (SE) image and respective EDS maps of sample B1 (red and blue areas demonstrate the distribution of Si and Mo respectively)* ***(adapted from Paper I)****.*

The highest relative density was achieved for sample B2 being 90%, and due to the fine decoration of silicon around $MoSi_2$, the Vickers hardness of the as-built B2, B1* and B2* samples at 1 kg load was in 10.3-10.9 GPa range for B2, B1* and B2* samples (Table 4).

Table 4. Density and hardness results of B1, B2, B1 and B2* bulk samples* ***(Paper I)***

Bulk sample (Name)	Laser power (W)	Laser current (mA)	Relative Density (%)	Hardness (GPa)
B1	26.4	1100	82	8.8
B2	31.2	1300	90	10.3
B1*	26.4	1100	83	10.8
B2*	31.2	1300	88	10.9

According to compression test results the ultimate compressive strength (σ_u) and compressive strain for bulk sample B2 was 610 MPa and 19.3%, respectively.

Based on above mentioned statements it was proven the printability of $MoSi_2$/10-13 wt.% Si composite powder by SLM approach.

Lattices

Making headway with the next step $MoSi_2$-10 wt.% Si and $MoSi_2$-13 wt.% Si lattices were produced and subjected to subsequent nitridation for $MoSi_2$-Si_3N_4 composite lattice preparation. Six lattices were prepared from each composite powder.

Fig. 16 d-i shows the top view SEM images of L1*- L6* $MoSi_2$-13 wt.% Si lattices produced at 36-84 W laser power. The estimated strut diameter of the lattices varied in 300-350 µm, the pore diameter in 750-850 µm and the period size in 1100-1200 µm range. For $MoSi_2$-10 wt.% Si L1-L6 lattices the strut diameter values were measured in 380-490 µm, pore diameter from 625 to 725 µm and the period size in 1050-1170 µm interval **(Paper II).** In this case the strut diameters overmatch the designed model (Fig. 16 a and b), due to number of adhered particles from heat affected zones on the struts, which artificially increase the struts diameter.

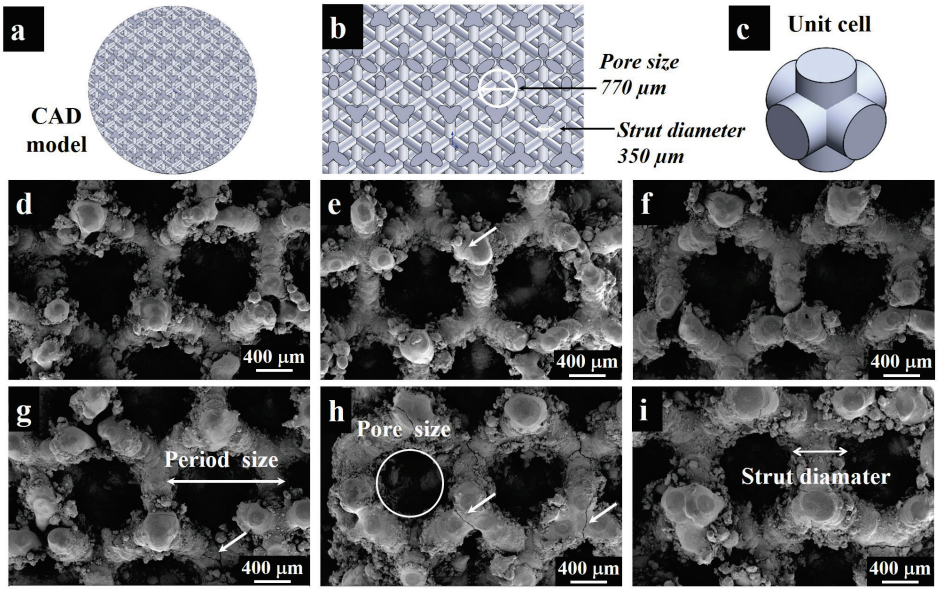

Figure 16. The CAD model of the lattice (a, b) and unit cell (c). SEM images of $MoSi_2$-13 wt.% Si lattices produced at 36W (d), 40.8 W (e), 48 W (f), 60 W (g), 72 W (h) and 84 W (i) laser power ***(adapted from Paper II).***

Apparently, the applied laser power has a remarkable effect on the strut diameter of produced cellular structures. In consolidation process, the laser beam initially melts silicon (which has lower melting point) and the subsequent sintering occurs in liquid-solid state. The molten Si serves as a binding phase providing capillary force for bonding the ceramic particles and for subsequent 3D structure development. High ceramic portion in the composite leads to low solidification shrinkage when relatively low laser power is used. Increasing the laser power from 36 to 60 W, the apparent relative density for $MoSi_2$-10 wt.% Si lattices was increased from 33% to 39% and for $MoSi_2$-13 wt.% Si lattices from 32 to 35%. While applying laser power of 72 and 84 W resulted in the textile growth and expansion of struts increasing the apparent relative density of the $MoSi_2$-13 wt.% Si up to 47% **(Paper II)**. Conclusively, the lattices printed at lower 36-60 W laser power are in close correspondence with designed model (Fig. 16 a and b, 350 µm strut size, 770 µm pore size, 66% porosity, (34% apparent relative density)). The presence of

cracks, marked with white arrows, can be noticed from SEM images (Fig. 16 e, g and i) attributed to process induced thermal stresses and different coefficient of thermal expansion (CTE) of Si and $MoSi_2$, as CTE_{Si} = 2.59–4.56·10^{-6} K^{-1} and CTE_{MoSi2} = 8.6·10^{-6} K^{-1} **(Paper II)**. According to compression test results the ultimate compressive strength (σ_u) and compressive strain for L1 and L6 lattices were 8.7 MPa and 9.3 MPa, and 4.17% and 7.48% respectively (Table 5).

*Table 5. Mechanical properties of as-built (after SLM) and nitridized lattices **(Paper II)***

Lattice sample	**Ultimate compressive strength (σ_u)**	**Compressive strain**
(Name)	**(MPa)**	**(%)**
L1	8.7	4.17
L6	9.3	7.48
L1 nitridized	5.7	6.68

Fig. 17 a-c show the top fracture of lattice L1*, where tetragonal $MoSi_2$ (gray) is encircled with face centered cubic Si phase (white). The side fracture images (Fig. 17 d-f) show that the vertical cross section of the lattices consists of well oriented long columnar structures with casual arming grown perpendicular to build direction.

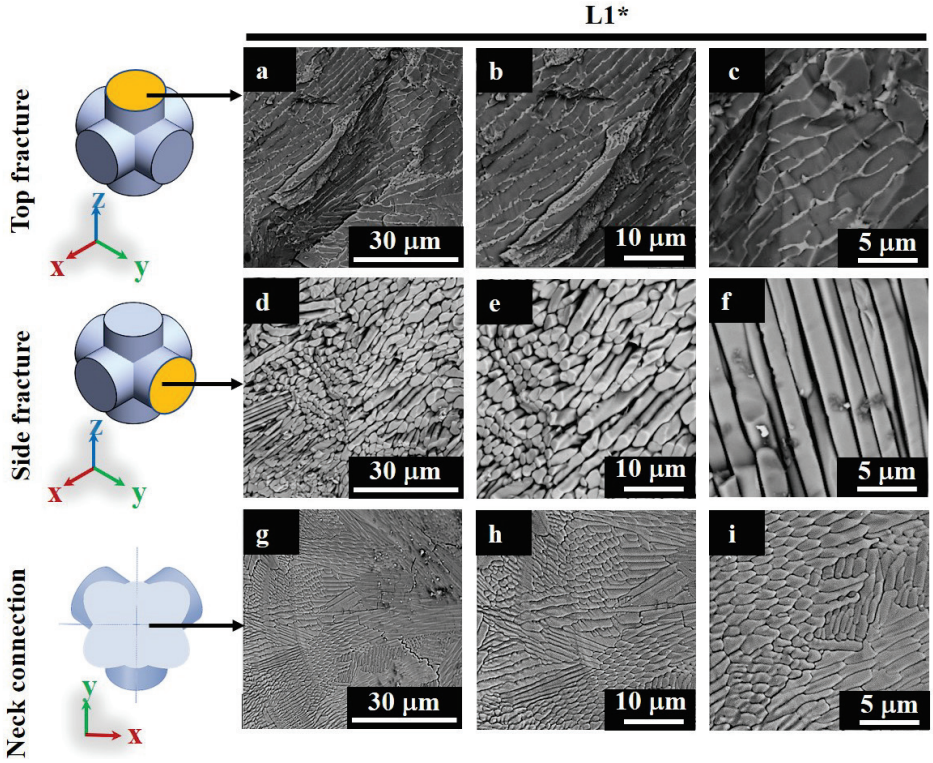

Figure 17. SEM images of top fracture (a-c), side fracture (d-f) and strut connection point (g-i) of $MoSi_2$-13 wt.% Si lattice sample L1.*

The neck connections of the lattices (xy plane) show the coexistence of columnar and cellular solidifications modes of melt pools (Fig. 17 g-i). The connecting area of 3 struts is composed of well oriented cells with length ranging from submicron to 2 µm (grown

along the temperature gradient direction) and misoriented 3-20 µm columnar grains nucleated and grown from cellular grains with converging grain boundaries. The latter is caused by the overlapping of the diffusion boundary layers of cellular grains, where the interaction leads to the columnar grains outgrowing the cells, Fig. 17i.

Eventually, to attain $MoSi_2$-Si_3N_4 lattices the $MoSi_2$/10-13 wt.% Si lattices were attempted to nitridize in nitrogen atmosphere to convert Si into Si_3N_4. The XRD pattern of nitridized L4 and L4* lattices (Fig. 18 a and b) reveal the characteristic peaks of $MoSi_2$, Si_3N_4, while Mo_5Si_3 peaks were also detected disturbing the compositional balance of the samples. Thus, samples with $MoSi_2$-5.1 wt.% Mo_5Si_3-14.8 wt.% Si_3N_4 and $MoSi_2$-9.4 wt.% Mo_5Si_3-17.5 wt.% Si_3N_4 composition were prepared (Table 6).

Table 6. Expected and achieved compositions of samples L4 and L4 before and after nitridation*

Sample	**Expected composition (wt.%)**			**Achieved composition (wt.%)**			
Name	**$MoSi_2$**	**Si**	**Si_3N_4**	**$MoSi_2$**	**Si**	**Mo_5Si_3**	**Si_3N_4**
L4	90	10	0	90	10	0	0
L4*	87	13	0	87	13	0	0
L4-nitridized	84.4	0	15.6	80.1	0	5.1	14.8
L4*-nitridized	80	0	20	73.1	0	9.4	17.5

After heating the $MoSi_2$/10-13 wt.% Si samples in nitrogen, the struts of the lattices were expanded by 5-10 µm while maintaining the period size in the same scope. Nanosize Si_3N_4 fibers (Fig. 18 c and f) were grown on lattice struts, which may additionally reinforce the fabricated material.

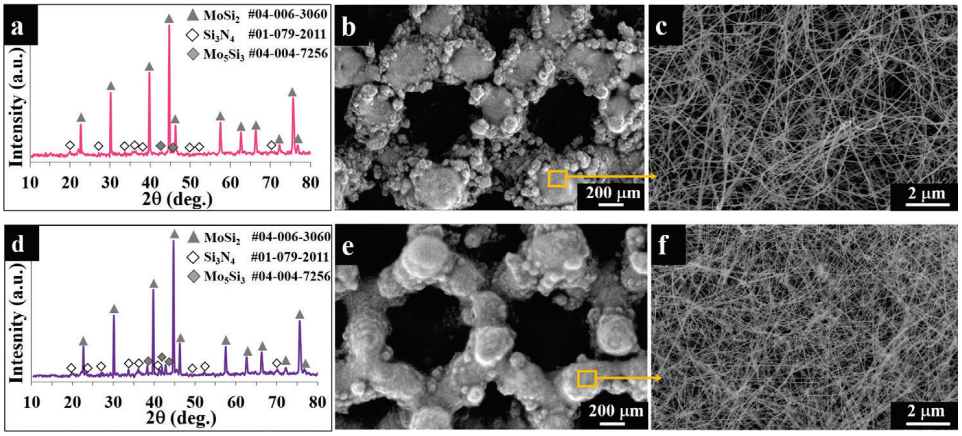

Figure 18. XRD pattern (a), SEM images (b, c) of nitridized $MoSi_2$-10 wt.% Si lattice sample L4. XRD pattern (d), SEM images (e, f) of nitridized $MoSi_2$-13 wt.% Si lattice sample L4 **(adapted from Paper II).***

Analyzing the compression test results, it can be noted, that the compressive strain of the nitridized $MoSi_2$-10 wt.% Si L1 lattice (6.68%) was higher in comparison with the compressive strain of as-built sample (4.17%), Table 5 **(Paper II).**

Considering that the dimensions of the lattices were in a close correspondence with CAD model, the laser power in 36-60 W range was chosen as optimum, and heating the lattices at 1350°C for 3h in N_2 was sufficient for almost complete $Si \rightarrow Si_3N_4$ conversion.

3.2 System 2. $Mo(Si,Al)_2$-based composite preparation. Routine 1.

Powders

Feedstock for SLM (Fig. 19d) consists of agglomerates of Mo in the form of 2-3 µm spherical particulates (Fig. 19a), angular shaped Si powder (Fig. 19b) and gas atomized AlSi10Mg in the form of spherical particles and satellite structures (Fig. 19c). The angle of repose and cohesion of Mo+2Si+30 wt.% AlSi10Mg powder mixture were measured to be 49° and 14.7, respectively, exhibiting the fair flowability of the powder for SLM processing. The XRD pattern shows the respective peaks of body-centered cubic Mo and face-centered cubic Al and Si (Fig. 19e).

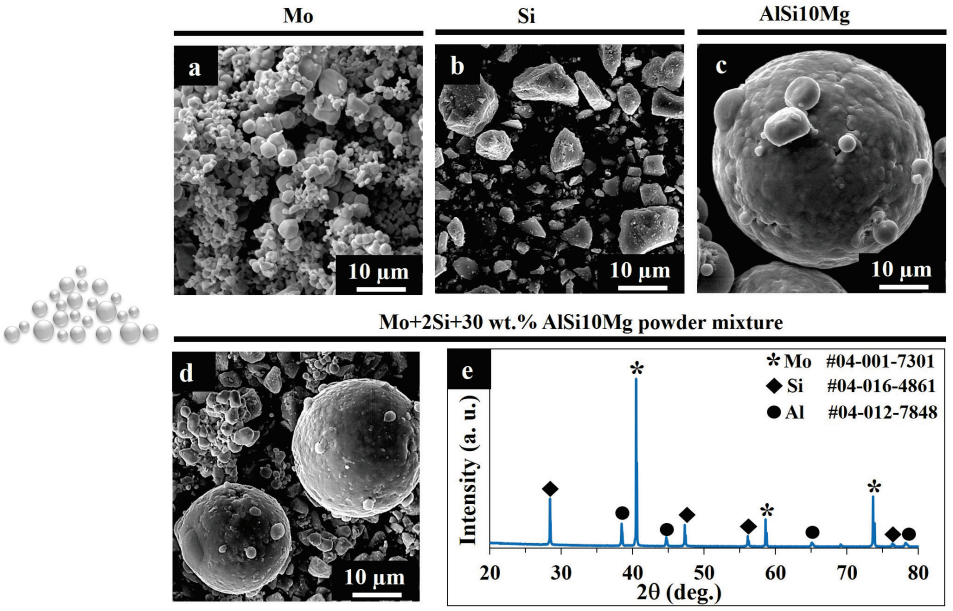

Figure 19. SEM images of Mo (a), Si (b), AlSi10Mg (c) raw powders. SEM image (d) and XRD pattern (e) of Mo+2Si+30wt.%AlSi10Mg powder mixture ***(adapted from Paper III).***

Bulks

Fig. 20 represents SEM images of sample A2 fabricated at 83.9 $J \cdot mm^{-3}$ energy density. The top view micrographs point the elliptically shaped melt pools (marked with orange dashes) from different printed layers. In the center of the melt pool fine columnar dendrites with occasional arming were homogenously distributed perpendicular to the stacking direction and grown towards thermally favorable directions. Coarsening of dendrites towards to the border of the melt pools took place (Fig. 20b) and segregation of Al-Si phase was observed (Fig. 20a marked with pink arrows and Fig. 21 f). Fine columnar dendrites in the core are enfolded by the comparably coarse and long columnar dendrites in the periphery (Fig. 20b), as a result of overlapping of neighboring melt pools. Figure 20 d-f illustrate the unpolished side surface of sample A2, demonstrating the presence of fine columnar dendrites in the center (Fig. 20e), and coarser grains in the boundary (Fig. 20f).

EDS mapping of sample A2 (Fig. 21a) indicates that the light gray dendritic textures are composed of Mo, Si and Al (Fig. 21e, purple phase), while the dark gray textures represent the Al rich phase (Fig. 21b, green map). Hexagonal C40 $Mo_3(Si_4Al_2)$, (which corresponds to $Mo(Si_{0.67}Al_{0.33})_2$ composition) together with face centered cubic $Al_{0.85}Si_{0.15}$

and free unreacted silicon were identified in sample A2 XRD profile (Fig. 21g). The hexagonal C40 molybdenum aluminosilicide was developed as the dominant phase, and $Al_{0.85}Si_{0.15}$ phase was generated from aluminum-silicon eutectic liquid.

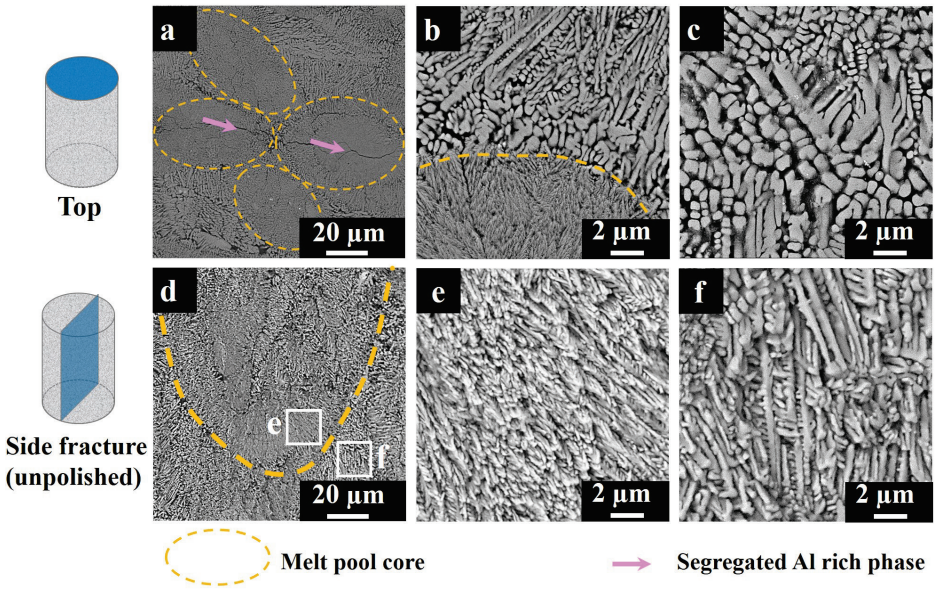

Figure 20. SEM images of the polished top surface (a-c) and unpolished side fracture (d-f) of sample A2 ***(adapted from Paper III)***

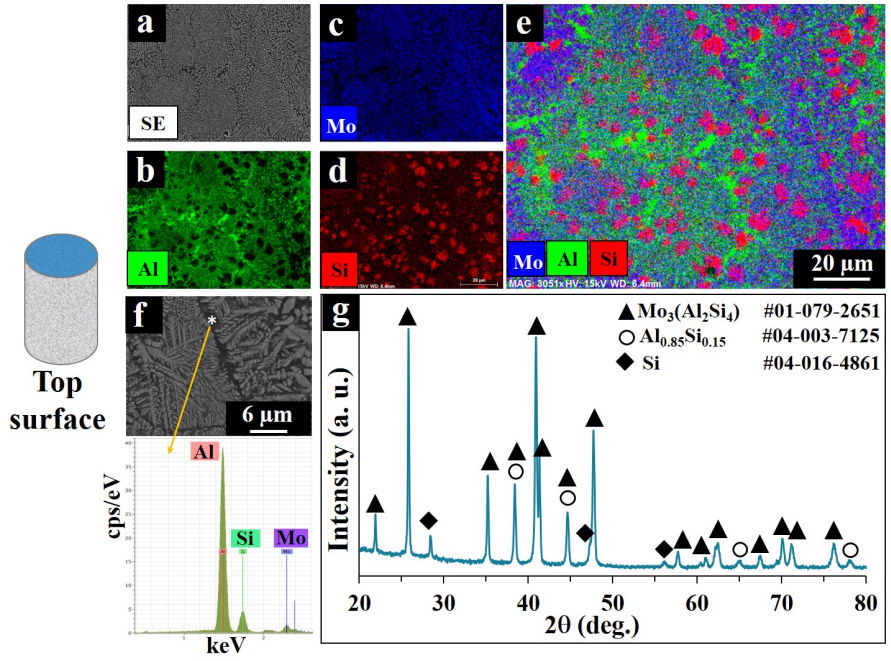

*Figure 21. Secondary electron image (a), EDS maps (b-e), backscattered electron image and EDS spectrum measured from the point marked as * (f). XRD pattern from top surface of sample A2 (g)* ***(adapted from Paper III)****.*

Phase content analysis has revealed that despite the change in applied energy density, all samples have similar phase composition, and quantitative analysis of element content indicated a close correspondence with starting reactant mixture **(Paper III).**

In defiance of the detection of aluminum rich $Al_{0.85}Si_{0.15}$ phase, the $Mo(Si_{1-x},Al_x)_2$ phase was formed with x=0.33 mole (while based on the literature review at excess aluminum content x should grow up to 0.65 mole forming $MoAl_{1.3}Si_{0.7}$ ($Mo(Si_{0.35}Al_{0.65})_2$) (Ghayoumabadi, 2009). This could be explained by localized heating nature and fast heating/cooling rates of SLM process, preventing the further widening of the C40 lattice and the development of the orthorhombic Al dominant C54 molybdenum aluminosilicide phase of a restricted homogeneity zone.

As the composition of molybdenum aluminosilicide is dependent on the composition of reactive mixture, Mo+1.34Si+0.66AlSi10Mg stoichiometric powder mixture was subjected to thermogravimetric analysis, to form pure $Mo(Si_{0.67}Al_{0.33})_2$. From the DSC curve the endothermic peak at 579°C speaks for the formation of the Al-Si eutectic phase formation (T_{start}=570°C). The high exothermic interaction between Mo and Al-Si phase initiates at 800°C registering the largest heat release at 869°C (Fig. 22a). No other thermal effects were identified up to the end of heating process demonstrating almost complete consumption of molybdenum.

XRD analysis of quenched DSC product (Fig. 22b) revealed the presence of 95.9% $Mo_3(Al_2Si_4)$ along with negligible amount of Mo (0.9%), $Al_{0.85}Si_{0.15}$ (1.9%) and Mo_5Si_3 (1.3%) phases, meaning that aluminum is substituting silicon up to x=0.33 mol (2x=0.66), as was observed for SLM fabricated samples.

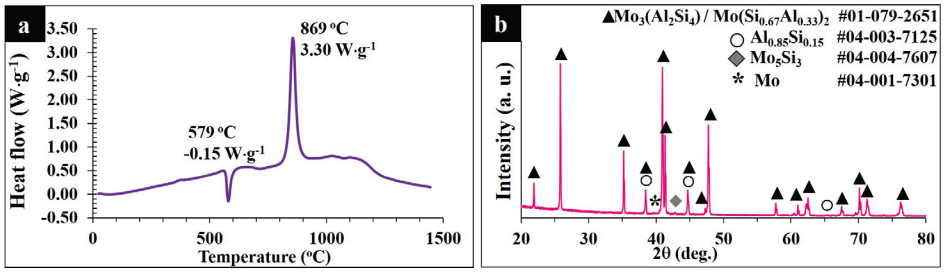

Figure 22. DSC curve of Mo+1.34Si+0.66AlSi10Mg powder mixture (a) and XRD pattern of quenched specimen after DSC analysis (b) ***(adapted from Paper III).***

Making strides to characterization of printed A1-A4 samples, Fig. 23 demonstrates the side surface profiles and the average surface roughness results by means of Sa and Sz. All printed samples possess moderate surface roughness (Sa) in 8.4-11.1 µm (Fig. 23e) and maximum height (Sz) in 89-111 µm range (Fig. 23f), with standard deviation less than 10%.

The quality of the $Mo(Si_{0.67}Al_{0.33})_2$-based specimens produced by routine 1 from the Mo-Si-AlSi10Mg powder, is not conceding the SLM produced AlSi10Mg parts according to the results of the side surface roughness (Sa) reported to be in 8-11 µm range (Majeed, 2019; Yu, 2019).

Fig. 23 g shows the 3D microscan of sample A2. The detected pores determine the porosity of 0.02%. Most of the disclosed pores are in 40-50 µm range (colored with pink, purple and blue) (Fig. 23i) with aspect ratio of 0.3 and 0.4 (Fig. 23j), meaning that they primarily possess irregular shape.

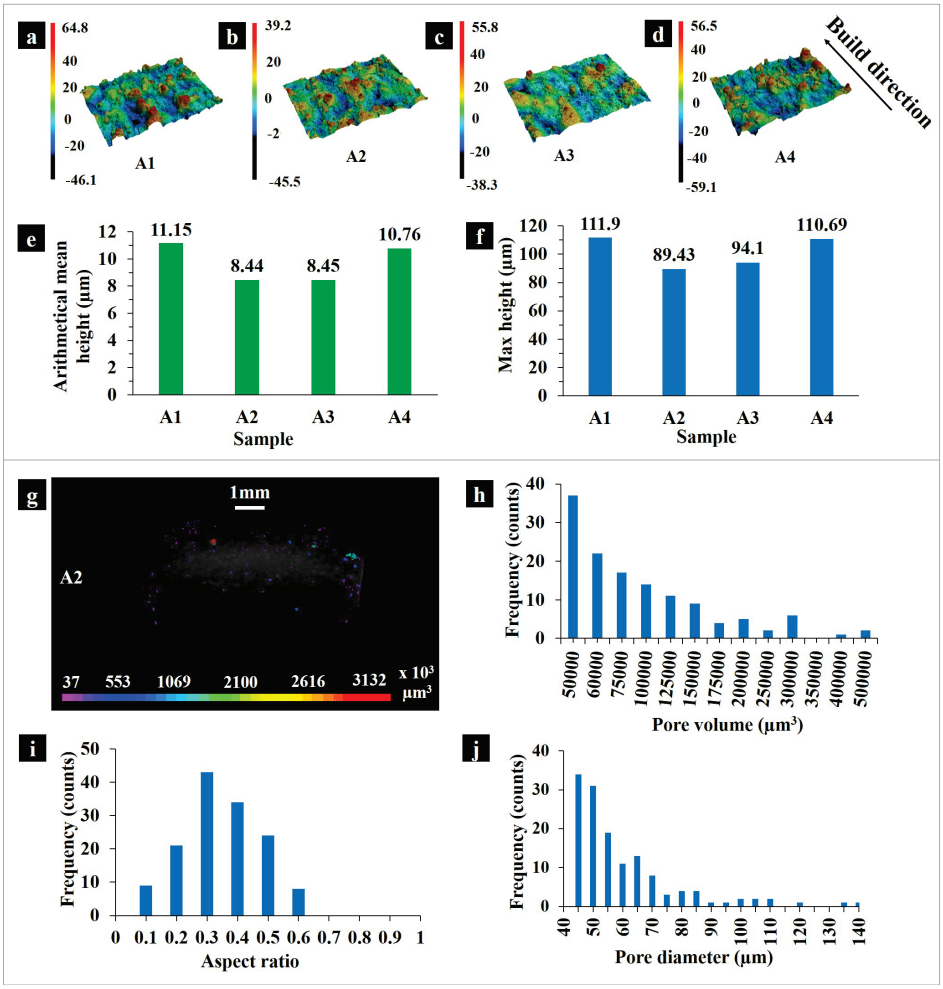

*Figure 23.The side surface profiles (a-d), average arithmetical mean height (Sa) (e) and average maximum height (Sz) for samples A1-A4 (f), 3D microscan of as-built sample A2 (g) and analysis of X-ray CT results: pore volume (h), aspect ratio (i), and diameter (j) distribution (adapted from **Paper III**).*

The theoretical density was calculated to be 4.37 g·cm^{-3}, considering the content of constituent phases. Thus, the relative density of samples reaches up to 98-99%, and the hardness values are in the range of 424-496 HV1 and 417-498 HV5 (Table 7). Conclusively, successful in-situ fabrication of $Mo(Si,Al)_2$ based composite coupons from Mo+2Si+30 wt.% AlSi10Mg powder mixture.

Table 7. Density and hardness of samples A1-A4 ***(Paper III)***

Sample	Energy density	Relative density	Hardness	
(Name)	(J·mm^{-3})	(%)	(HV1)	(HV5)
A1	67.2	97.9	424±10	417±11
A2	83.9	99.0	490±15	477±20
A3	95.3	98.3	496±12	498±17
A4	112.0	98.8	476±19	450±15

3.3 System 2. $Mo(Si,Al)_2$-based composite preparation. Routine 2.

Powders

The powder feedstock for $Mo(Si,Al)_2$-based material preparation consists of a mixture of gas atomized AlSi10Mg alloy and combustion synthesized $MoSi_2$ powders at a 30 wt.% : 70 wt.% ratio. The SEM image of AlSi10Mg powder is shown in Fig. 24a. The size of spherical AlSi10Mg powder range from 15 µm to 63 µm with a Gaussian distribution centered on 38 µm. $MoSi_2$ powder is composed of agglomerates of fine (1-5 µm) particles, Fig. 24b, with D10 =5.4 µm, D50 = 18.9 µm, D90 = 43.4 µm (**Paper IV).** The SEM image of $MoSi_2$-30 wt.% AlSi10Mg powder mixture (Fig. 24c) points clear differentiation of AlSi10Mg and $MoSi_2$ particle size. The $MoSi_2$-30 wt.% AlSi10Mg powder mixture has shown negatively skewed Gaussian size distribution, with D10 = 7.68 µm, D50 = 33.0 µm and D90 = 54.1 µm.

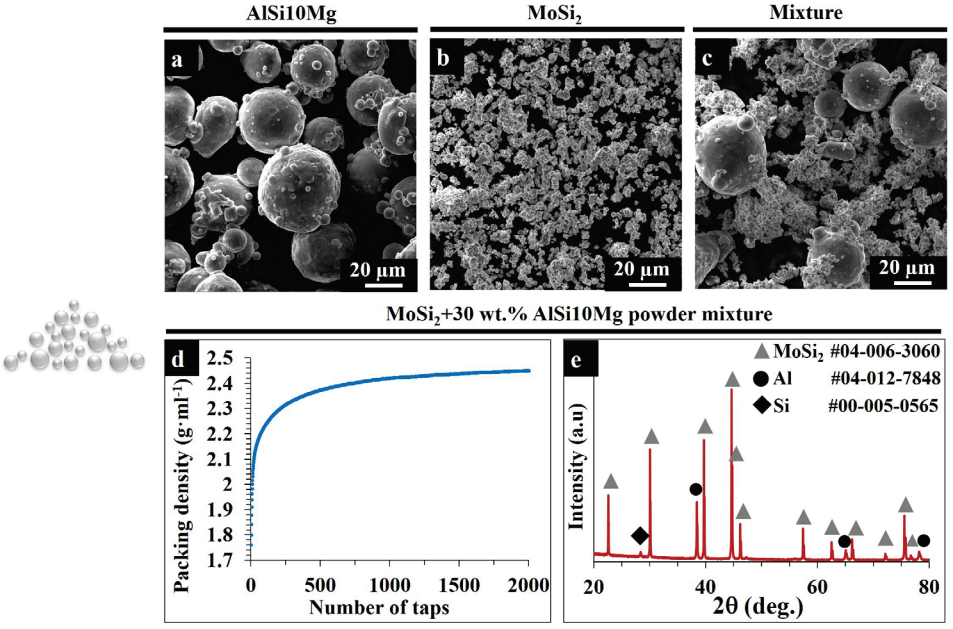

Figure 24.SEM images of AlSi10Mg alloy (a), SHS prepared $MoSi_2$ (b) and $MoSi_2$-30 wt.% AlSi10Mg mixture (c). Average packing density as a function of stress (d) and XRD pattern (e) of $MoSi_2$-30 wt.% AlSi10Mg powder mixture ***(adapted from Paper IV).***

The powders with negatively skewed Gaussian size distribution have high packing density, due to small particles filling voids between the larger ones. The initial bulk density of the $MoSi_2$-30 wt.% AlSi10Mg powder mixture was measured as 1.76±0.012 $g \cdot ml^{-1}$, after 2000 taps the bulk density increased up to 2.45±0.048 $g \cdot ml^{-1}$ and the packing density after extrapolation was 2.62±0.064 $g \cdot ml^{-1}$, because of fine $MoSi_2$ particles occupying the vacancies between relatively bigger AlSi10Mg particles (Fig. 24d).

The XRD pattern of $MoSi_2$-30 wt.% AlSi10Mg powder shows the corresponding peaks of tetragonal C11b $MoSi_2$ and face centered Al and Si (Fig. 24e).

The basic flowability energy of AlSi10Mg, $MoSi_2$-30 wt.% AlSi10Mg and $MoSi_2$ are ~206 mJ, 252 mJ and 307 mJ, respectively, and stability index (SI) around ~1 **(Paper IV)**. The flowability of the $MoSi_2$-30 wt.% AlSi10Mg mixture can be considered as fair, thus the powder is suitable for SLM processing.

Bulks

The disclosed pores of samples E6, E10 and E16 are visualized in Fig. 25 (colored from pink to red). The level of porosity determined by calculating the pore and part voxels is less than 1%, meaning that relative density of the samples exceed 99%.

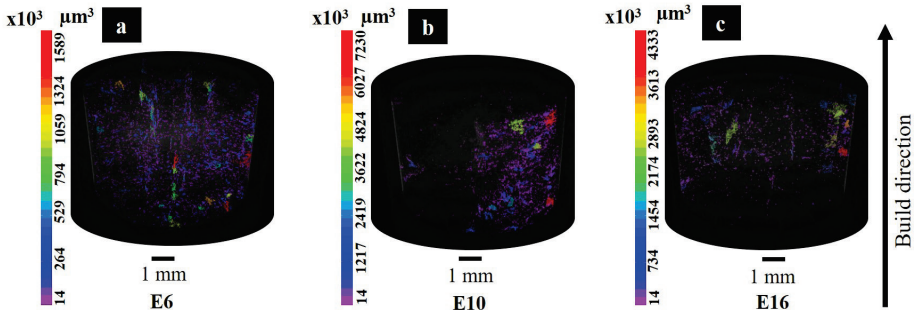

Figure 25. 3D visualization of porosity in as-built samples E6 (a), E10 (b) and E16 (c) (pores are labelled by volume (µm³)) ***(adapted from Paper IV).***

The analysis of X-ray CT scans revealing the pore size, distribution and respective pore aspect ratio for samples E6, E10 and E16 are illustrated in Fig. 26.

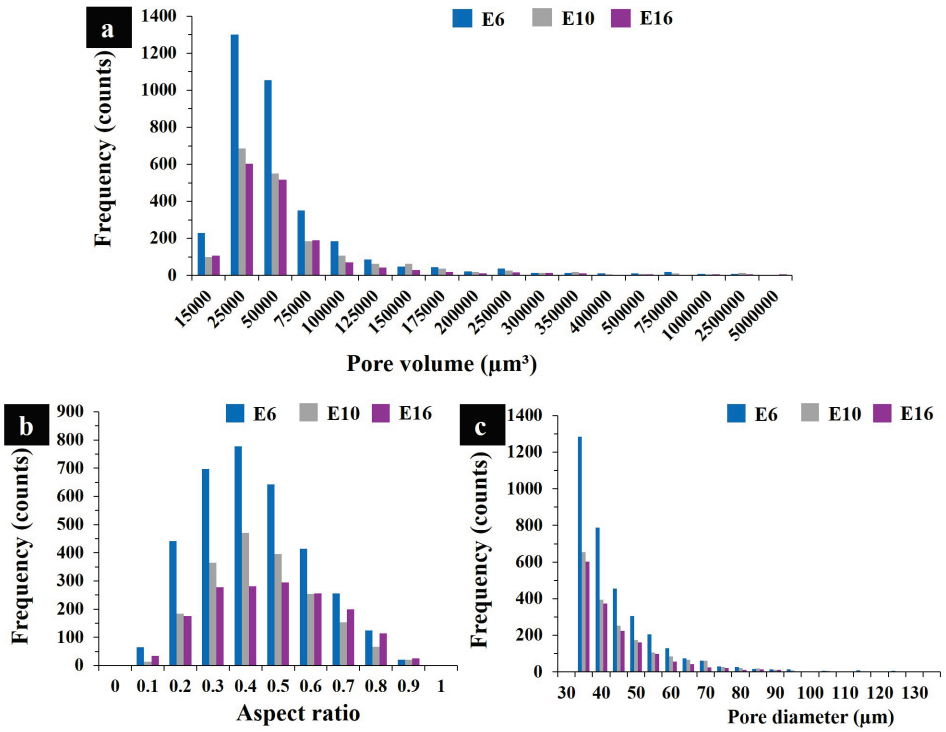

Figure 26. X-ray CT results: pore volume distribution (a), aspect ratio of the pores (b), pore diameter distribution (c) in as-built samples E6, E10 and E16 ***(adapted from Paper IV).***

For samples E6 and E10, the maximum counts were detected for the pores having aspect ratio of 0.4, while for E16, majority of the pores had the aspect ratio of 0.5 (Fig. 26c). This explains that samples E6 and E10 has high number of more elongated and

irregularly shaped pores, compared to E16, which has more rounded pores. The greater number of pores for analyzed samples are in 30-35 µm size range.

The top surface profiles of samples E5, E6, E9, E10, E13 and E16 are displayed in Fig. 27, and the average top surface roughness (Sa) and the maximum height (Sz) derived from surface profiles are presented in Fig. 28. SLM manufactured part quality and surface characteristics are dependent on process parameters to a great extent.

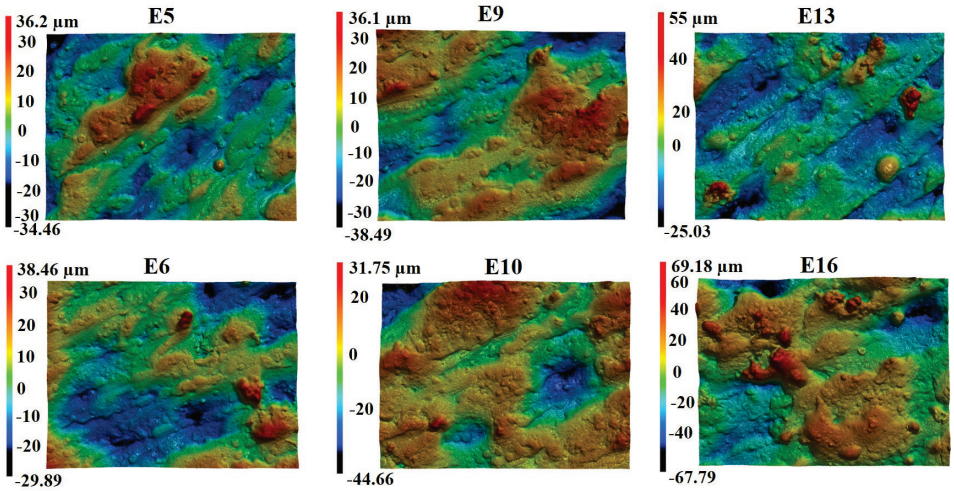

Figure 27.Top surface profiles of samples E5, E6, E9, E10, E13 and E16 ***(adapted from Paper V).***

Increased scanning speed at fixed laser power drives to increase of top surface unevenness, withal disturbing the dimensional accuracy of printed objects. While, at the same scanning speed, parts fabricated at higher applied laser power display relatively flat surface (e.g. samples E1-E5-E9 and E4-E8-E12). In case of applying low 100 W laser power, the samples (E1-E4) possess deep valleys and high peaks, resulted by inadequate melting of consecutive powder layers, as the process is proceeding beyond the melting mode.

The laser scan tracks are clearly seen at top surface profiles of samples E6 and E13 (Fig. 27). The almost spherical shaped particles adhered on the top surfaces of the samples (colored with yellow, orange and red) portray the spattered particles, as a consequence of splashing droplets from melt pool. The EDS analysis revealed that these trapped particles embody surface oxidized Al alloy, which prevent the wettability between melt pool and the substratal layer resulting in ragged surface. (Wang, 2016).

At the combination of higher laser powers (150-300 W) and high scanning speeds (1000-1500 mm·s^{-1}), during powder bed fusion shallow melt pools are being generated, which inadequately wets the preceding solidified layer. The latter results to shrinkage of molten tracks leading to balling phenomenon owing to the tension between the scan tracks' interfaces.

Relatively smooth surfaces were developed for samples E5, E6, E9, E10, E11 and E13 as evaluated Sa was in 9-11 µm range (Fig. 28), as when moderate scan speed is used, there is sufficient solidification time for melt pool relaxation and solidification, leading to an even surface finish. (Strano, 2013). The gradual growth of estimated max height was noticed, when scan speed was increased at stated laser power (Fig. 28). Samples E9, E10 and E11 manufactured at 200 W laser power and moderate 400-700 mm·s^{-1} scan speed,

portray moderate maximum height results. Sample E16 produced at the highest applied laser power shows inferior surface quality in comparison with E9-E11 samples. The reason behind is rapid solidification and not sufficient relaxation time for the melt pool, accompanied by insufficient capillary forces for powder fusion, resulting rippling on the surface and degrading the surface quality.

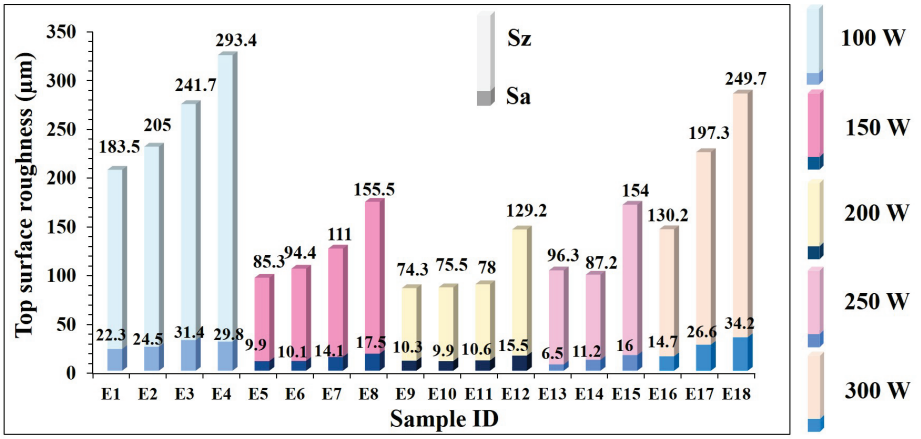

Figure 28.Top surface roughness results of samples E1-E18 (standard deviation is less than 10%) ***(adapted from Paper V).***

Phase composition

Fig. 29 shows the polished top surface XRD patterns for the samples E10 (a) and E4 (b). The diffractogram of sample E4 reveals the presence of unreacted tetragonal $MoSi_2$, face centered cubic Al, the substituted face centered cubic Si phases, duplex, in-situ formed $Mo_3(Al_2Si_4)/MoAl_{0.6}Si_{1.4}$ phases (resembling $Mo(Si_{1-x},Al_x)_2$, x=0.3-0.33 composition) with hexagonal lattice structure and Si enriched Al rich $Al_{0.85}Si_{0.15}$ phase.

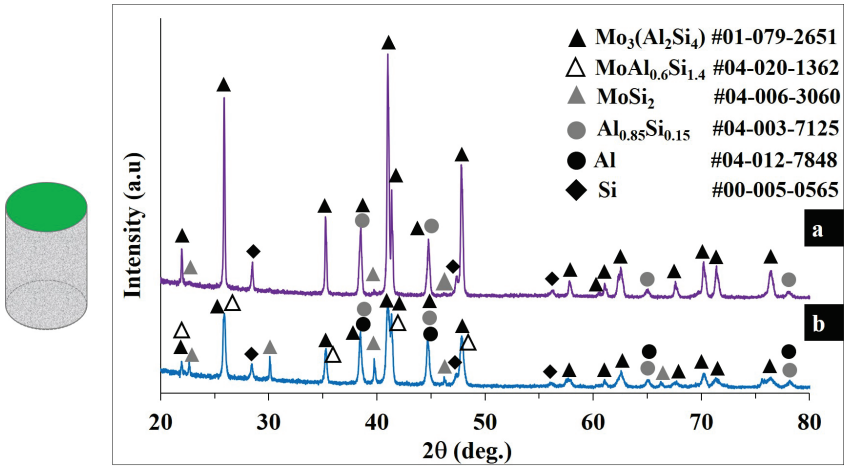

Figure 29.Surface XRD pattern of the samples E10 (a) and E4 (b) ***(adapted from Paper IV).***

The diffractogram of E10 shows almost complete $MoSi_2$ phase transformation to C40 molybdenum aluminosilicide with subtle peaks of unreacted C11b and minor aluminum lean $MoAl_{0.6}Si_{1.4}$. It reveals the formation of $Al_{0.85}Si_{0.15}$ phase and replaced Si. In case of low applied energy density, the reaction between $MoSi_2$ and AlSi10Mg is incomplete,

which results in unreacted $MoSi_2$ and face centered cubic Al phase in the produced material. In E10, no Al was detected, but Si saturated Al rich $Al_{0.85}Si_{0.15}$ phase. It is important to note that under chosen conditions (33.6-168.0 $J \cdot mm^{-3}$ energy density), the addition of AlSi10Mg to the $MoSi_2$ demonstrates that C11b tetragonal lattice of $MoSi_2$ widens until hexagonal $Mo(Si_{0.67}Al_{0.33})_2$ (x=0.33 mol) structure, and no further C40 lattice transformation to form Al rich orthorhombic C54 structure is observed. Similar results have been obtained in Routine 1 **(Paper III)**, where mixture of Mo, Si and Al alloy were used as feedstock. It was disclosed, that the increase in scanning speed at fixed laser power, leads to incomplete single displacement reaction of $MoSi_2$ and aluminum, causing chemical and compositional inhomogeneity. The theoretical density is averaged considering slightly different compositions of the samples and the certainty level of the Rietveld refinement method and is calculated to be 4.37 $g \cdot cm^{-3}$. The relative density is calculated in relation to this number.

Microstructural analysis

The SEM images of polished top and side surfaces of samples E10 and E12 are illustrated in Fig. 30. The areas highlighted with elliptical orange dashed-lines in Fig. 30 a and c point the melt pool cores. After laser scanning, different regions of generated melt pools have different solidification modes, caused by the gradient thermal distribution. The latter results in the formation of diverse microstructure in the manufactured components. The variation of local thermal histories between the center and the edge of the melt pool makes the melt pool visible after polishing. The microstructure of the elliptical melt pool cores comprises of sub-micron to 1-micron structures (Fig. 30 a). Meantime at the boundary of each elliptical section, the coarser columnar dendrites are observed in the perpendicular direction of stacking, as the edges are exposed to longer laser treatment because of the overlap of adjacent scan tracks. The dendritic growth is caused by the non-homogeneous nucleation taking place ahead of the liquid-solid interface. Sample E10 has homogeneous microstructure, while sample E12 printed at high 1000 $mm \cdot s^{-1}$ scan speed shows inhomogeneous morphological texture and underdeveloped non-continuous melt pools, as the fabrication process was beyond melting zone. The orange dashed curve in Fig. 30b shows the morphological transition zone of fine grains of melt pool core and the heat affected overlapped regions.

Fig. 30 e and g show the vertical side fracture of the samples E10 and E12. The semi-elliptical dashes highlight the melt pool cores in X-Z direction (parallel to build direction). And the orange dashed curve in Fig. 30f shows the morphological transition zone, like in case of top surface. In sample E12 it was challenging to find melt pools, as the procedure was in sintering mode.

When compared the microstructural features of samples produced by routine 1 and 2, and taking step back to Figure 20, it can be noted that samples A2 and E10 possess almost full densification, but have different morphological textures. Both top surface and side fracture of sample A2 are composed of columnar dendrites, while for sample E10 the melt pool solidification mode is duplex cellular (cellular dendritic) and columnar dendritic on the top surface and columnar dendritic on the side fracture. This means, that the cellular grains on the top surface are the tips of the elongated columnar dendrites observed in the fracture. Grain coarsening in the periphery of solidified melt pools was observed in both cases due to the overlapping of the consecutive and adjacent melt pools. The formation of columnar dendrites all over the sample A2 can be conditioned by the internal heat released during the exothermic Mo-Si-Al interaction

combined with external heat from provided by laser beam. Thus, it makes a large thermal gradient between the border and the center of melt pool, promoting the formation of dendritic crystals together with the center segregation of Al-Si rich phase.

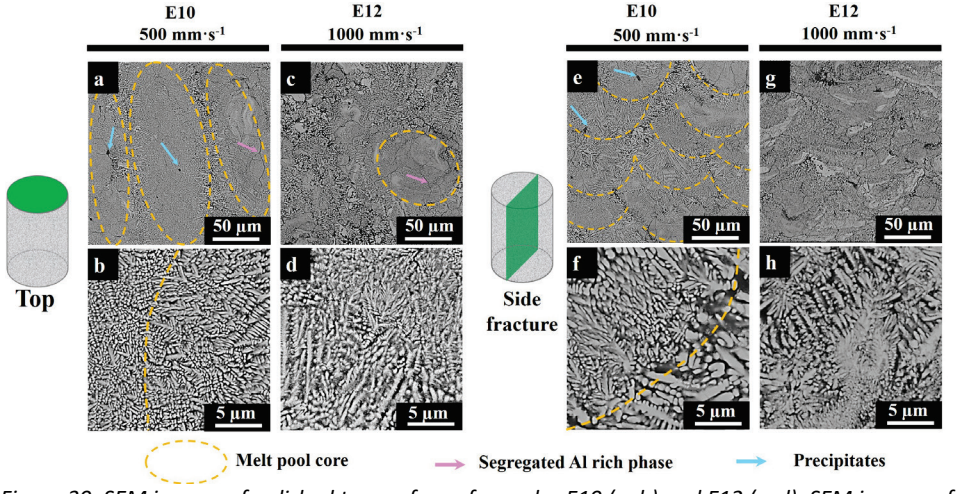

Figure 30. SEM images of polished top surface of samples E10 (a, b) and E12 (c, d). SEM images of the side fracture of samples E10 (e, f) and E12 (g, h) ***(adapted from paper V).***

Fig. 31 a and b show the top surface secondary electron and backscattered electron images of sample E10, respectively.

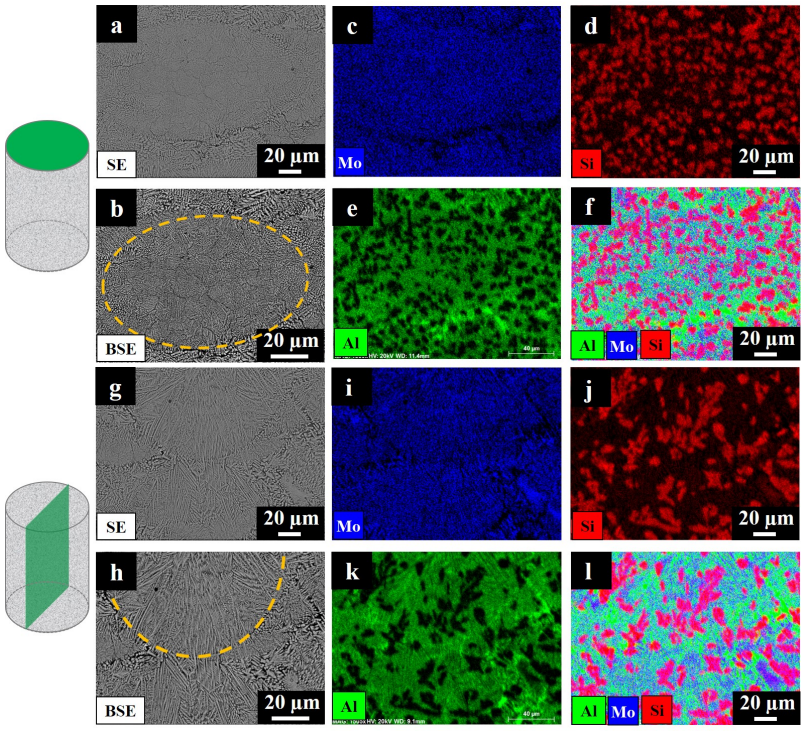

Figure 31. Top SE image (a), BSE image (b), corresponding EDS maps (c-f), and side surface SE image (g), BSE image (h) and respective EDS maps (i-l) of sample E10 ***(adapted from paper IV).***

Fig. 31 c, d, e show the corresponding elemental maps of Mo, Si and Al and mixed EDS map is shown in Fig. 31 (f). Molybdenum signals are recorded from across the sample except in the darker regions which corresponds to interdendritic Al rich phase (Fig 31d bright green regions). Silicon is also observed among all analyzed zone, while the radiant red sections reveal the existence of replaced free silicon, where no aluminum signal is registered. Fig. 31 g and h show the SE and BSE images of the polished side fracture of sample E10. The orange dashed regions (Fig. 31h) represent the melt pool core. The EDS maps corresponding to Fig. 31 g SEM image reveal the similar elemental composition as for the top surface of the sample (Fig. 31 i-l). Most of the studied area is composed of Mo-Si-Al containing phase, which is revealed to be $Mo(Si_{1-x},Al_x)_2$ at x=0.33 mole, while in the dark regions observed in Fig. 31 g, the absence of Mo and presence of Al rich phase is revealed ($Al_{0.85}Si_{0.15}$). The black regions in Al green map and bright red regions in Si map reveal that there is substituted Si phase, meaning that Al partially replaced Si, being in agreement with XRD results.

Density and hardness of produced E1-E18 parts

Fig. 32 shows the relative geometric, relative Archimedes density results and Vickers hardness values at 1 and 5 kg load. For samples E3 and E4 Archimedes density is not estimated, because of huge open porosity. The increase in scan speed in sets E1-E4, E5-E8, E9-E12, E13-E15 and E16-E18, results the drop in density values, caused by insufficient energy applied for powder fusion (Fig. 32).

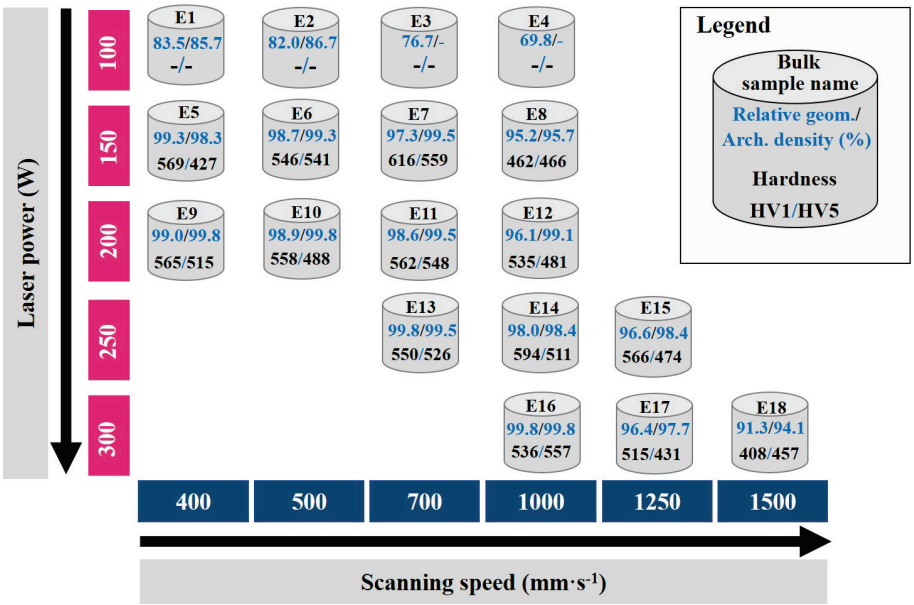

Figure 32. Relative geometric, relative Archimedes densities, HV1 and HV5 hardness values for E1-E18 samples ***(adapted from Paper V)****.*

In the vertically arranged sample sets of E1-E9, E2-E10, E3-E13, E4-E16 and E15-E7, where the laser power is ramped up to 50 W (step size), the density values progressively grow as the applied energy completely melts the deposited powder layers ensuring adequate bonding between consecutive and adjacent layers. Samples E15, E17 and E18 produced at relatively high 250-300 W laser power and high 1250-1500 $mm{\cdot}s^{-1}$ scanning speeds show inferior densification behavior (Fig. 32).

To provide the reliable hardness results, the indentations were made at 9.8 N and 49 N force, as the indentation mark after applying 9.8 N force is small and results higher deviation. Due to relatively high porosity, it was not possible to evaluate the hardness for samples E1-E4. When a 9.8 N force is applied samples E8 and E18 produced at 50.4 J·mm^{-3} and 67 J·mm^{-3} energy density, respectively, yielded to hardness less than 500 HV1, which is caused by heterogeneity of developed microstructure. For the rest of samples, hardness of up to 594 HV1 (E14) and for sample E7 up to 618 HV1 are measured. When the applied force is 49 N, hardness in 427-559 HV5 range is observed (Fig. 32).

According to the scheme showing the relationship of process parameters and built part characteristics (Fig. 33), samples E5, E6, E9, E10 and E13 possess high density, high hardness, moderate surface roughness, high microstructural and compositional homogeneity and can be applicable for industrial use.

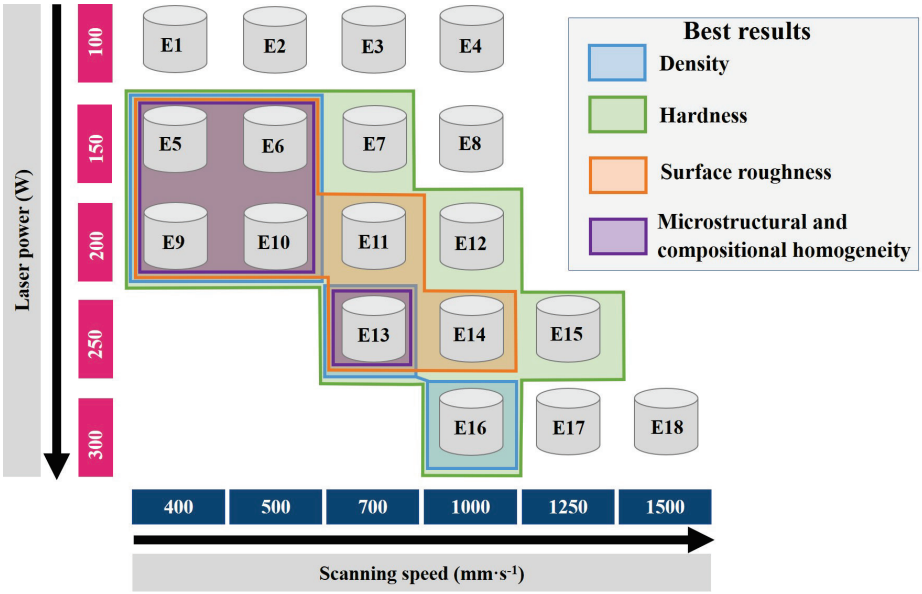

Figure 33.Revealed influence of process parameters on $Mo(Si_{1-x},Al_x)_2$-based part characteristics fabricated by routine 2.

For the comparison of the molybdenum aluminosilicide based composite preparation by routine 1 and 2, it can be noted that almost full density samples were produced following the both approaches. The hardness up to 500 HV1 and HV5 was achieved for samples prepared by routine 1, while hardness reached up to 600 HV1 and HV5 for the samples prepared by routine 2. This can be explained by different microstructural features of the samples.

The primary distinctive feature for routines 1 and 2 is the interaction nature of the reactants. In case of routine 1, the Mo-Si-Al reaction is comparably exothermic, which makes challenges to estimate the real influence of the energy supplied by laser beam, while in case of routine 2 the reaction between $MoSi_2$ and aluminum is weak exothermic, allowing a better control of applied laser energy. For this reason routine 2 appears more advantageous. However, the complex physics behind the process and the complex chemistry of the Mo-Si-Al combination reaction make the system quite interesting for deeper analysis and comparison of experimental results with thermodynamic calculations, and correspondence with phase diagrams.

4 Conclusions

The main targets of this work were development and manufacturing of novel $MoSi_2$-containing powders feedstock suitable for SLS/SLM processing and printing reliable items using the developed powders. The prepared feedstocks were subjected to SLM, and the consolidated structures were characterized.

From this study, the following conclusions can be drawn:

1. The method of self-propagating high-temperature synthesis allows production of $MoSi_2$/10-13 wt.% Si composite powders feedstock, possessing fair flowability and high packing density, which is applicable for SLM processing.
2. $MoSi_2$/10-13 wt.% Si bulks were successfully manufactured via SLM process reaching to 90 % relative density, homogeneous microstructure and hardness of 10.9 GPa.
3. Cellular ceramic lattices of $MoSi_2$-Si_3N_4 were prepared with the help of subsequent nitridation of $MoSi_2$/Si structures keeping the original lattice design and period size. Parametric study of SLM consolidation of $MoSi_2$-13 wt.% Si powder showed that applying 36-60 W laser power at fixed 80 $mm \cdot s^{-1}$ scanning speed, the dimensions (300-350 µm strut diameter, 750-850 µm pore size) and porosity level (up to 35% apparent relative density, 65% porosity) of prepared lattices are in close correspondence with CAD model.
4. For the first time, the successful consolidation of $MoSi_2$-30 wt.% AlSi10Mg and Mo-2Si-30 wt.% AlSi10Mg powders was conducted by SLM yielding the preparation of C40 hexagonal $Mo(Si_{1-x},Al_x)_2$ (molybdenum aluminosilicide) based composites.
5. For SLM of Mo-2Si-30 wt.% AlSi10Mg powder, the influence of scanning speed (300-500 $mm \cdot s^{-1}$) was studied at fixed laser power (100 W), layer thickness (35 µm) and hatching space (85 µm), showing that under all chosen parameters, the solubility limit of Al in $Mo(Si_{1-x},Al_x)_2$ was 0.33 mole regardless the excess amount of AlSi10Mg in the reactants' mixture. Samples consist of fine columnar dendrites and display up to 99% relative density, ~496 HV1 and 498 HV5 hardness and moderate 8.4-11.1 µm side surface roughness (Sa).
6. For SLM of $MoSi_2$-30 wt.% AlSi10Mg powder mixture, the influence of scanning speed (400-1500 $mm \cdot s^{-1}$) and laser power (100-300 W) was studied at a fixed layer thickness (35 µm) and hatching space (85 µm). It was shown, that samples produced at 150-200 W and 400-500 $mm \cdot s^{-1}$ scan speed, as well as 250 W laser power and 700 $mm \cdot s^{-1}$ scan speed, possess 6.5-10.3 µm top and 10.5-13.2 µm side surface roughness, up to 99.8% relative density, up to 570 HV1 and 540 HV5 hardness along with remarkable chemical and microstructural homogeneity. The SEM examination of the cross section revealed that the solidified melt pools are constructed by well oriented fine columnar dendrites of $Mo(Si_{1-x},Al_x)_2$ x=0.33, while the heat affecting zones surrounding the melt pools consist of misoriented coarser dendritic structures along with

$Al_{0.85}Si_{0.15}$ and substituted Si phases. A low laser power (100 W) and applied high scan speeds (1000-1500 $mm \cdot s^{-1}$) are leading to unreacted $MoSi_2$ and the formation of Al lean $Mo(Si_{1-x},Al_x)_2$ x=0.3 mole, disturbing both microstructural and chemical homogeneity of the printed parts.

5 Future work

Continuing the research briefly introduced in thesis, further investigations are going to be performed in future, such as:

- Oxidation tests of SLM built $Mo(Si,Al)_2$-based composites at intermediate (500-700^oC) and high temperatures (>1600^oC);
- Preparation of $Mo(Si_{1-x},Al_x)_2$-based composites with different compositions (by changing the ratio of initial reactants) via selective laser melting technique;
- Parametric study and SLM process optimization of newly developed $Mo(Si_{1-x},Al_x)_2$-based composites;
- Preparation of $MoSi_2$-Si_3N_4 lattices with new model design for specific applications.

References

Aboulkhair, N. T. (2014). Reducing porosity in AlSi10Mg parts processed by selective laser melting. *Additive Manufacturing, 1*, 77-86.

AlMangour, B. (2016). Selective laser melting of TiC reinforced 316L stainless steel matrix nanocomposites: Influence of starting TiC particle size and volume content. *Materials & Design, 104*, 141-151.

Anwar, A. B. (2017). Selective laser melting of AlSi10Mg: Effects of scan direction, part placement and inert gas flow velocity on tensile strength. *Journal of Materials Processing Technology, 240*, 388-396.

Attar, H. (2014a). Manufacture by selective laser melting and mechanical behavior of commercially pure titanium. *Materials Science and Engineering: A, 593*, 170-177.

Attar, H. (2014b). Selective laser melting of in situ titanium–titanium boride composites: processing, microstructure and mechanical properties. *Acta Materialia, 76*, 13-22.

Attar, H. (2015). Effect of powder particle shape on the properties of in situ Ti-TiB composite materials produced by selective laser melting. *Journal of Materials Science & Technology, 31*(10), 1001-1005.

Attaran, M. (2017). The rise of 3-D printing: The advantages of additive manufacturing over traditional manufacturing. *Business Horizons, 60*(5), 677-688.

Balla, V. K. (2008). Processing of bulk alumina ceramics using laser engineered net shaping. *International Journal of Applied Ceramic Technology, 5*(3), 234–242.

Bartlett, A. H. (1998). Elevated temperature mechanical properties of MoSi2/Si3N4, MoSi2/SiC composites produced by self-propagating high temperature synthesis. *Journal of materials science, 33*(6), 1653-1660.

Bourell, D. (2011). Influence of the particle size distribution on surface quality and mechanical properties in AM steel parts. *Rapid Prototyping Journal, 17*, 195-202.

Brandt, M. (2016). *Laser additive manufacturing: materials, design, technologies, and applications.* United Kingdom: Woodhead Publishing.

Cappi, B. (2011). Rheological properties of aqueous Si3N4 and MoSi2 suspensions tailor-made for direct inkjet printing. *Journal of the American Ceramic Society, 94*(1), 111-116.

Choe, H. (1997). The effect of powder processing on the coefficient of thermal expansion of MoSi2-Si3N4 composites. *Materials Science and Engineering: A, 237*(2), 250-255.

Choi, S. R. (1998). Elevated-Temperature Slow Crack Growth and Room-Temperature Properties of MoSi2-50 vol% Si3N4 Composites. *In 22nd Annual Conference on Composites, Advanced Ceramics, Materials,and Structures: A: Ceramic Engineering and Science Proceeding. 19*, pp. 361-369. NJ: John Wiley & Sons, Inc.

Costa e Silva, A. (1993). Microstructural modification of MoSi2 through aluminum additions. *Scripta metallurgica et materialia, 29*(8), 1141-1145.

Cotton, J. D. (1991). Intrinisic second-phase particles in powder-processed MoSi2. *Materials Science and Engineering: A, 144*(1-2), 287-291.

Dadbakhsh, S. (2014). Effect of Fe2O3 content on microstructure of Al powder consolidated parts via selective laser melting using various laser powers and speeds. *The International Journal of Advanced Manufacturing Technology, 73*(9-12), 1453-1463.

Dasgupta, T. (2007). Thermal properties of MoSi2 with minor aluminum substitutions. *Intermetallics, 15*(2), 128-132.

Deckers, J. (2014). Additive manufacturing of ceramics: a review. *Journal of Ceramic Science and Technology, 5*(4), 245-260.

Deevi, S. C. (1992). Diffusional reactions in the combustion synthesis of MoSi2. *Materials Science and Engineering: A, 149*(2), 241-251.

Delroisse, P. (2017). Effect of strut orientation on the microstructure heterogeneities in AlSi10Mg lattices processed by selective laser melting. *Scripta Materialia, 141*, 32-35.

Ding, X. (2017). Heat transfer and fluid flow of molten pool during selective laser melting of AlSi10Mg powder: Simulation and experiment. *Journal of Manufacturing Processes, 26*, 280-289.

Esmaeilizadeh, R. (2019). On the effect of spatter particles distribution on the quality of Hastelloy X parts made by laser powder-bed fusion additive manufacturing. *Journal of Maufacturing Processes, 37*, 11-20.

Ford, S. (2016). Additive manufacturing and sustainability: an exploratory study of the advantages and challenges. *Journal of cleaner Production, 137*(1), 573-1587.

Gabrielyan, A. V. (2008). Comparative study of combustion laws for Mo–Si–N and W–Si–N ternary systems. *Journal of alloys and compounds, 454*(1-2), 394-399.

Ghayoumabadi, M. E. (2009). Lattice variations and phase evolutions during combustion reactions in Mo–Si–Al system. *Journal of Alloys and Compounds, 472*(1-2), 84-90.

Gu, D. (2012). Selective laser melting of TiC/Ti bulk nanocomposites: Influence of nanoscale reinforcement. *Scripta Materialia, 67*(2), 185-188.

Guo, N. (2013). Additive manufacturing: technology, applications and research needs. *Frontiers of Mechanical Engineering, 8*(3), 215-243.

Hagihara, K. (2017). Successful additive manufacturing of MoSi2 including crystallographic texture and shape control. *Journal of Alloys and Compounds, 696*, 67-72.

Harada, Y. (1998). Solid solution softening and hardening in alloyed MoSi2. *Intermetallics, 6*(6), 529-535.

Harrison, N. J. (2015). Reduction of micro-cracking in nickel superalloys processed by Selective Laser Melting: A fundamental alloy design approach. *Acta Materialia, 94*, 59-68.

Hebsur, M. G. (2001). Development of Tough, Strong, and Pest-Resistant MoSi2-(Beta) Si3N4 Composites for High-Temperature Structural Applications. *International symposium of structural intermetallics.* Wyoming, USA: Minerals, Metals & Materials Society.

Hou, H. D. (2016). Preparation of Mo (Si, Al) 2 feedstock used for air plasma spraying. *Transactions of Nonferrous Metals Society of China, 26*(11), 2939-2946.

Ingemarsson, L. (2011). Oxidation behaviour of a Mo (Si, Al) 2 based composite at 1500° C. *Intermetallics, 19*(9), 1319-1329.

ISO 13314:2011. (n.d.). Mechanical testing of metals — Ductility testing — Compression test for porous and cellular metals.

Iveković, A. O. (2018). Selective laser melting of tungsten and tungsten alloys. *International Journal of Refractory Metals and Hard Materials, 72*, 27-32.

Jhabvala, J. (2010). On the effect of scanning strategies in the selective laser melting process. *Virtual and physical prototyping, 5*(2), 99-109.

Jo, S. W. (1996). On the formation of MoSi2 by self-propagating high-temperature synthesis. *Acta materialia, 44*(1), 4317-4326.

Kempen, K. (2014). Selective laser melting of crack-free high density M2 high speed steel parts by baseplate preheating. *Journal of Manufacturing Science and Engineering, 136*(6).

King, W. E. (2015). Laser powder bed fusion additive manufacturing of metals; physics, computational, and materials challenges. *Applied Physics Reviews, 2*(4), 041304.

Ko, I. Y. (2010). Properties and densification of nanocrystalline MoSi2–Si3N4 composite from mechanically alloyed powders by pulsed current-activated sintering. *Journal of alloys and compounds, 502*(1), L10-L13.

Kühnle, T. (2012). In-situ formation of titanium boride and titanium carbide by selective laser melting. *Physics Procedia, 39*, 432-438.

Kushan, M. C. (2012). *Potential of MoSi2 and MoSi2-Si3N4 composites for aircraft gas turbine engines. Recent Advances in Aircraft Technology.* (A. R. K., Ed.) Croatia: InTech.

Lee, P. Y. (1995). Synthesis of MoSi2 powder by mechanical alloying. *Materials Science and Engineering: A, 192*, 556-562.

Liao, H. (2019). Alumina loss mechanism of Al2O3-AlSi10 Mg composites during selective laser melting. *Journal of Alloys and Compounds, 785*, 286-295.

Liu, L. (1995). Solid state reactions induced by mechanical alloying in metal-silicon (metal= Mo, Nb) systems. *Acta metallurgica et materialia, 43*(10), 3755-3761.

Liu, L. (2020a). SHS Produced TiB2-Si Powders for Selective Laser Melting of Ceramic-Based Composite. *Applied Sciences, 10*(9), 3283.

Liu, L. (2020b). Selective laser melting of TiB2-Ti composite with high content of ceramic phase. *Ceramics International*, 21128-21135.

Liu, Y. (2000). Thermodynamic reassessment of the Mo–Si and Al–Mo–Si systems. *Intermetallics, 8*(8), 953-962.

Liu, Z. H. (2013). Crystal structure analysis of M2 high speed steel parts produced by selective laser melting. *Materials characterization, 84*, 72-80.

Luo, S. (2020). Selective laser melting of dual phase AlCrCuFeNix high entropy alloys: Formability, heterogeneous microstructures and deformation mechanisms. *Additive Manufacturing, 31*, 100925.

Majeed, A. (2019). An investigation into the influence of processing parameters on the surface quality of AlSi10Mg parts by SLM process. *In 2019 16th international bhurban conference on applied sciences and technology (IBCAST)* (pp. 143-147). IEEE.

Manukyan, K. V. (2008). Molten salt-assisted combustion synthesis and characterization of MoSi2 and MoSi2-Si3N4 composite powders. *Chemical engineering journal, 143*(1-3), 331-336.

Manukyan, K. V. (2009). MoSi2–Si3N4 composites: Influence of starting materials and fabrication route on electrical and mechanical properties. *Journal of the European Ceramic Society, 29*(10), 2053-2060.

Maruyama, T. (1997). High temperature oxidation and pesting of Mo (Si, Al) 2. *Materials Science and Engineering: A, 239*, 828-841.

Merzhanov, A. G. (2004). The chemistry of self-propagating high-temperature synthesis. *Journal of Materials Chemistry, 14*(12), 1779-1786.

Minasyan, T. (2018). Mo–Cu pseudoalloys by combustion synthesis and spark plasma sintering. *Journal of Materials Science, 53*(24), 16598-16608.

Minasyan, T. (2019). Selective Laser Melting of Ti/cBN Composite. *In Key Engineering Materials, 799*, 257-262.

Mitra, R. (2015). *Silicides: Processing and Mechanical Behavior. In Structural Intermetallics and Intermetallic Matrix Composites* (Vol. 6). New York, USA: CRC Press.

Mossino, P. (2004). Some aspects in self-propagating high-temperature synthesis. *Ceramics International, 30*(3), 311-332.

Munir, K. S. (2017). *Metallic scaffolds manufactured by selective laser melting for biomedical applications.* United Kingdom: Woodhead Publishing.

Nanko, M. (2001). Formation of Mo (Si, Al) 2 layer on Mo dipped in Al melt saturated with Si and the effects of transition metals added in the melt. Intermetallics. *Intermetallics, 9*(7), 637-646.

Ngo, T. D. (2018). Additive manufacturing (3D printing): A review of materials, methods, applications and challenges. *Composites Part B: Engineering, 143*, 172-196.

Pan, Y. (2017). Probing the balance between ductility and strength: transition metal silicides. *Physical Chemistry Chemical Physics, 19*(29), 19427-19433.

Pan, Y. (2018). Insight into the oxidation mechanism of MoSi2: Ab-initio calculations. *Ceramics International, 44*(16), 19583-19589.

Patel, S. (2020). Melting Modes in Laser Powder Bed Fusion. *Materialia*, 100591.

Pinkerton, A. J. (2016). Lasers in additive manufacturing. *Optics & Laser Technology, 78*, 25-32.

Prakash, K. S. (2018). Additive manufacturing techniques in manufacturing - an overview. *Materials Today: Proceedings, 5*(2), 3873-3882.

Ramberg, C. E. (2000). Fabrication and High-Temperature Phase Stability of Mo (Al, Si) 2—MoSi2 Intermetallics. *Journal of the American Ceramic Society, 83*(4), 946-948.

Revilla-León, M. (2017). Impression technique for a complete-arch prosthesis with multiple implants using additive manufacturing technologies. *The Journal of prosthetic dentistry, 117*(6), 714-720.

Salarian, M. (2020). Pore space characteristics and corresponding effect on tensile properties of Inconel 625 fabricated via laser powder bed fusion. *Materials Science and Engineering: A, 769*, 138525.

Sames, W. J. (2016). The metallurgy and processing science of metal additive manufacturing. *International Materials Reviews, 61*(5), 315-360.

Sharif, A. A. (2001). Alloying of MoSi2 for improved mechanical properties. *Intermetallics, 9*(10-11), 869-873.

Sharif, A. A. (2010). High-temperature oxidation of MoSi2. *Journal of materials science, 45*(4), 865-870.

Simonelli, M. (2014). Effect of the build orientation on the mechanical properties and fracture modes of SLM Ti–6Al–4V. *Materials Science and Engineering: A, 616*, 1-11.

Sing, S. L. (2017). Direct selective laser sintering and melting of ceramics: a review. *Rapid Prototyping Journal*, 611-623.

Slotwinski, J. A. (2014). Characterization of metal powders used for additive manufacturing. *Journal of research of the National Institute of Standards and Technology, 119*, 460.

Stergiou, A. (1994). Study of the effects of Al, Ta, W additions on the microstructure and properties of MoSi 2 base alloys. *MRS Online Proceedings Library Archive*, 364.

Strano, G. (2013). Surface roughness analysis, modelling and prediction in selective laser melting. *Journal of Materials Processing Technology, 213*(4), 589-597.

Sun, S. (2017b). Powder bed fusion processes: An overview. In *Laser Additive Manufacturing* (pp. 55-77). United Kingdom: Woodhead Publishing.

Sun, S. P. (2017a). Prediction of the mechanical properties of MoSi2 doped with Cr, Nb and W from first-principles calculations. *Journal of Alloys and Compounds, 714*, 459-466.

Sun, Z. (2016). Selective laser melting of stainless steel 316L with low porosity and high build rates. *Materials & Design, 104*, 197-204.

Sundberg, M. (2004). Alumina forming high temperature silicides and carbides. *Ceramics International, 30*(7), 1899-1904.

Suryanarayana, C. (2008). Structure and properties of ultrafine-grained MoSi2+ Si3N4 composites synthesized by mechanical alloying. *Materials Science and Engineering: A, 479*(1-2), 23-30.

Szost, B. A. (2016). A comparative study of additive manufacturing techniques: Residual stress and microstructural analysis of CLAD and WAAM printed Ti–6Al–4V components. *Materials and Design, 89*, 559-567.

Tan, J. H. (2017). An overview of powder granulometry on feedstock and part performance in the selective laser melting process. *Additive Manufacturing, 17*, 228-255.

Tang, H. P. (2015). Effect of powder reuse times on additive manufacturing of Ti-6Al-4V by selective electron beam melting. *Jom, 67*(3), 555-563.

Tolochko, N. K. (2000). Absorptance of powder materials suitable for laser sintering. *Rapid Prototyping Journal*, 155-160.

Vasudevan, A. K. (1992). A comparative overview of molybdenum disilicide composites. *Materials Science and Engineering: A, 155*(1-2), 1-17.

Vorotilo, S. (2018). Self-propagating high-temperature synthesis of nanocomposite ceramics TaSi2-SiC with hierarchical structure and superior properties. *Journal of the European Ceeramic Society, 38*(2), 433-443.

Wang, D. (2016). Investigation of crystal growth mechanism during selective laser melting and mechanical property characterization of 316L stainless steel parts. *Materials & Design, 100*, 291-299.

Wang, X. H. (2015). Synthesis and mechanical properties of Nb and Al substituted MoSi2. *Materials Research Innovations, 19*(4), S175-S180.

Wilkes, J. (2013). Additive manufacturing of ZrO2-Al2O3 ceramic components by selective laser melting. *Rapid Prototyping Journal*, 51-57.

Wohlers Report . (2019). *3D printing and additive maufacturing, State of the industry.* Wohlers Associates.

Yan, C. (2014). Advanced lightweight 316L stainless steel cellular lattice structures fabricated via selective laser melting. *Materials & Design, 55*, 533-541.

Yap, C. Y. (2017). Selective laser melting of nickel powder. *Rapid Prototyping Journal*, 750-757.

Yeh, C. L. (2007). Combustion synthesis of MoSi2 and MoSi2–Mo5Si3 composites. *Journal of alloys and compounds, 438*(1-2), 165-170.

Yen, B. K. (1997). Reaction synthesis of refractory disilicides by mechanical alloying and shock reactive synthesis techniques. *Materials Science and Engineering: A, 239*, 515-521.

Yu, W. (2019). Influence of re-melting on surface roughness and porosity of AlSi10Mg parts fabricated by selective laser melting. *Journal of Alloys and Compounds, 792*, 574-581.

Zakeri, M. (2005). Synthesis of nanocrystalline MoSi2 by mechanical alloying. *Journal of alloys and compounds, 403*(1-2), 258-261.

Zhang, L. (2019). Key issues of MoSi2-UHTC ceramics for ultra high temperature heating element applications: Mechanical, electrical, oxidation and thermal shock behaviors. *Journal of Alloys and Compounds, 780*, 156-163.

Zhang, L. C. (2016). Selective laser melting of titanium alloys and titanium matrix composites for biomedical applications: a review. *Advanced Engineering Materials, 18*(4), 463-475.

Zhong, Y. (2016). Intragranular cellular segregation network structure strengthening 316L stainless steel prepared by selective laser melting. *Journal of Nuclear Materials, 470*, 170-178.

Zhou, R. (2019). Precipitation behavior of selective laser melted FeCoCrNiC0. 05 high entropy alloy. *Intermetallics, 106*, 20-25.

Zhou, X. (2015). Balling phenomena in selective laser melted tungsten. *Journal of Materials Processing Technology, 222*, 33-42.

Zocca, A. (2015). Additive manufacturing of ceramics: issues, potentialities, and opportunities. *Journal of the American Ceramic Society, 98*(7), 1983-2001.

Acknowledgements

I would like to express my huge gratitude to my supervisor Professor Irina Hussainova for her great support, guidance and encouragement, to my current and former co-supervisors Dr Sofiya Aydinyan and Dr Marina Aghayan for their leadership, scientific and life lessons.

I would like to thank the ‘‘Archimedes’’ foundation for supporting my research visit to Institute of Ceramics and Glass, Madrid, Spain and University of Waterloo, Ontario, Canada. I wish to convey my sincere gratitude to Professor Miguel-Angel Rodrigues and Professor Ehsan Toyserkani for accepting me as a visiting student, their tremendous support and supervision, as they played a crucial role for my career development.

I would like to express my gratitude for Professor Jakob Kübarsepp, Professor Fjodor Sergejev for their thorough review and valuable comments on my thesis.

I wish to sincerely thank my former supervisor Professor Suren Kharatyan for guiding me over my Bachelor’s and Master’s degrees, for all the knowledge he gave me, all support, trust and care.

I would like to thank my first teachers in additive manufacturing field Dr Lauri Kollo, Dr Marek Jõeleht and Dr Yaroslav Holovenko.

I would like to acknowledge the significant help from my dear friends and colleagues Roman Ivanov and Le Liu for all useful scientific discussions, help and freindship.

I would like to express my deep gratitude to my friend and former colleague Dr Der-Liang Yung for encouragment and support.

I would like to thank my dear friends Nikhil Kamboj, Mansureh Rezapourian, Rahul Kumar, Ramin Rahmani, Janis Baronins, Rocio Rojas, Ali Saffar and whole my group for their friendship, positive vibes and scientific help.

I want to thank Dr Maksim Antonov, Dr Olga Volobujeva, Mr Rainer Traksmaa, Mr Mart Viljus, Laivi Väljaots and Hans Vallner for all the support they showed me during these 4 years of studies.

This research was funded by Tallinn University of Technology scholaraship, the Estonian Minsistry of Higher Education and Research under IUT19-29, PSG220 and PRG643 projects.

And my huge gratitude to my family and friends, that despite the distance between us, they cared, supported and believed in me.

Abstract
$MoSi_2$-based composites by selective laser melting

Molybdenum disilicide ($MoSi_2$) is a promising refractory material widely used for high temperature structural applications ranging from heating elements for combustion furnaces to turbine components for jet engines. However, some limitations, such as: severe oxidation of $MoSi_2$ in intermediate temperatures and low fracture toughness at room temperature are narrowing the application of $MoSi_2$. There are two approaches to improve the quality of $MoSi_2$ based materials: reinforcing $MoSi_2$ with thermodynamically compatible compounds (WSi_2, Mo_5Si_3, TiC, SiC, Si_3N_4, etc.), and alloying with metals or alloys (Nb, Al, Cr, Ti, Ta, W).

In this work Si_3N_4 was chosen as a reinforcing additive and aluminium as an alloying additive. The addition of Si_3N_4 is believed to improve the high thermal shock resistance, fracture toughness and high temperature creep strength. The addition of Al results on enhancement of ductility and oxidation resistance of $MoSi_2$-based materials by forming molybdenum aluminosilicide ($Mo(Si_{1-x},Al_x)_2$).

Self-propagating high-temperature synthesis (SHS) technique was used for $MoSi_2$ and $MoSi_2$-Si powders preparation as energy and time efficient process, allowing the control of size and shape of synthesized powders and ensuring high purity of the product. Commercially available (CA) powders (AlSi10Mg, Mo, Si) and SHS synthesized products were used for powder feedstock preparation by conventional mixing/milling techniques.

Selective laser melting (SLM) devices with different maximum laser power (Realizer SLM50 at 120 Watts and Renishaw AM400 at 400 Watts) were used for samples manufacturing. High dimensional accuracy, design freedom, ability of in-situ phase formation (reactive sintering) and single step process are the primary motivating attributes for SLM technique in the present research.

Goals of the present study are production of $MoSi_2$-Si_3N_4 ceramic lattices; preparation of $Mo(Si_{1-x},Al_x)_2$ based composite bulks by SLM along with parametric study and process optimization.

For the first time the approach of $MoSi_2$-Si_3N_4 lattice preparation by SLM of SHS prepared $MoSi_2$-Si composite powders and subsequent nitridation was successfully accomplished. $MoSi_2$-Si_3N_4 lattices with definite porosity, strut and pore size in close correspondence with CAD model were successfully fabricated.

For the first time an in-situ SLM processing (reactive sintering) of the $Mo(Si_{1-x},Al_x)_2$-based composite bulks were performed by two routines. The first routine represents the SLM consolidation of the mixture of three CA powders: 44.2 wt.% Mo + 25.8 wt.% Si + 30 wt.% AlSi10Mg (Mo+2Si+30 wt.% AlSi10Mg), and the second routine proposes the SLM consolidation of SHS prepared $MoSi_2$ mixed with 30 wt.% commercial AlSi10Mg powder.

$Mo(Si_{1-x},Al_x)_2$-based composite bulks (x=0.33 mol) prepared by the first routine are composed of fine columnar dendrites and possess up to 99% relative density; 496 HV1 and 498 HV5 hardness and moderate 8.4-11.1 µm side surface roughness (Sa) at applied 100 W laser power and 300-500 $mm \cdot s^{-1}$ scanning speed range.

$Mo(Si_{1-x},Al_x)_2$-based composite bulks (x=0.33 mol) prepared by the second routine consist of cellular and columnar dendrites; possess 6.5-10.3 µm top and 10.5-13.2 µm side surface roughness; up to 99.8% relative density; up to 570 HV1 and 540 HV5 hardness along with remarkable chemical and microstructural homogeneity at optimized

parameters of 150-200 W and 400-500 mm·s^{-1} scan speed, as well as 250 W laser power and 700 mm·s^{-1} scan speed.

Conclusively, the approach suggested for $MoSi_2$-Si_3N_4 lattice preparation was found as an effective way to reach the target phase composition and can be applied for production of complex shaped parts.

Characterization of $Mo(Si_{1-x},Al_x)_2$-based composite bulks, produced at optimized parameters of two different routines, reveals the phase composition, density and surface roughness to be suitable for applications, where high oxidation resistance at elevated temperatures is required. The second routine can be proposed as preferable, as it allows to apply external heat (laser power) in a more controllable manner, considering the weak exothermic reaction between $MoSi_2$ and aluminium compared to a high exothermicity of Mo-Si-Al reaction occurring in the first routine.

Keywords: self-propagating high-temperature synthesis, additive manufacturing, selective laser melting, molybdenum disilicide, molybdenum aluminosilicide, surface roughness, CT scanning, hardness

Lühikokkuvõte
Selektiivse lasersulatuse teel valmistatud $MoSi_2$ baasil komposiidid

Molübdeendisitsiid ($MoSi_2$) on paljutõotav kõrgtemperatuurne materjal, mida kasutatakse struktuurse materjalina laialdaselt kõrgete temperatuuridega rakendustes, alates põletusahjude kütteelementidest kuni reaktiivmootorite turbiinikomponentideni. Tugev oksüdeerumine juba keskmistel temperatuuridel ning madal purunemissitkus toatemperatuuril on peamised asjaolud mis kitsendavad $MoSi_2$ rakendusi. $MoSi_2$-põhiste materjalide kvaliteedi parandamiseks on kaks lähenemisviisi: $MoSi_2$ tugevdamine termodünaamiliselt ühilduvate ühenditega (WSi_2, Mo_5Si_3, TiC, SiC, Si_3N_4 jne) ning legeerimine metallide või metallisulamitega (Nb, Al, Cr, Ti, Ta, W).

Käesolevas töös valiti tugevdavaks lisandiks Si_3N_4 ning legeerivaks lisandiks alumiinium. Arvatakse, et Si_3N_4 lisamine parandab termolöögikindlust, purunemissitkust ja kõrgtemperatuurset roomekindlust. Alumiiniumi lisamine tõstab $MoSi_2$-põhiste materjalide plastseid omadusi ja vähendab kõrgtemperatuurset oksüdeerumist tänu molübdeenalumiinisilitsiidi ($Mo(Si_{1-x},Al_x)_2$) moodustumisele.

$MoSi_2$ ja $MoSi_2$-Si pulbrite valmistamisel kasutati kõrgtemperatuurse iselevisünteesi (SHS) meetodit kui energiat ja valmistusaega säästvat protsessi, mis võimaldab kontrollida sünteesitud pulbriosakeste suurust ja kuju ning tagab toote kõrge puhtuse. Kaubanduslikult kättesaadavatest pulbritest (AlSi10Mg, Mo, Si) ja SHS-i teel sünteesitud toodetest valmistati pulbrisegud tavapäraste segamis- ning jahvatamistehnikate abil.

Proovide valmistamiseks kasutati erineva maksimaalse laserivõimsusega selektiivse lasersulatuse (SLM) seadmeid (Realizer SLM50 120 W juures ja Renishaw AM400 400 W juures). Kõrge mõõtmete täpsus, kujundusvabadus, in-situ faaside moodustumine (reaktiivne paagutamine) ja üheastmeline protsess on käesolevas uurimustöös peamised motiveerivad tegurid SLM tehnoloogia valimiseks.

Käesoleva uuringu eesmärkideks on $MoSi_2$-Si_3N_4 keraamiliste võrestruktuuride tootmine; $Mo(Si_{1-x}Al_x)_2$ komposiittahkiste valmistamine läbi SLM protsessi optimeerimise ning parameetrilise uuringu.

Esmakordselt õnnestus käesolevas töös $MoSi_2$-Si_3N_4 võrestruktuuride valmistamine kasutades SLM meetodit sellele järgneva nitreerimisega, SHS-i teel valmistatud $MoSi_2$-Si komposiitpulbritest. Edukalt valmistati 3D mudeliga vastavuses olevad kindlaksmääratud poorsuse, varraste ja poorisuurusega $MoSi_2$-Si_3N_4 võrestruktuurid.

Esimest korda valmistati $Mo(Si_{1-x},Al_x)_2$ komponendid protsessi in-situ SLM teel (reaktiivpaagutamine) läbi kahe erineva meetodi. Esimese protseduuri puhul valiti 44.2 massiprotsenti Mo+25.8 massiprotsenti Si + 30 massiprotsenti AlSi10Mg segu mis konsolideeriti SLM teel. Teine meetod kasutab 30 massiproti SHS teel valmistatud $MoSi_2$ ning kaubandusliku AlSi10Mg pulbri SLM tehnoloogiaga konsolideerimist.

Esimese protseduuri järgi valmistatud $Mo(Si_{1-x},Al_x)_2$ tahkiste (x=0.33 mol) mikrostruktuur koosneb peenetest dendriitidest. Komposiitide suhteline tihedus on kuni 99%; kõvadus 496 HV1 ja 498 HV5 ning pinnakaredus 8.4–11.1 µm (Ra), 100 W laservõimsuse ja 300–500 $mm \cdot s^{-1}$ skaneerimiskiiruse juures.

Teise meetodi järgi valmistatud $Mo(Si_{1-x},Al_x)_2$ komposiitide (x = 0.33 mol) mikrostruktuur koosneb võre- ja sammasdendriitidest. Nendepinnakaredus on pealispinnal 6.5-10.3 µm ja külgpinnal 10.5-13.2 µm; suhteline tihedus kuni 99.8%; kõvdus kuni 570 HV1 ja 540 HV5 koos märkimisväärse keemilise ja mikrostruktuuri

homogeensusega. Optimeeritud parameetrid on 150-200 W juures ja 400-500 $mm \cdot s^{-1}$ skaneerimiskiirusel, samuti 250 W laservõimsuse ja 700 $mm \cdot s^{-1}$ skaneerimisel kiiruse juures.

Kokkuvõtteks leiti, et $MoSi_2$-Si_3N_4 võrestruktuuride valmistamiseks pakutud lähenemisviis võimaldab saavutada soovitud faasilise koostise ja seda saab rakendada keerukate detailide tootmiseks.

Kahe erineva meetodiga valmistatud $Mo(Si_{1-x},Al_x)_2$ faasilise koostise, tiheduse ja pinnakareduse näitajad kinnitavad, et need materjalid sobivad rakendusteks kus on vajalik kõrge oksüdatsioonikindlus kõrgendatud temperatuuridel. Eelistatumaks võib pakkuda teist protseduuri, kuna see võimaldab rakendada sisendenergiat (laseri võimsust) paremini kontrollitaval viisil, arvestades $MoSi_2$ ja alumiiniumi madalamat eksotermilist reaktsiooni, võrreldes esimese protseduuri puhul toimuva kõrge eksotermilisusega Mo-Si-Al reaktsiooni käigus.

Märksõnad: kõrgtemperatuurne iselevisüntees, kihtlisandustehnoloogiad, selektiivne lasersulatus, molübdeendisilitsiid, molübdeenalumiinisilitsiid, pinnakaredus, kompuutertomograafia, kõvadus

Appendix

Paper I

Minasyan, T., Aghayan, M., Liu, L., Aydinyan, S., Kollo, L., Hussainova, I., & Rodríguez, M. A. (2018). Combustion synthesis of $MoSi_2$ based composite and selective laser sintering thereof. *Journal of the European Ceramic Society*, 38(11), 3814-3821.

Journal of the European Ceramic Society 38 (2018) 3814–3821

Contents lists available at ScienceDirect

Journal of the European Ceramic Society

journal homepage: www.elsevier.com/locate/jeurceramsoc

Original Article

Combustion synthesis of $MoSi_2$ based composite and selective laser sintering thereof

Tatevik Minasyan[a], Marina Aghayan[a,b,*], Le Liu[a], Sofiya Aydinyan[a], Lauri Kollo[a,b], Irina Hussainova[a,b,c], Miguel A. Rodríguez[b,d]

[a] Tallinn University of Technology, Ehitajate tee 5, Tallinn, 19086, Estonia
[b] FACT-Industries OÜ, Õismae tee 124, Tallinn, 13513, Estonia
[c] ITMO University, Kronverkskiy 49, St. Petersburg, 197101, Russia
[d] Instituto de Cerámica y Vidrio, CSIC, C/Kelsen 5, 28049 Madrid, Spain

ARTICLE INFO

Keywords:
Additive manufacturing
Selective laser sintering
Combustion synthesis
Ceramic composites
$MoSi_2$

ABSTRACT

Additive manufacturing is gaining increasing attention as it provides cost-effective and waste-less production of materials with multi-axis geometries. Selective laser sintering of ceramics is very challenging in terms of poor sinterability caused by low thermal shock resistance and insufficient electron conductivity blocking absorption of laser beam energy.

Here, we present a novel strategy for manufacturing dense, hierarchically structured ceramics, particularly, $MoSi_2$-based composites by selective laser sintering. $MoSi_2$-Si composite powders were prepared by combustion synthesis technique, where the ceramic grains were covered with different amount of Si. $MoSi_2$-Si powder was consolidated by selective laser sintering reaching 92% of density. The hardness of the manufactured samples varied with the amount of Si and applied laser current from 7.7–11.4 GPa. The maximum value of the compressive strength was determined to be 636 MPa. The manufactured $MoSi_2$-Si was subjected to nitridation, which resulted in the growth of Si_3N_4 fibres on the surface and pores of the samples.

1. Introduction

The progress of the enabling technologies provides the best platform for cooperation across industry and science sectors and generates economic growth. Since approbation of the first commercial 3D printer in the 1980s, a manufacturing process shifts to a digital model in which the entire industrial sector evolves to become more local and entrepreneurial, changing towards creativity and design thinking.

The traditional means of fabrication for complex-shaped parts usually involve a series of steps resulting in huge material waste and a high labour cost along with limitations on design complexity. Despite the fact that the conventional net-shaping processes, such as ceramic injection moulding, slip casting, etc., enable large-scale production of complex-shaped components, they are not economically competitive in the case of small-scale production because of the need in costly tailor-made mould.

Being cost-effective and in some cases irreplaceable technique, 3D printing or additive manufacturing (AM) expanded the range of applications in modern industries, such as automotive, aerospace, defence, electronics and robotics sectors [1–3]. It allows minimization of manufacturing time, generated waste of materials, and energy consumed. Moreover, with the help of AM technique, the near-net shape structures can provide unprecedented control over an internal porosity of compounds, that is highly demanded by medicine, particularly for the preparation of body prostheses, dental and tissue engineering scaffolds [4,5].

Fabrication of ceramic parts by additive manufacturing is a challenging task, because of the high melting temperature, low thermal shock resistance, high thermal stability, high viscosity of the molten ceramic, etc. Several studies have reported fabrication of the fully dense ceramic parts with tailored mechanical properties; for example, the high density of structural ceramics (Al_2O_3, density > 97%; SiC, density > 95%, Si_3N_4 density > 99%) were achieved by robocasting [6]. However, the parts suffer from an anisotropic strength. Technology of fused deposition of ceramics (FDC) was successfully applied to processing WC/Co, Al_2O_3, and Si_3N_4 [7]. However, the huge amount of the required binder phase (50–60 vol.%) resulted in an anisotropic shrinkage and presence of defects deteriorating the mechanical properties. The obtained high density of Si_3N_4 part (96%) provides a comparable bending strength to those of extruded and iso-pressed samples

* Corresponding author at: Tallinn University of Technology, Ehitajate tee 5, Tallinn, 19086, Estonia.
E-mail address: marina.aghayan@ttu.ee (M. Aghayan).

https://doi.org/10.1016/j.jeurceramsoc.2018.04.043
Received 17 February 2018; Received in revised form 18 April 2018; Accepted 19 April 2018
Available online 22 April 2018

[7]. Viscous suspensions of ceramic particles (60 vol.%) were also prepared to fabricate Al_2O_3 based materials by Ceramic On-Demand Extrusion (CODE) resulting in production of the high-density component after drying and high-temperature sintering [8]. It was suggested that the remained 1.5% porosity was caused by the bubbles in the paste, which can be eliminated via optimizing the drying process. One of the most commonly employed 3D printing techniques is stereolithography, which provides a good precision feature and a smooth surface of the products. Stereolithography enables production of the nearly full density and, therefore, mechanically reliable ceramic parts (e.g. zirconia [9], zirconia-toughened alumina [10], Si_3N_4 [11,12]) for industrial and biomedical applications. However, the stereolithography exhibits up to 60% shrinkage and geometric changes, which makes the technology uncertain.

Fabrication of ceramic parts by the selective laser sintering represents a fascinating challenge. Ceramics usually suffer from high level of porosity, poor interlayer adhesion, and low mechanical properties [13,14]. In [15], the potential of the selective laser sintering for consolidation of Al_2O_3-ZrO_2 based materials with almost 100% density and flexural strength above 500 MPa was highlighted exploiting the complete melting of the powder and no any post-treatment. Development of defects was overcame with the help of high temperature preheating up to1600 ˚C [15].

Several factors should be taken into account for successful launch of the SLS. Among them there are:

(i) *State of the powder during sintering.* By traditional techniques, densification of ceramics are usually relatively time-consuming process. In the case of SLS, the high-intensity laser heats the target over a microsize sport for a short period of time preventing diffusion. For a liquid phase sintering, a binder material (e.g. metal, polymer or glass) of comparatively low melting point is required to bind the ceramic particles.

(ii) *Powder flowability* is a key parameter greatly influencing powder bed density, which affects the sintered part quality including density, roughness, etc. Powder particle shape and size as well as particle size distribution play an important role in sintering kinetics and powder bed formation. For example, the spherical particles of the narrow size distribution have better flowability as compared to the angularly shaped powders. The density of the powders is another very important characteristic that deserves attention when choosing the powder for SLS.

(iii) *Laser beam-powder interaction.* The SLS laser should be carefully chosen taking into account the material to be sintered. For instance, the CO_2 laser with a wavelength of 10.6 μm is well absorbed by polymer powders and oxide ceramics; while Nd:YAG laser with wavelength of 1.06 μm is well absorbed by metals and carbides [16]. The materials absorbing at a short wavelength have a higher processing window when Nd:YAG is applied [16]. However, the CO_2 laser provides wider processing window, including energy density, particle size ranges for a large number of materials (e.g. HAPEX®) [17].

(iv) *Composition.* In general, laser sintering of a single-component powder is a complicated process due to the narrow processing window [18]. The single-component powder has to be densified at the well-established processing parameters (e.g. laser power, scanning speed, scan line spacing, temperature of the powder bed, etc.) usually exploiting complete melting of the powder. Full melting may cause a number of undesired effects, such as merging of droplets and minimising the surface energy. Formed liquid zone and temperature gradient can generate Marragoni convection, namely, mass flow from regions with a low surface tension to regions with a high surface tension. Marragoni flow may cause a tendency to balling of alloys containing a sufficiently high content of surface active elements during SLS [19].

(v) *Impurities.* Even the traces of oxygen influence dramatically the sintering of the powder. For instance, Fe containing 0.1 wt% oxygen has a much higher tendency to balling than Fe containing 0.02 wt% oxygen due to a higher surface tension gradient. Therefore, the addition of small amount of carbon as a deoxidizing agent to iron decreases the surface tension gradient and allows to obtain smoother layer [19]. The existence of impurities in the chamber (e.g. oxygen) usually changes the optical properties of the powder and hampers sintering [18].

(vi) *Scanning strategy.* Laser power, scanning speed, hatch spacing, and layer thickness have a high impact on the densification, microstructural features, and mechanical properties of the final part. The scanning parameters vary from powder to powder and should be optimized as a complex and evaluate their combined effect. For instance, the low scan speed of Fe powders prevents balling and leads to the formation of smooth layer [19]. A similar tendency is observed in the case of NiAl alloy [20]. However, the slow scan speeds result in pores development from gases trapped within the melt pool or evolved from the AlSi10Mg powder during consolidation [21]. In addition, evaporation of the molten material can harm a laser window and disrupt the delivery of the laser power. The evaporation of the material can be prevented by decreasing the laser power. To build a part with the full density and desired properties, complex optimization of all parameters (laser power, scanning speed, hatch spacing, and layer thickness) is necessary to successfully build the near full-density parts.

In this work, we report a novel strategy to fabricate ceramic parts, particularly $MoSi_2/Si_3N_4$ composite by the selective laser sintering. The strategy includes synthesis of ceramic/metalloid (particularly, $MoSi_2$/Si) composite powder enabling melting of the metalloid component and sintering by SLS technique. After consolidation the unique ceramic/metalloid composite is subjected to functionalizion (particularly, nitridation) converting the part into ceramic/ceramic composite (particularly, $MoSi_2/Si_3N_4$). Fig. 1 represents the scheme of the proposed approach. The effect of the amount of silicon and SLS conditions (laser current, point distance, exposure time) on the sinterability and density

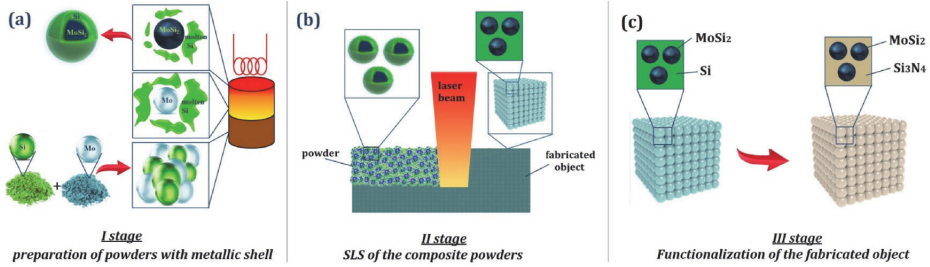

Fig. 1. The schematic representation of the novel strategy for fabrication of ceramic composites by selective laser sintering.

Table 1
The composition of elemental powder mixture and combustion product.

Sample	Combustion product	Calculated amount of free Si (wt.%) after combustion	Amount of free Si (wt.%) after combustion based on XRD*
nSi = 2.2	$MoSi_2$-0.2Si	3.6	3.0
nSi = 2.4	$MoSi_2$-0.4Si	6.9	7.2
nSi = 2.6	$MoSi_2$-0.6Si	10.0	10.1
nSi = 2.8	$MoSi_2$-0.8Si	12.8	13.0
nSi = 3.0	$MoSi_2$-Si	15.5	15.8

of $MoSi_2$/Si was thoroughly studied. The materials were mechanically tested.

2. Experimental

2.1. $MoSi_2$-Si powder preparation

The starting powder materials were: > 99.9% purity Mo (Aldrich) with a particle size of 1–5 μm and specific surface area (SSA) of 1.27 m^2/g; and > 99% purity Si (Silgrain-Elkem) with a mean particle size of 4 μm and SSA of 3.37 m^2/g. The elemental powder mixtures (Mo-nSi) containing stoichiometric ratios of Mo:Si = 1:2.2, 1:2.4, 1:2.6, 1:2.8, 1:3.0. (Table 1) were mixed in a ceramic mortar for 15 min and die-pressed at room temperature under a uniaxial pressure of 4 MPa. Cylindrical samples with a height of 25–30 mm and a diameter of 40 mm were prepared and attached to the cylindrical Ti-C samples (molar ratio of Ti:C = 1:1) with a height of 2–3 mm and a diameter of 40 mm. An electrically heated tungsten coil ignited the Ti-C mixture, which itself ignited Mo-nSi (where *n* is the molar ratio of Si) targeted system. The combusted samples were crushed into a powder and sieved to < 45 μm in size.

Combustion temperature was measured by IMPAC pyrometer (400–2200 °C range). After the combustion reaction, the reacted samples were crushed into a powder, sieved and prepared for sintering.

2.2. SLS processing

Sintering of the powder was performed by SLS technique using Metal 3D printer (ReaLizer GmbH SLM-50, Germany) equipped with a YAG: Nd^{3+} laser with a maximum output power of 120 W, laser spot size of 15–100 μm and computer-controlled laser beam scan velocity up to 1000 mm/s.

During the sintering, the chamber was sealed with a high purity nitrogen (99.999 vol.%) to avoid oxidation and degradation of the powder. The focused laser beam (IPQ Laser GmbH, YLM-120-AC, 120 W, YAG: Nd^{3+} with 1.06 μm wavelength) was then directed onto the powder bed to form the pattern according to CAD design. The laser beam is deflected by galvano mirrors, which control the movement of the laser source over the surface of the powder bed. The powder was spread by a wiper over the surface of 75 mm diameter steel cylindrical platform. In each layer, the laser beam followed a prescribed scanning path. Solidification was obtained by fusing or sintering selected areas of the successive powder layers using a thermal energy supplied through a laser beam. When a layer is scanned, the build cylinder moves down one step-typically 25 μm, wiper spreads next layer of powder to build the bed. The process is repeated until manufacturing of the designed part is complete. Low scanning speed (80 mm/s) with a scanning line space of 60 μs was used keeping exposure time and point distance fixed to 125 μs and 10 μm, respectively. The laser current was altered from 900–1300 mA. As a result, the laser energy density was changed from 180–260 J/mm^3.

Samples with a cubic form with a length of 5 mm were prepared from $MoSi_2$-Si powder mixture. SLS process parameters are given in Table 2.

Table 2
Influence of the SLS process parameters on the density of sintered samples, where Point distance is 10 μm, Exposure time - 125 μs.

Sample	Laser current (mA)	Density (g/cm^3)	Relative density (%)	Hardness (GPa)
nSi = 2.2	900	3.4	57	7.7
nSi = 2.2	1100	4.2	72	8.4
nSi = 2.2	1300	5.4	92	10.5
nSi = 2.4	900	4.4	79	8.0
nSi = 2.4	1100	4.5	81	10.0
nSi = 2.4	1300	5.0	89	11.4
nSi = 2.6	900	4.1	77	8.5
nSi = 2.6	1100	4.4	82	8.8
nSi = 2.6	1300	4.8	90	10.3
nSi = 2.8	900	3.7	72	9.8
nSi = 2.8	1100	4.3	83	10.8
nSi = 2.8	1300	4.5	88	10.9

2.3. Nitridation of $MoSi_2$-Si samples

The Selective laser sintered $MoSi_2$/Si specimens were placed in a graphite boat and heated in a furnace (RdWEBB, USA) to 1350 °C at 10 °C/min heating rate and held for 3 h in nitrogen (purity 99.999 vol. %) gas flow of 200 ml/min.

A schematic illustration of the process of $MoSi_2/Si_3N_4$ parts fabrication is shown in Fig. 1.

2.4. Characterization

Phase composition was analyzed by X-ray diffraction (XRD; D5005, Bruker, USA) using CuKα1 radiation (λ = 1.5406 Å) with a step of 0.02° (2θ) and a scanning rate of 4° min^{-1}. Morphologies and microstructures of the samples were observed by high-resolution scanning electron microscope (HR-SEM Zeiss Merlin) at an accelerating voltage of 2 kV. HR-SEM was equipped with an In-Lens SE detector for topographic imaging and In-Lens energy selective backscattered detector for compositional contrast. Energy-dispersive X-ray spectroscopy (Bruker EDX-XFlash6/30 detector) was carried out at an accelerating voltage of 10 kV. The concentrations of elements were calculated by using PB-ZAF standardless mode.

Compressive strength tests were performed to evaluate the structural integrity of the samples. The cylindrical samples with 10 mm (± 0.1 mm) of diameter and 5 mm (± 0.1 mm) of height were loaded at a crosshead speed of 0.5 mm/min (the speed calculated based on ASTM E9/09 [22]). Microhardness was measured using Vicker's microhardness tester (Indentec 5030 SKV) at a load of 1 kg and an indentation time of 10 s.

3. Results and discussion

3.1. Combustion laws in the Mo - nSi system

Thermodynamically, the formation of $MoSi_2$ through the reaction of molybdenum with a stoichiometric amount of silicon is characterized by a moderate exothermicity (ΔH = 130 kJ/mol) [23] so that the adiabatic temperature T_{ad} attains a value of 1650 °C. However, increasing the amount of silicon, which has a thermal dilution effect, leads to the fluent decrease of both the combustion and adiabatic temperatures (Fig. 2a). These values are lower than the empirical limit enunciated in [24] (1587 °C); nevertheless, these values are not exact, and only approximately show if the system is enough exothermic to reach the activation energy of the reaction. Another aspect is that the raw materials have a higher, than the ambient, initial temperature due to the heat generation from the combustion of Ti-C mixture (Tad is a much higher for Ti-C system). Thus, the real temperature of the reaction is higher than thermodynamically calculated. When the n_{Si} = 3.0, the

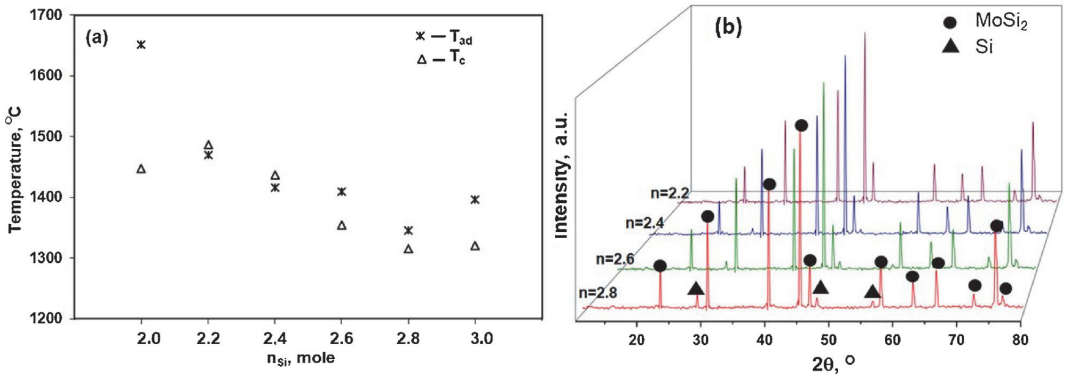

Fig. 2. The effect of silicon amount (n_{Si}) on the combustion and adiabatic temperatures (a) and XRD patterns of the combustion products (b).

process no longer takes place in a self-sustained regime, therefore the sample was pre-heated in a furnace at 400 °C.

The X-ray diffraction (XRD) data of the combustion products, Fig. 2(b), show that $MoSi_2$ phase was formed along with Si during the combustion reaction in the Mo–nSi reactive mixture. The relative intensity of Si diffraction peaks increases with increasing Si content in the reaction mixture. The intensity ratios of $MoSi_2$/Si peaks were calculated by Rietveld refinement of XRD data, which showed intensity ratios of $MoSi_2$/Si correspond to the theoretical ones when $n_{Si} \geq 2.4$. In the silicon lean sample ($n_{Si} = 2.2$), the amount of silicon is less than theoretical, caused by the higher combustion temperature developed during the process resulting in evaporation of Si. Kharatyan et al. [23] reported that the combustion of Mo-2Si mixture began with a solid-solid exothermic reaction leading to the formation of $MoSi_2$. This process was followed by the melting of silicon and the solid-liquid reaction between Mo and Si. Both solid-solid and solid-liquid reactions resulted in $MoSi_2$ formation.

Fig. 3 shows the SEM images of combusted Mo-nSi mixture after grinding. Based on the SEM observations, it can be asserted that the particle size of the obtained $MoSi_2$/Si composite powder increases slightly with increasing the amount of Si. An average particle size of 4 μm was measured for $n_{Si} = 2.2$. However, the particles become bigger in size and inhomogeneous in size distribution with increasing the amount of Si. In the case of $n_{Si} = 2.8$, particles agglomerates with up to 20 μm in size can be observed. As it was reported in [23], upon Si melting, some amount of Mo dissolves in Si melt where $MoSi_2$ grains precipitate. Partially $MoSi_2$ forms and grows by a reactive diffusion, as well. This mechanism explains the formation of relatively small $MoSi_2$ particles, which are not bigger than the starting Mo particles. SEM and EDS mapping result show each particle consists of $MoSi_2$ grains with < 4 μm in size bonded with Si layer for $n_{Si} = 2.2$. The silicon fuse covers homogeneously $MoSi_2$ grains (Sup. Fig. 1). Although increasing the amount of silicon leads to the formation of bigger agglomerates, the higher resolution SEM and EDS mappings show that the agglomerates consist of small$MoSi_2$ grains bonded to each other with Si fuse (Sup. Fig. 2). Such morphology manifested or evinced the solid-liquid interaction between Mo and Si. The decrease in grain size of $MoSi_2$ can be caused by a lower temperature generated during the combustion (Fig. 2(a)) and a lower concentration of Mo in Mo-Si mixture.

3.2. Selective laser sintering of $MoSi_2$ - Si composites

The measured apparent densities of the composites are listed in Table 2. The densities vary from 57 to 92%. The geometrical density of the sintered samples strongly depends on the laser current. The composite parts show the highest values when a higher laser current is applied, which is caused by providing a lower viscosity of silicon, thus, spreading through the $MoSi_2$ particles. At the low laser current, the amount of silicon critically influences the density of the parts. However, the further increase of the laser current (1300 mA) does not cause change of density. This can be explained by the decrease of viscosity of Si during heating facilitating its spreading between the particles and binding them in the case of the low amount of Si. While at the high amount of Si, it should be "softened enough" to bond the neighbouring particle.

The SEM analysis shows that when the silicon amount in $MoSi_2$-Si composite is ≤0.4 (6.9 wt.%), the cracks over the parts are generated (Sup. Fig. 3). This is caused by the low thermal shock resistance of $MoSi_2$. With increase in the amount of Si, the thermal stresses decreases resulting crackless parts.

Fig. 4 shows the SEM images of $MoSi_2$-0.6-0.8Si composites sintered by the laser with different currents. The sample of a higher content of silicon ($MoSi_2$-0.8Si) has a smoother surface in comparison to the silicon lean samples; however, the silicon-rich samples contain more cracks.

Fig. 5 shows the SEM and EDS mapping of the selective laser sintered $MoSi_2$-0.6Si (10 wt.% Si) part. The $MoSi_2$ particles with 2–4 μm in size are well dispersed and interconnected by Si layer < 0.3 μm.

XRD analysis of the sintered samples showed only the presence of $MoSi_2$ and Si, thus new phases were not obtained due to the laser treatment.

3.3. Mechanical properties of fabricated $MoSi_2$ - Si composites parts

Table 2 demonstrates that the hardness values of the selective laser sintered parts depend on the laser current and amount of Si. The increase of the laser current positively influences the hardness. This is connected with a higher density of the parts using a higher laser current. The hardness differs strongly with changing the amount of Si in $MoSi_2$-Si composites. When the laser current is 900 mA, the hardness of the specimens increases increasing the amount of Silicon. This effect is not noticeable at higher laser currents. The authors propose that the lower laser current does not supply enough energy to melt and/or increase the viscosity of silicon. So, the sintering of the powders containing small amount of silicon, where the silicon does not homogeneously cover ceramic core leads to the formation of defects. The powders containing higher amount of silicon are more homogeneously covered with the binder phase, which facilitates the sintering, resulting the increase of the hardness of the consolidated samples. At higher laser current (1300 mA), the hardness increases from 10.5 GPa to 11.4 GPa increasing the amount of silicon from n = 2.2 to n = 2.4. However, the further increase of the amount of silicon leads to decrease of hardness to 10.3 GPa (n = 2.6) and 10.9 GPa (n = 2.6). At high laser current, silicon melts and distributes over the sample. When there is sufficient

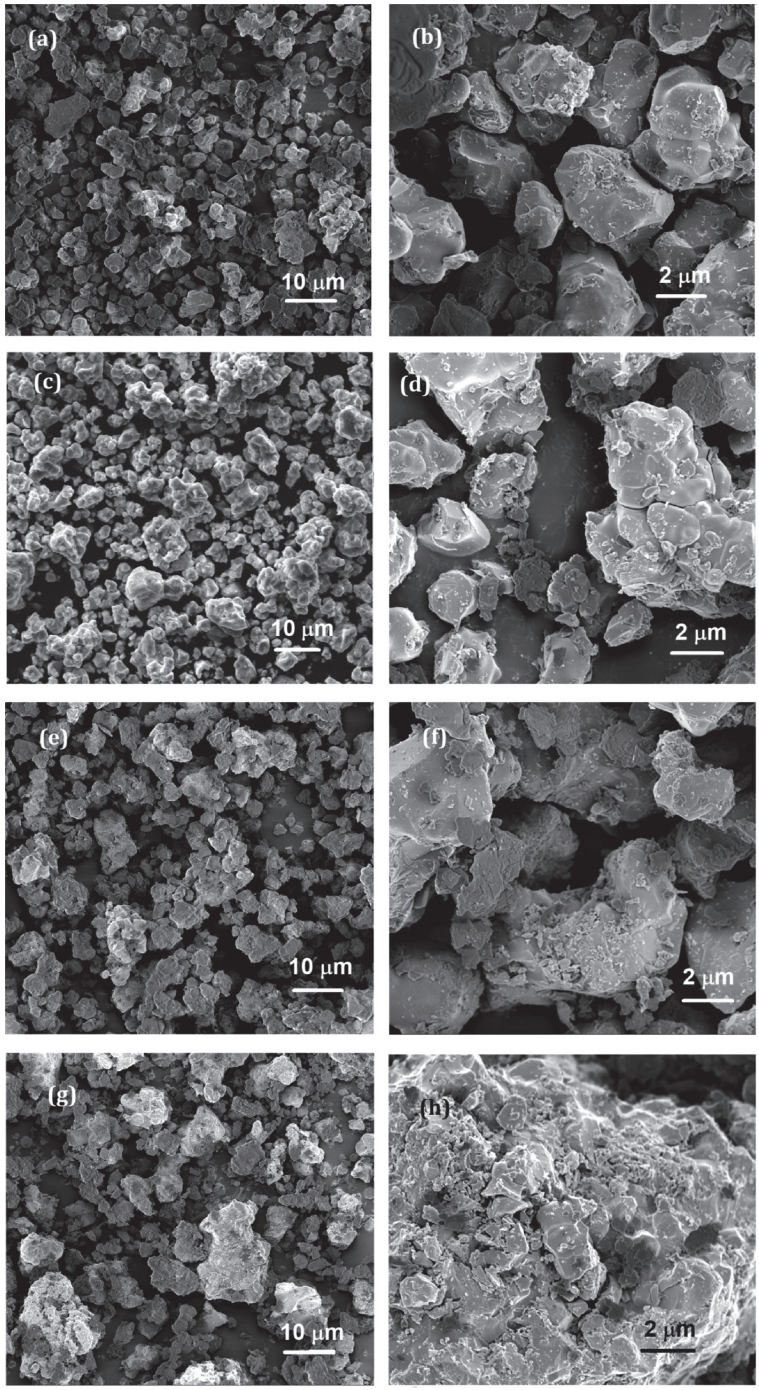

Fig. 3. Low and high magnification SEM images of combustion products of Mo + nSi mixtures: (a,b) n = 2.2; (c,d) 2.4; (e,f) 2.6; (g,h) 2.8.

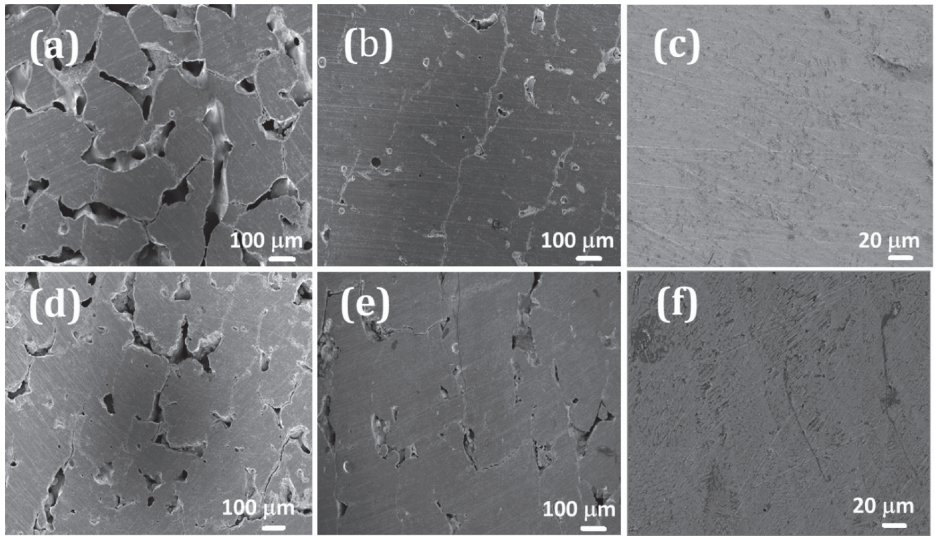

Fig. 4. Low and high magnification SEM images of selective laser sintered MoSi2-Si parts with different amount of Si and laser current correspondingly: (a)0.6; 900 mA; (b) 0.6; 1100 mA; (c) 0.6; 1100 mA; (d) 0.8; 900 mA; (e) 0.8; 1100 mA; (f) 0.8; 1100 mA.

amount of silicon to fill the space between the ceramic particles, the further increase in the silicon quantity does not affect the densification and formation of defects. Moreover, increasing the amount of silicon leads to the decrease of the concentration of the harder phase-MoSi2, resulting to the decrease of the hardness.

The highest hardness value result was recorded as 11.4 GPa for $MoSi_2$-0.4Si (or 6.86 wt.% of Si) at 1300 mA laser current. These hardness values are higher as compared to previously reported for $MoSi_2$-based ceramic composites consolidated by vacuum hot pressing, hot isostatic pressing [25].

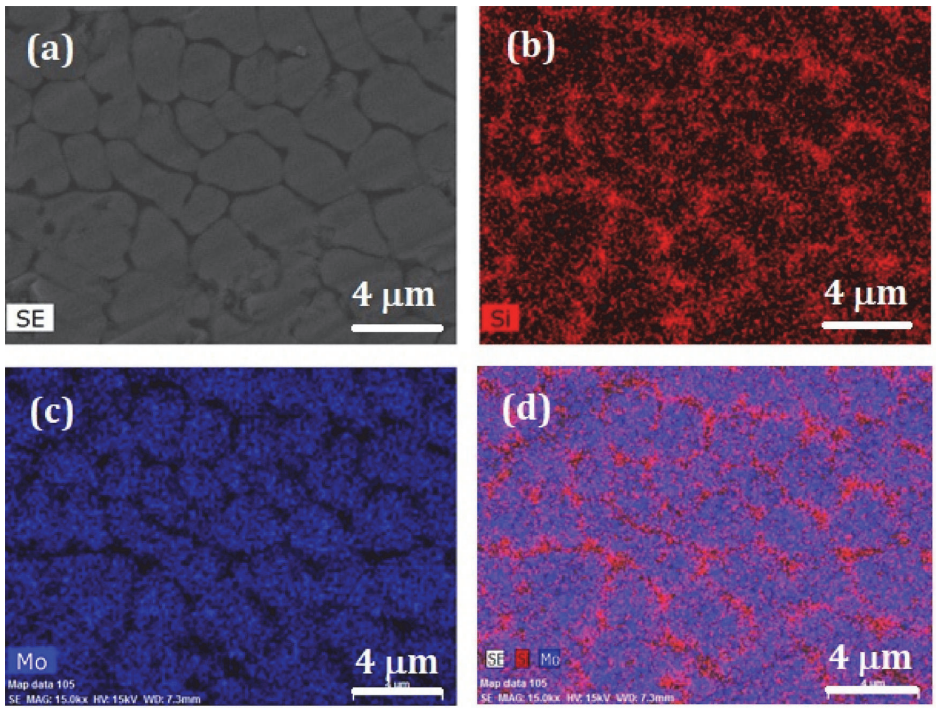

Fig. 5. SEM and EDS mapping analysis result of selective laser sintered MoSi2-0.6Si part at 1300 mA laser current: (a) SEM (backscattered electron) morphology, (b) Si map, (c) Mo map, (d) Mo and Si map.

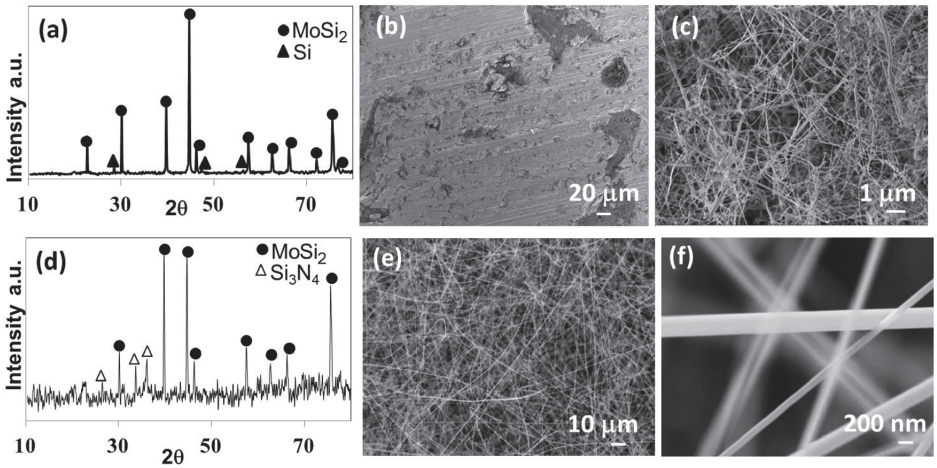

Fig. 6. XRD patterns (a, d) and SEM images of fracture (b, c) and surface(e, f) of selective laser sintered $MoSi_2$-0.6Si (1100 mA) sample after nitridation.

The consolidated $MoSi_2$-0.6Si product (diameter-10 mm; height-5 mm, laser current-1300 mA) was subjected to the compression test. During the test, when the load reached 50.0 kN, the product started to break. Based on the test results, the compressive strength was determined to be 636 MPa.

3.4. Nitridation of selective laser sintered $MoSi_2$-Si samples

Hereinafter, the selective laser sintered $MoSi_2$-0.6-0.8Si parts were applied for nitridation in a nitrogen environment at 1350 °C for 3 h. The parts are covered with white fibrous mass, while the centre remains grey. The XRD and SEM analysis show that the fibres are composed of Si_3N_4, which are grown on the surface and in the pores existed in the bulk (Fig. 6). There is less amount of fibres grown in the fracture surface and the fibres are shorter and thicker as compared to those grown on the outer surface of the sintered composites. The surface of the $MoSi_2$-0.6Si part is composed of $MoSi_2$, Si_3N_4 and a little amount of Si (Fig. 6(d)). However, the XRD analyses did not detect Si_3N_4 phase in the central part of the sample (Fig. 6(a)). The current investigations are directed to improve the nitridation of the printed silicon.

4. Conclusions

Combustion synthesis can be successfully used for the fabrication of MoSi2-Si composite powders, where a controllable amount of Si covers $MoSi_2$ grains promoting laser absorption, sintering and further possible functionalization into the desired ceramic.

For the first time, the $MoSi_2$-based composite containing < 13 wt.% of Si as a binding agent was consolidated by the selective laser sintering in a single stage. The produced parts of a high (92%) density were free of cracks and detectable structural defects. It was shown that the laser current and the amount of Si drastically influence the morphology, density and mechanical properties of the parts. The Vickers hardness and compressive strength of the sintered $MoSi_2$-Si parts reached up to 11.4 GPa and 636 MPa, correspondingly.

The nitridation of $MoSi_2$-Si results in the formation of fibrous Si_3N_4 on the surface of the samples, while nitridation of the bulk was not successful. Traces of Si_3N_4 fibres were determined in the pores generated during sintering.

Acknowledgements

The authors would like to thank the European Regional Fund under the project number 2014-2020.4.01.16-0183 (Smart Industry Centre). The authors are grateful to the JECS Trust for funding the visit of M. Aghayan to Instituto de Cerámica y Vidrio, CSIC (Contract No. 2017142) to implement research. This work was also supported by the Estonian Research Council underPUT1063 (I. Hussainova). T. Minasyan acknowledges the Archimedes foundation under the DoRa + scholarship program for partial funding the research. Authors would like to thank PhD O. Volobujeva, PhD M. Viljus and Mr R. Traksmaa for their help with SEM and XRD analysis.

Appendix A. Supplementary data

Supplementary material related to this article can be found, in the online version, at doi:https://doi.org/10.1016/j.jeurceramsoc.2018.04.043.

References

[1] J. O'Donnell, M. Kim, H.S. Yoon, A review on electromechanical devices fabricated by additive manufacturing, J. Manuf. Sci. Eng. 139 (1) (2017) 010801.
[2] L. Chong, S. Ramakrishna, S. Singh, A review of digital manufacturing-based hybrid additive manufacturing processes, Int. J. Adv. Manuf. Tech. (2017) 1–20.
[3] R. Liu, Z. Wang, T. Sparks, F. Liou, J. Newkirk, Aerospace Applications of Laser Additive Manufacturing, Laser Additive Manufacturing, Woodhead Publishing Series in Elect. and Optic. Mater., 2017, pp. 351–371.
[4] X. Wang, S. Xu, S. Zhou, W. Xu, M. Leary, P. Choong, Y.M. Xie, Topological design and additive manufacturing of porous metals for bone scaffolds and orthopaedic implants: a review, Biomaterials 83 (2016) 127–141.
[5] S. Singh, S. Ramakrishna, R. Singh, Material issues in additive manufacturing: a review, J. Manuf. Process. 25 (2017) 185–200.
[6] E. Feilden, E.G.T. Blanca, F. Giuliani, E. Saiz, L. Vandeperre, Robocasting of structural ceramic parts with hydrogel inks, J. Eur. Ceram. Soc. 36 (10) (2016) 2525–2533.
[7] M.K. Agarwala, A. Bandyopadhyay, R. Van Weeren, N.A. Langrana, A. Safari, S.C. Danforth, Fused deposition of ceramics (FDC) for structural silicon nitride components, Proc. of SFF Symposium, (1996), pp. 335–343.
[8] A. Ghazanfari, W. Li, M.C. Leu, G.E. Hilmas, A novel extrusion-based additive manufacturing process for ceramic parts, Proc. of SFF Symposium, (2016).
[9] H. Xing, B. Zou, S. Li, X. Fu, Study on surface quality, precision and mechanical properties of 3D printed ZrO2 ceramic components by laser scanning stereolithography, Ceram. Int. 43 (18) (2017) 16340–16347.
[10] H. Wu, W. Liu, R. He, Z. Wu, Q. Jiang, X. Song, S. Wu, Fabrication of dense zirconia-toughened alumina ceramics through a stereolithography-based additive manufacturing, Ceram. Int. 43 (1) (2017) 968–972.
[11] S. Kang, J. Stampfl, A.G. Cooper, F. Prinz, Application of the Mold SDM Process to the Fabrication of Ceramic Parts for a Micro Gas Turbine Engine, Technical Report, Rapid Prototyping Laboratory, Stanford University, Stanford, CA, 2000, pp. 1–6.
[12] M.H. Bocanegra-Bernal, B. Matovic, Dense and near-net-shape fabrication of Si3N4 ceramics, Mater. Sci. Eng. A 500 (1-2) (2009) 130–149.
[13] P. Bertrand, F. Bayle, C. Combe, P. Gœuriot, I. Smurov, Ceramic components

manufacturing by selective laser sintering, Appl. Surf. Sci. 254 (4) (2007) 989–992.
[14] I. Shishkovsky, I. Yadroitsev, P. Bertrand, I. Smurov, Alumina–zirconium ceramics synthesis by selective laser sintering/melting, Appl. Surf. Sci. 254 (4) (2007) 966–970.
[15] H. Yves-Christian, W. Jan, M. Wilhelm, W. Konrad, P. Reinhart, Net shaped high-performance oxide ceramic parts by selective laser melting, Phys. Procedia 5 (2010) 587–594.
[16] J.P. Kruth, X. Wang, T. Laoui, L. Froyen, Lasers and materials in selective laser sintering, Assembly Autom. 23 (4) (2003) 357–371.
[17] M.M. Savalani, L. Hao, R.A. Harris, Evaluation of CO2 and Nd: YAG lasers for the selective laser sintering of HAPEX®, Proc. Inst. Mech. Eng. B 220 (2) (2006) 171–182.
[18] N.K. Tolochko, Y.V. Khlopkov, S.E. Mozzharov, M.B. Ignatiev, T. Laoui, V.I. Titov, Absorptance of powder materials suitable for laser sintering, Rapid Prototyp. J. 6 (3) (2000) 155–161.
[19] M. Rombouts, J.P. Kruth, L. Froyen, P. Mercelis, Fundamentals of selective laser melting of alloyed steel powders, CIRP Ann-Manuf. Technol. 55 (1) (2006) 187–192.
[20] I. Yadroitsev, I. Smurov, Selective laser melting technology: from the single laser melted track stability to 3D parts of complex shape, Phys. Procedia 5 (2010) 551–560.
[21] N.T. Aboulkhair, N.M. Everitt, I. Ashcroft, C. Tuck, Reducing porosity in AlSi10Mg parts processed by selective laser melting, Addit. Manuf. 1 (2014) 77–86.
[22] A.S.T.M. Standard, Standard test methods of compression testing of metallic materials at room temperature, 1990 Annual Book of ASTM Standards, ASTM, West Conshohocken, PA, 1990, pp. 98–105.
[23] S.L. Kharatyan, H.A. Chatilyan, M.A. Aghayan, M.A. Rodriguez, Non-isothermal phenomena in Mo/Si diffusion couple, reaction kinetics and structure formation, Int. J. 22 (1) (2013) 18–26.
[24] N.P. Novikov, I.P. Borovinskaya, A.G. Merzhanov, Thermodynamic analysis of self-propagating high-temperature synthesis reactions, in: A.G. Merzhanov (Ed.), Combustion Processes in Chemical Technology and Metallurgy, Chernogolovkaya, 1975.
[25] C. Suryanarayana, Synthesis of nanocomposites by mechanical alloying, J. Alloys Compd. 509 (1) (2011) 229–234.

Paper II

Minasyan, T., Liu, L., Holovenko, Y., Aydinyan, S., & Hussainova, I. (2019). Additively manufactured mesostructured $MoSi_2$-Si_3N_4 ceramic lattice. *Ceramics International*, 45(8), 9926-9933.

Ceramics International 45 (2019) 9926–9933

Contents lists available at ScienceDirect

Ceramics International

journal homepage: www.elsevier.com/locate/ceramint

Additively manufactured mesostructured $MoSi_2$-Si_3N_4 ceramic lattice

Tatevik Minasyan[a,*], Le Liu[a], Yaroslav Holovenko[a], Sofiya Aydinyan[a], Irina Hussainova[a,b,**]

[a] Tallinn University of Technology, Ehitajate tee 5, Tallinn, 19086, Estonia
[b] ITMO University, Kronverkskiy 49, St. Petersburg, 197101, Russian Federation

ARTICLE INFO

Keywords:
Additive manufacturing
Selective laser melting
Combustion synthesis
Ceramic composites
Lattice mesostructures
Molybdenum disilicide
Silicon nitride

ABSTRACT

Lattice structures, their shape, orientation, and density make the critical building blocks for macro-scale geometries during the AM process and, therefore, manipulation of the lattice structure extends to the overall quality of the final product. This work reports on manufacturing of $MoSi_2$-Si_3N_4 ceramic lattices through a selective laser melting (SLM) approach. The strategy first employs the production of core-shell structured $MoSi_2$/(10-13 wt%)Si composite powders of 3–10 μm particle size by combustion synthesis followed by SLM assembly of $MoSi_2$/Si lattices and their further nitridation to generate $MoSi_2$-Si_3N_4 mesostructures of designed geometry. Experimental results revealed that the volumetric energy density of SLM laser has remarkable influence on the cell parameters, strength, porosity and density of lattices. Under compressive test, samples sintered at a higher laser current demonstrated a higher strength value. Selective laser melting has shown its potential for production of cellular lattice mesostructures of ceramic-based composites with a low content of a binder metal, which can be subsequently converted into a ceramic phase to produce ceramic-ceramic structure.

1. Introduction

Recent developments in additive manufacturing (AM) techniques and architectural design foster progress in fabrication of materials for special not-available-before applications. With a compound annual growth rate of approximately 35%, AM industry reached its maturity in printing fully dense bulk volumes in a layer-wise fashion by melting some of the metallic powders with the help of a high-energy source such as laser or electron beam. As opposed to conventional subtractive or formative techniques, within the several design possibilities enabled by metal AM through a selective laser melting (SLM), cellular structures such as honeycombs and lattices are particularly exciting research frontier. Lattice structures and mesostructures offer advantages that cannot be easily availed from bulk structures. The list of the advantages is not limited by only increase in stiffness-to-weight ratios, energy absorption capability and thermal performance, but also includes digitally controlled architectures for bio-medical and catalysts applications. The ability to tailor mechanical properties spatially, which originates from the use of cellular geometries, is essentially attained by leveraging the fact that cellular structures allow for tuning the allocation of material and space at a finer level than is attainable through traditional homogeneous structures and at a more accessible level of scale than at the microstructural level [1].

Ceramic additive manufacturing has the potential to radically change the market. Ceramic materials attract the attention of research community and industry due to the impressive properties, including elevated temperature capability, good wear resistance and high strength. Despite the fact that significant progress has been made in the development of advanced ceramic composites, the main limitations for high-technological applications are set by geometrical design and structural complexity [2–4]. From a mechanical engineering viewpoint, a key advantage offered by cellular materials is a high strength accompanied by a relatively low mass, good energy absorption characteristics, thermal and acoustic insulation properties [5–9].

SLM process, as one of the most developed AM technologies, is a captivating technique, capacitating manufacture of tailorable complex configurations with a minimal wastage [10] applicable to the direct production of functional components. However, these techniques' adoption by industry is currently impeded by certain technical barriers: the residual stresses from rapid heating followed by the solidification during the manufacturing can introduce cracks or even entire structural failure. SLM typically requires a material with a relatively low melting point and sufficient thermal conductivity, good laser adsorption and wettability. Recently, the SLM has been intensively studied for polymers, metals and their composites [11]. However, AM through SLM approaches to consolidate defects-free ceramics rarely reported due to

* Corresponding author. Tallinn University of Technology, Ehitajate tee 5, 19086, Tallinn, Estonia.
** Corresponding author. Tallinn University of Technology, Ehitajate tee 5, 19086, Tallinn, Estonia.
E-mail addresses: tatevik.minasyan@taltech.ee (T. Minasyan), irina.hussainova@taltech.ee (I. Hussainova).

https://doi.org/10.1016/j.ceramint.2019.02.035
Received 16 January 2019; Received in revised form 5 February 2019; Accepted 5 February 2019
Available online 06 February 2019

the extremely high melting point, poor thermal shock resistance and low or no plasticity of ceramic materials [12,13].

In this study, we focus on design of an open-pore ceramic cellular lattice mesostructures of geometric complexity coupled with freedom of tool-less manufacturing. High temperature ceramics, specifically molybdenum disilicide ($MoSi_2$), are candidate materials for high-temperature applications connected to the high melting point, high hardness, moderate density and acceptable oxidation resistance. However, molybdenum disilicide possesses poor machinability due to its low fracture toughness at room temperature and a low creep resistance at temperatures above 1200 °C, which limits the scope of its applications [14]. This can be offset by chemically adding compatible constituents and toughening agents in the form of a tougher ceramic. Among those ceramics, Si_3N_4 is one of the suitable additives for fabrication of a composite material along with $MoSi_2$ [15–19].

In this work, we report a novel approach to prepare 15-20 wt%Si_3N_4 reinforced $MoSi_2$ cellular lattices. This approach is centered on the preparation of a $MoSi_2$/Si core-shell structured composite powder by energy saving combustion synthesis technique [20,21].

In general, the particles used for laser sintering are required to be of a spherical shape in a micrometer range possessing sufficient flowability. Moreover, the inherent physical and chemical properties of materials, such as thermal absorptivity and conductivity, melt viscosity and surface tension, crystallization temperature and velocity, bulk density and liquidity, have to be carefully considered when selecting the ceramic precursor powders for the SLM process [2,12,18,22].

In the frame of this work, we have developed core-shell structured $MoSi_2$/Si powder, where the silicon shell serves as a binder phase providing relevant laser absorption, while the $MoSi_2$ core provides mechanical durability. Furthermore, the powder has been subjected to the SLM followed by nitridation in nitrogen environment. It is demonstrated that the $MoSi_2$/Si lattices can be fabricated through SLM and converted into $MoSi_2$-Si_3N_4 ceramic-ceramic composite keeping structural integrity and functionality. This study shows an applicability of AM in combination with carefully designed powder precursors and process optimization for creation of complex ceramic structures with tailored geometry and mechanical properties.

2. Experimental

2.1. Combustion synthesis of $MoSi_2$/Si

Elementary powders of Mo (> 99.9%, 1–5 μm, 1.27 m^2g^{-1} SSA, Aldrich) and silicon Si (> 99%, < 20 μm, average particle size 4 μm, 3.37 m^2g^{-1} SSA, Silgrain-Elkem, Norway) were used for the combustion synthesis of $MoSi_2$/Si composite powders. The green mixture of reactants was mixed in a ceramic mortar for 15 min and die-pressed at room temperature under uniaxial pressure of 4 MPa to prepare the cylindrical samples with height of 25–30 mm and diameter of 40 mm. To record temperature-time profiles of the combustion process, two C-type tungsten-rhenium thermocouples (wire diameter 0.2 mm) covered with a thin layer of boron nitride were placed into holes (diameter 2 mm, depth 10 mm) drilled in each sample. The samples were then placed into a reaction chamber CPR-3.5l. To initiate the combustion reaction, the short-term annealing of tungsten coil (18 V, 2 s) positioned on the upper surface of the sample was employed. Maximum combustion temperature (T_c) for each sample was calculated as an average maximum for two temperature profiles. The combustion velocity was calculated as: $U_c = L/t$, where L is the distance between the thermocouples, and t is a time interval between signals from the thermocouple. The standard measurement error for T_c and U_c were ± 20 °C and 5%, respectively. The sample was crushed into powder and sieved by < 20 μm mesh for subsequent consolidation.

2.2. Selective laser melting of $MoSi_2$/Si

The consolidation of $MoSi_2$/Si lattices by selective laser melting was carried out in Metal 3D Printer (SLM ReaLizer 50) equipped with Yb:YAG fiber laser, with a maximum power of 120 W and wavelength of 1.07 μm. The whole manufacturing process is carried out inside a chamber containing a precisely controlled atmosphere of an inert gas; in this case nitrogen at oxygen level below 500 ppm was used to avoid the oxidation or degradation of the material. The SLM procedure was based on a digital model constructed and transferred to a three-dimensional physical object. During the process, the powder was evenly distributed on a platform and the product was generated layer by layer through temporally and selectively melting of the powder by a laser.

The lattice structures were generated to a specific controlled volume fractions and unit cell size. The volume fraction of the lattices defines the relative solid volume of the structure; if this value is low, it may result in loss of connectivity between the adjacent cells in the structure, and very high values may result in a closed structure volume. The cell size refers to the size of a single unit cell forming the lattice structure network. The lattices with 1 mm unit cells were designed by Magic software.

The SLM process parameters have detrimental effect on the manufacturability and integrity of components. The processing parameters used in this study were as follows: the laser current (I) was changed from 1500 to 4000 mA, the scanning time per point, point distance, the scan spacing (h) and the layer thickness (d) were fixed as 125 μs, 10 μm, 60 μm, and 25 μm, respectively. As a result, a scanning speed (ν) was fixed at optimized value of 80 mm s^{-1}, and a volumetric energy density (E) was altered from 200 to 800 J mm^{-3}. The laser current and the laser energy density are listed in Table 1.

The set of cellular lattice structures for each composite with the diameter of 10 mm and the height of 5 mm were built on a stainless steel base platform. The design of lattice structure permitted easy removal of the loose powder trapped inside the structures when the process is completed. Using designed systematic experimental methodology, the sintering parameters of SLM were optimized.

2.3. Nitridation and characterization

The $MoSi_2$/Si specimens consolidated by the selective laser melting were heated in the furnace (WEBB, USA) at 1350 °C (V_h = 10 °C min^{-1}, t = 3 h) in N_2 (purity 99.999 vol%) gas flow of 200 sccm. Schematic view on the $MoSi_2$-Si_3N_4 lattice preparation is depicted in Fig. 1. Phase compositions of the samples were analyzed with the help of X-ray diffractometer (Siemens, Bruker (USA), D5005 analyzer with CuKα radiation). The samples were irradiated with CuKα radiation at 40 kV and 30 mA, in θ-2θ scan with a step size of 0.02° and a count time of 0.4 s.

The concentrations of elements were calculated using Rietveld refinement method, which was performed by quantitative analysis of the crystalline phases detected by corresponding XRD patterns. The evolution of the surface morphology was examined with a high-resolution scanning electron microscope (HR-SEM Zeiss Merlin) equipped with an

Table 1
Sintering parameters for $MoSi_2$-10 wt%Si and $MoSi_2$-13 wt% composites with a fixed scanning speed of 80 mm s^{-1}

Laser current (mA)	Laser Energy density (J·mm^{-3})
1000	200
1500	300
1700	340
2000	400
2500	500
3000	600
3500	700
4000	800

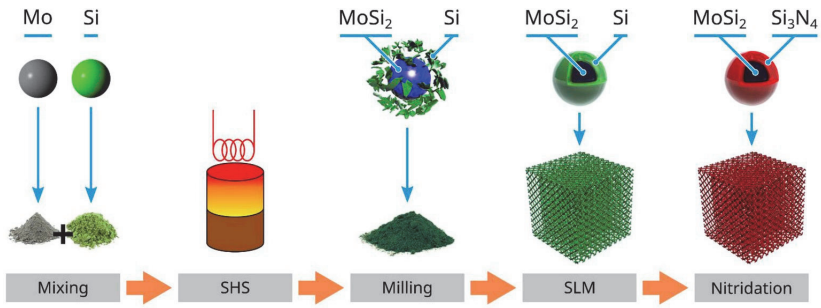

Fig. 1. Schematic representation of the process of $MoSi_2$-Si_3N_4 lattice preparation.

In-Lens SE detector for topographic imaging and In-Lens energy selective backscattered detector for compositional contrast. Measurements were made at operating voltage of 2 kV. The chemical composition of the samples was determined using an energy dispersive X-ray analysis (EDS) system (Bruker EDX-XFlash6/30 detector).

Compression tests were conducted using an Instron 5869 machine equipped with a laser extensometer at controlled crosshead speed of 0.5 mm min^{-1}. The tests were performed at least three times for identical specimens. X-ray computed tomography (XCT) system YXLON FF35 CT as a volumetric measurement tool was conducted to evaluate the close porosity and volume defects.

3. Results and discussion

3.1. Combustion laws in the Mo-Si system

Combustion synthesis of $MoSi_2$/(10-13 wt%)Si composite powders was accomplished from the corresponding Mo-Si mixtures. To study the dependence between the amount of free silicon and combustion parameters (combustion wave propagation velocity and maximum temperature of combustion process), the temperature profiles for each reaction were examined. It was demonstrated that the addition of more than 15% of silicon to the stoichiometric (Mo + 2Si) mixture results in interruption of self-sustaining reaction between Mo and Si. Fig. 2 demonstrates temperature-time histories of the combustion of Mo + 2Si + (10-13 wt%)Si mixtures. The addition of 10–13 wt% of silicon into Mo + 2Si system (T_{ad} = 1650 °C) fluently decreases the combustion temperature by 100 °C, as the additional amount of silicon acts as a thermal diluent and absorbs the heat released during Mo + 2Si reaction.

The XRD patterns of combustion synthesized $MoSi_2$/(10-13 wt%)Si composites indicate only characteristics peaks of $MoSi_2$ and Si, Fig. 3. With increase in silicon content in the initial mixture, the intensity of the corresponding peaks of free silicon in the product increases. Table 2 lists the weight and volume content of free silicon in produced $MoSi_2$/Si composites.

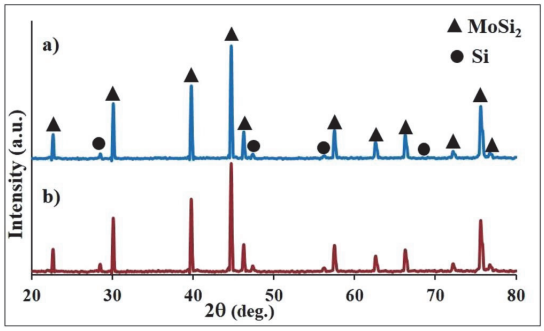

Fig. 3. XRD patterns of $MoSi_2$-10 wt%Si (a) and $MoSi_2$-13 wt%Si (b) samples.

Table 2
Weight and volume percentage of Si in $MoSi_2$-Si composites.

Composite	Wt.% of free Si by XRD	Vol. % of free Si
$MoSi_2$-10 wt%Si	10.0	22.9
$MoSi_2$-13 wt%Si	13.0	28.7

SEM images of the crushed powder, shown in Fig. 4, illustrate $MoSi_2$/Si powders with particles of 3–10 μm in size.

According to the EDS mapping (Fig. 4, c-f), silicon was melted in both systems developing "core-shell" structured particulates. In the silicon rich composite (13%), a silicon fuse (shell) covers the $MoSi_2$ particles (core) more homogeneously and binds ceramic particles together.

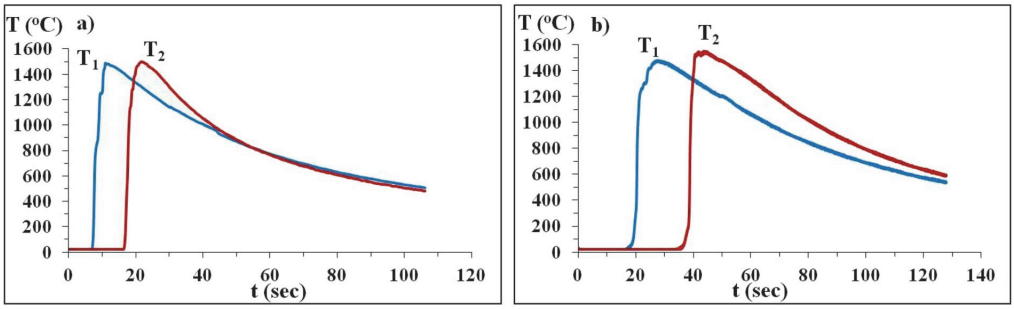

Fig. 2. Temperature profiles and combustion wave propagation velocity in Mo + 2Si + 10 wt%Si (a); and Mo + 2Si + 13 wt%Si (b) reaction mixtures.

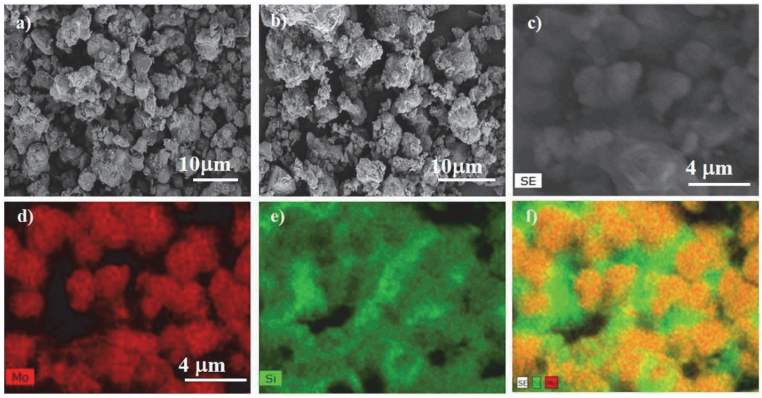

Fig. 4. SEM images of $MoSi_2$-10 wt%Si (a), $MoSi_2$-13 wt%Si (b) composite powders and EDS mapping results of $MoSi_2$-13 wt%Si (c–f).

3.2. *Selective laser melting of $MoSi_2$/(10-13 wt%)Si composites*

The fixed scanning speed of 80 mm s^{-1} and the increasing laser current (1000–4000 mA) resulted in an increase in the energy distributed per a unit volume (200–800 J mm^{-3}). As it was anticipated, the laser current has a key influence on the process of sintering. Using a relatively low laser current of < 1000 mA, the developed lattices appeared to be brittle and breakable during removal of the support from the platform. However, with increase in laser current to I = 4000 mA, the melt tends to splash caused by a high capillary instability of the melt due to overheating of local regions. A narrow process window via combination of a moderate scan speed and a laser energy density was determined to eliminate process defects and result in the formation of the anticipated structures.

XRD analysis of the sintered samples represented by Fig. 5 testifies the presence of $MoSi_2$ and Si only; therefore, new phases were not detected at solidification under the highest laser current. The EDS mapping presented in the co-authors study [12] has shown that a molten silicon shell framed and bonded the $MoSi_2$ particles supposing that, after SLM the composite maintains its core-shell microstructure.

Fig. 6 displays SEM images of the obtained lattices (I = 1500–2500 mA). Structural analysis exhibited that the wall thickness values are varied in a range of 380–490 μm, pore diameter - from 625 to 725 μm, and the period size is changed form 1050 up to 1170 μm. The laser power has a decisive influence on the strut-diameter of the lattices. In the partial melting process, a laser beam firstly melts

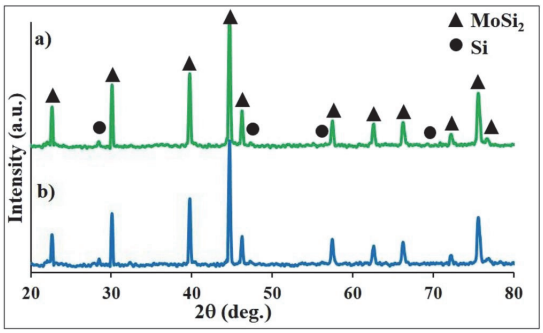

Fig. 5. XRD patterns of $MoSi_2$-10 wt%Si sintered at laser current of 2000 mA (a) and 3500 mA (b).

materials of a lower melting point. The molten metal serves as a binder for development of neck connections between ceramic particles and subsequently for construction of a 3D porous structure. The temperature gradients may cause Marangoni flow [23], which is significant for the ceramics containing composites. High ceramic content resulted in a low sintering shrinkage using a comparatively low laser current. With increase in the current up to 3000 mA, the wall thickness was apparently increased leading to an increase in the period size. The heat provided by laser of a higher current (I = 3500 mA) lowers the viscosity of the molten silicon which can flow to join into large droplets occupying the available room thus decreasing pore size and increasing wall thickness. Table 3 summarizes the geometrical parameters of the lattice structures.

Fig. 7 shows general landscape of lattices sintered by the laser operating at different currents. SEM micrographs of a higher magnification shown in Fig. 8 allow estimation of the wall thickness, which is varied in a range of 300–350 μm, the pore diameters - in a range of 750–850 μm, and the period size - in 1100–1200 μm intervals. The geometrical parameters of the lattices are specified in Table 4.

Balling effect is one of the objectionable issues that may be encountered by the SLM-produced parts due to localized irregularities or capillary instability of the melts [24]. Balling effect is important for systems of poor wettability between the molten pool and underlying solid, causing the molten pool to break up into the spheres as can be clearly recognized from the SEM images in Figs. 6–8. Balling, as an undesirable phenomenon, is a complex physical metallurgical process and requires close consideration in the nearest future for a certain system under study.

The $MoSi_2$/10 wt%Si sample shown in Fig. 6 possesses relatively thick lattice walls as compared to the $MoSi_2$/13 wt%Si samples, Figs. 7 and 8. The thicker lattice of $MoSi_2$/10 wt%Si can be explained by the scanning of several neighboring layers around a melt pool. The superheated melt pool of silicon heats neighboring powder layers causing the growth of lattice walls. The additionally bonded layers cause weak interparticle and interlayer binding and lead to the formation of cracks. In case of high content of Si, the energy source from laser provides stable melt pool and causes smooth scan tracks and thinner walls.

The laser energy density is a function of the key processing factors for the densification and the quality of SLM fabricated parts, thereby determining their properties [25]. Increasing laser power and/or decreasing scan speed, layer thickness, scan spacing would increase the laser energy density and, therefore, the temperature of the powder. A higher incident laser energy density results in a larger amount of melting and higher final density. Expectedly, the density of lattice

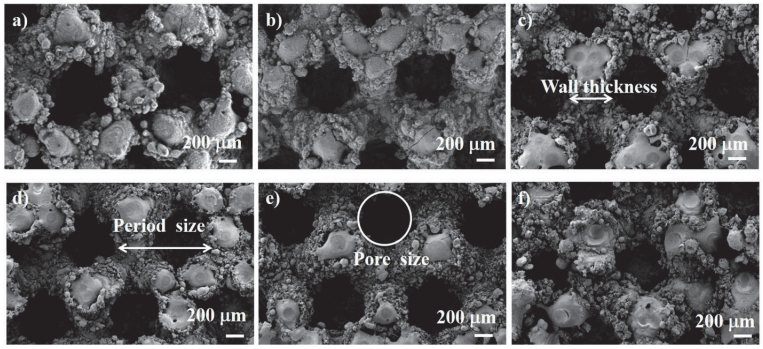

Fig. 6. SEM images of $MoSi_2$-10wt%Si lattices sintered at 1500 (a), 1700 (b), 2000 (c), 2500 (d), 3000 (e) and 3500 mA (f) laser current.

Table 3
Wall thickness, pore size and period size values for $MoSi_2$-10 wt%Si lattices sintered at 1500–3500 mA laser current.-

Current (mA)	Pore diameter (µm)	Wall thickness (µm)	Period size (µm)
1500	650–670	390–450	1040–1120
1700	700–730	395–450	1095–1180
2000	670–685	380–470	1050–1155
2500	625–680	400–455	1025–1135
3000	620–695	480–535	1100–1230
3500	590–610	450–510	1040–1120

structures produced at a high laser current is higher as compared to the lattices fabricated at currents lower than 2500 mA, Table 5.

According to the high-resolution X-ray computed tomography, $MoSi_2$/13 wt%Si lattice (I = 2500 mA) has the ratio of volume defects of about 0.5–0.9%.

The presence of cracks can be noticed from SEM images of both systems attributed to the combination of thermal accumulation effect and the change of thermal conductivity owing to the transition from powder to solid. In the case of the procedure including a partial melting, residual stresses are very probable events. The magnitude of residual stress is closely related to the material properties, particularly the modulus of elasticity (E_{Si} = 168 GPa [26], $E_{MoSi2} \approx$ 387–515 GPa [27]) and the coefficient of thermal expansion (CTE) (CTE_{Si} = 2.59–4.56·10^{-6} K^{-1} [28], CTE_{MoSi2} = 8.6·10^{-6} K^{-1} [29]), as well as the laser processing conditions. For instance, metal matrix composites with reinforcement that has a close CTE to a metal matrix is preferred. Moreover, the microscopic cracks are usually developed due to rapid solidification and low ductility of the material.

The representative stress–strain curves of the compression tests on the cellular lattice mesostructures fabricated at the laser current of 1500 and 3500 mA are displayed in Fig. 9. These two specimens sintered with application of 1500 and 3500 mA laser current (having the highest and the lowest densities) were subjected to progressively increasing compression.

The compressive modulus of elasticity (E) for $MoSi_2$/10 wt%Si (I = 1500 mA) and $MoSi_2$/10 wt%Si (I = 3500 mA) were 0.9 GPa and 0.66 GPa; the yield (σ_y) and ultimate strengths (σ_u) were 3.3 MPa and 3.8 MPa, 8.7 MPa and 9.3 MPa, respectively. The average values of E, σ_y, σ_u and maximum compressive strain measured for the specimens under consideration are summarized in Table 6. The samples of a higher density showed both high ultimate and compressive strength.

3.3. Nitridation of selective laser sintered $MoSi_2$/Si samples

To achieve near-net shaped ceramic lattices with a designated porosity and controlled permeability to specific liquids, we attempted to nitridize $MoSi_2$/(10-13 wt%)Si lattice shaped specimens in nitrogen atmosphere to convert Si into Si_3N_4. The theoretical amounts of Si_3N_4 after nitridation of $MoSi_2$/10 wt%Si and $MoSi_2$/13 wt%Si composites are 15.6 wt% and 19.9 wt%, respectively.

According to the XRD pattern of the product after nitridation, the samples mostly contain $MoSi_2$ and Si_3N_4, and a small amount of Mo_5Si_3, (Fig. 10 a). Mo_5Si_3 belongs to a class of complex body-centered tetragonal structures with the melting point to be higher as compared to $MoSi_2$; therefore, some improvement of creep resistance is expected [30].

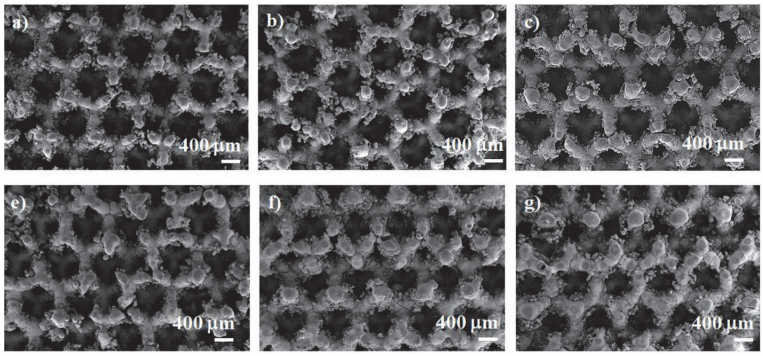

Fig. 7. SEM images of $MoSi_2$-13 wt%Si lattices sintered at 1500 (a), 1700 (b), 2000 (c), 2500 (d), 3000 (e) and 3500 mA (f) laser current.

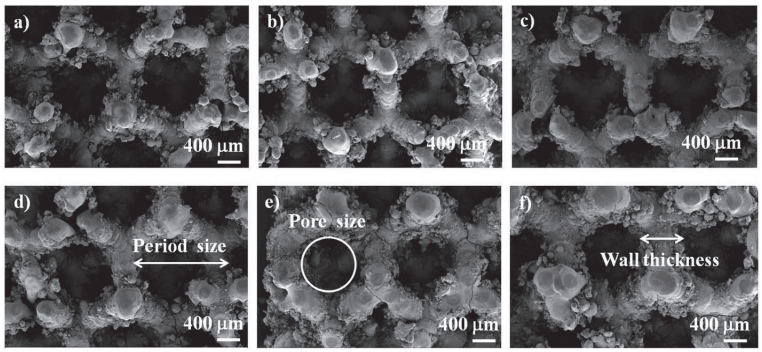

Fig. 8. SEM images of $MoSi_2$-13 wt%Si lattices sintered at 1500 (a), 1700 (b), 2000 (c), 2500 (d), 3000 (e) and 3500 mA (f) laser current with higher magnification.

Table 4
Wall thickness, pore size and period size values for $MoSi_2$-13 wt%Si lattices sintered at 1500–3500 mA laser current.

Current (mA)	Pore diameter (μm)	Wall thickness (μm)	Period size (μm)
1500	755–780	345–360	1100–1150
1700	765–795	300–355	1065–1150
2000	800–850	330–350	1130–1200
2500	740–770	300–355	1040–1125
3000	750–765	330–350	1080–1115
3500	760–780	325–340	1085–1120

Table 5
The apparent density of $MoSi_2$-(10-13 wt%)Si lattices sintered at different laser currents.

Current (mA)	Apparent Density ($g{\cdot}cm^{-3}$)		Apparent relative density (%)	
	$MoSi_2$-10 wt% Si	$MoSi_2$-13 wt% Si	$MoSi_2$-10 wt% Si	$MoSi_2$-13 wt% Si
1500	1.81	1.68	33.82	32.76
1700	1.70	1.66	31.76	32.37
2000	1.85	1.64	34.57	31.98
2500	2.13	1.84	39.80	35.88
3000	2.06	2.22	38.49	43.29
3500	2.80	2.43	52.32	47.38

The tomography analysis following to the nitridation of the lattices showed that the portion of volume defects was decreased to 0.3%.

SEM analysis of nitridized $MoSi_2$/Si lattices obviously indicates the presence of Si_3N_4 nanofibers grown on the surfaces and discontinuouses of the lattices (Fig. 10 b-e).

After heating the $MoSi_2$/(10-13 wt%)Si samples in nitrogen, the wall thickness of the lattices was changed by 5–10 μm keeping the period size in the same range (Table 7).

After the compression test of nitridized $MoSi_2$/10%wt.Si lattice (I = 1500 mA), the compressive modulus of elasticity (E) was 0.29 GPa, the yield (σ_y) and ultimate strengths (σ_u) were 3 MPa and 5.7 MPa, respectively. The compressive strain of the nitridized sample (6.68%) was higher as compared to the compressive strain of untreated sample (4.17%), Fig. 11.

4. Conclusions

Selective laser melting has shown its potential for production of cellular lattice mesostructures of ceramic-based composites with a low content of a binder metal, which can be subsequently converted into a ceramic phase. In this work, the core-shell structured $MoSi_2$/(10-13 wt %)Si powders with an average particle size of 3–10 μm were synthesized by the combustion synthesis technique and were used for fabrication of $MoSi_2$/Si cellular mesostructures. The parameters of SLM process, particularly the laser current, have a significant effect on the internal and external architecture of the lattices. The change of the laser energy density from 300 to 700 J mm^{-3} results in the textile growth of lattices increasing the apparent relative density of the $MoSi_2$-Si lattices from ~34 to 52%. High laser energy densities prone to increase wall thickness of lattice structures at a constant period size.

Nitridation of $MoSi_2$/Si mesostructures results in production of $MoSi_2$-Si_3N_4 composites with an insignificant content of Mo_5Si_3 phase and reducing volume defects.

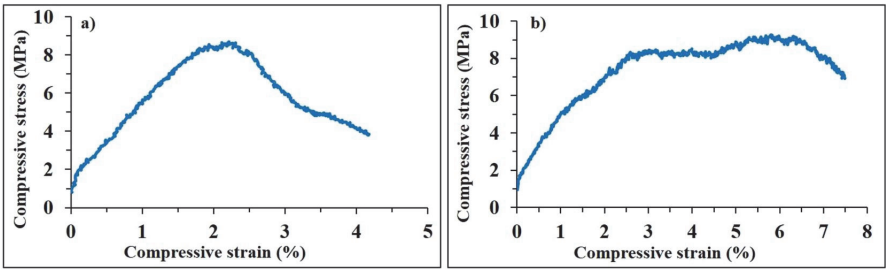

Fig. 9. Compressive stress-strain curve of selective laser melted $MoSi_2$-10 wt%Si lattice using 1500 mA (a) and 3500 mA (b) laser current.

Table 6
Mechanical properties of $MoSi_2$-10 wt%Si lattice (I = 1500 and 3500 mA).

Sample	Compressive modulus of elasticity (E) (GPa)	The yield (σ_y) (MPa)	Ultimate strength (σ_u) (MPa)	Compressive strain (%)
$MoSi_2$-10 wt%Si (1500 mA)	0.9	3.3	8.7	4.17
$MoSi_2$-10 wt%Si (3500 mA)	0.66	3.8	9.3	7.48

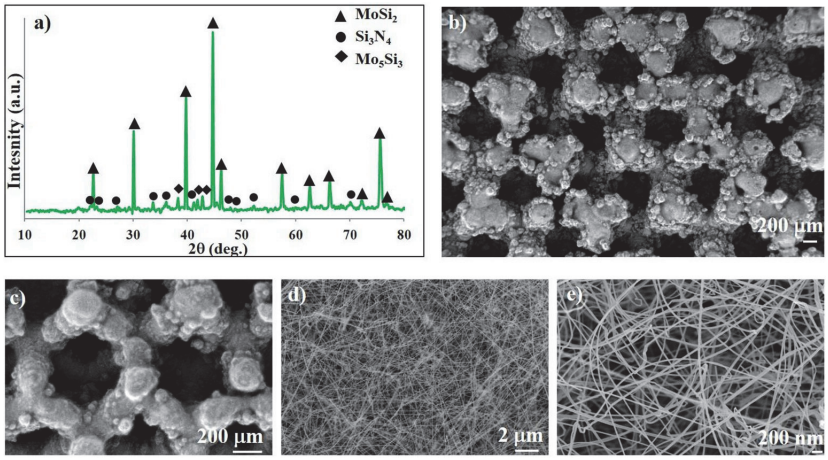

Fig. 10. XRD pattern (a) and SEM images (b–e) of $MoSi_2$-13 wt%Si lattice after nitridation (I = 2500 mA).

Table 7
Lattice parameters of $MoSi_2$-(10-13 wt%)Si before and after nitridation.

Sample	Before nitridation			After nitridation		
	Pore diameter (μm)	Wall thickness (μm)	Period size (μm)	Pore diameter (μm)	Wall thickness (μm)	Period size (μm)
$MoSi_2$-10 wt%Si	625–680	400–455	1025–1135	620–690	420–460	1040–1150
$MoSi_2$-13 wt%Si	740–770	300–355	1040–1125	710–780	310–350	1020–1130

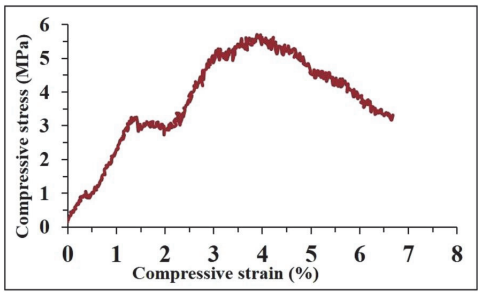

Fig. 11. Compressive stress-strain curve of nitridation product of selective laser melted $MoSi_2$-10 wt%Si lattice (I = 1500 mA).

Acknowledgements

This work was supported by the Mobilitas Pluss Postdoctoral Researcher Grant project MOBJD166 (S. Aydinyan), the Estonian Research Council PSG220 (S. Aydinyan) and PUT1063 (I. Hussainova). The authors would like to thank also the European Regional Fund, project number 2014-2020.4.01.16-0183 (Smart Industry Centre). The authors would like to thank also the European Regional Fund, project number 2014-2020.4.01.16-0183 (Smart Industry Centre).

Appendix A. Supplementary data

Supplementary data to this article can be found online at https://doi.org/10.1016/j.ceramint.2019.02.035.

References

[1] D. Bhate, Modelling the mechanical behaviour of additively manufactured cellular structures, Metal. AM. Magazine 2 (4) (2016) 51–55 http://www.padtinc.com/blog/additive-mfg/metal-am-magazine-article-modeling-the-mechanical-behaviour-of-additively-manufactured-cellular-structures.
[2] A.N. Chen, J.M. Wu, K. Liu, J.Y. Chen, H. Xiao, P. Chen, Y.S. Shi, High-performance ceramic parts with complex shape prepared by selective laser sintering: a review, Adv. App. Ceram. 117 (2) (2018) 100–117 https://doi.org/10.1080/17436753.2017.1379586.
[3] M. Bogers, R. Hadar, A. Bilberg, Additive manufacturing for consumer-centric business models: Implications for supply chains in consumer goods manufacturing, Technol. Forecast. Soc. Change 102 (2016) 225–239 https://doi.org/10.1016/j.techfore.2015.07.024.
[4] S. Ford, M. Despeisse, Additive manufacturing and sustainability: an exploratory study of the advantages and challenges, J. Clean. Prod. 137 (2016) 1573–1587 https://doi.org/10.1016/j.jclepro.2016.04.150.
[5] A. Hussein, L. Hao, C. Yan, R. Everson, P. Young, Advanced lattice support structures for metal additive manufacturing, J. Mater. Process. Technol. 213 (7) (2013) 1019–1026 https://doi.org/10.1016/j.jmatprotec.2013.01.020.
[6] C. Chu, G. Graf, D.W. Rosen, Design for additive manufacturing of cellular structures, Comput. Aided Des. Appl. 5 (5) (2008) 686–696 https://doi.org/10.3722/cadaps.2008.686-696.
[7] J. Chu, S. Engelbrecht, G. Graf, D.W. Rosen, A comparison of synthesis methods for cellular structures with application to additive manufacturing, Rapid Prototyp. J. 16 (4) (2010) 275–283 https://doi.org/10.1108/13552541011049298.
[8] C. Yan, L. Hao, A. Hussein, D. Raymont, Evaluations of cellular lattice structures

manufactured using selective laser melting, Int. J. Mach. Tool Manuf. 62 (2012) 32–38 https://doi.org/10.1016/j.ijmachtools.2012.06.002.
[9] F. Brenne, T. Niendorf, H.J. Maier, Additively manufactured cellular structures: Impact of microstructure and local strains on the monotonic and cyclic behavior under uniaxial and bending load, J. Mater. Process. Technol. 213 (9) (2013) 1558–1564 https://doi.org/10.1016/j.jmatprotec.2013.03.013.
[10] M. Cloots, A. Spierings, K. Wegener, Assessing new support minimizing strategies for the additive manufacturing technology SLM, Solid Freeform Fabrication Symposium (SFF), Austin, TX, 2013, pp. 631–643.
[11] E. Herderick, Additive manufacturing of metals: A review (MS) ASM International (176252), Mater. Sci. Technol. (2011) 1413–1425.
[12] T. Minasyan, M. Aghayan, L. Liu, S. Aydinyan, L. Kollo, I. Hussainova, M.A. Rodríguez, Combustion synthesis of $MoSi_2$ based composite and selective laser sintering thereof, J. Eur. Ceram. Soc. 38 (11) (2018) 3814–3821 https://doi.org/10.1016/j.jeurceramsoc.2018.04.043.
[13] A. Gahler, J.G. Heinrich, J. Guenster, Direct Laser Sintering of Al_2O_3–SiO_2 Dental Ceramic Components by Layer-Wise Slurry Deposition, J. Am. Ceram. Soc. 89 (10) (2006) 3076–3080 https://doi.org/10.1111/j.1551-2916.2006.01217.x.
[14] S.R. Srinivasan, R.B. Schwarz, Elastic moduli of $MoSi_2$-based materials, J. Mater. Res. 7 (7) (1992) 1610–1613 https://doi.org/10.1557/JMR.1992.1610.
[15] J.K. Yoon, G.H. Kim, J.H. Han, I.J. Shon, J.M. Doh, K.T. Hong, Low-temperature cyclic oxidation behavior of $MoSi_2$/Si_3N_4 nanocomposite coating formed on Mo substrate at 773 K, Surf. Coating. Technol. 200 (7) (2005) 2537–2546 https://doi.org/10.1016/j.surfcoat.2005.01.035.
[16] M.C. Kushan, Y. Uzunonat, S.C. Uzgur, F. Diltemiz, Potential of $MoSi_2$ and $MoSi_2$-Si_3N_4 composites for aircraft gas turbine engines, in: Ramesh Agarwal (Ed.), Recent Advances in Aircraft Technology, 2012 ISBN:978–953-51–0150-5.
[17] A.H. Bartlett, R.G. Castro, Elevated temperature mechanical properties of $MoSi_2$/Si_3N_4, $MoSi_2$/SiC composites produced by self-propagating high temperature synthesis, J. Mater. Sci. 33 (6) (1998) 1653–1660 https://doi.org/10.1023/A:1017536408913.
[18] T. Minasyan, L. Liu, M. Aghayan, L. Kollo, K.N. Kamboj, S. Aydinyan, I. Hussainova, A novel approach to fabricate Si_3N_4 by selective laser melting, Ceram. Int. 44 (2018) 13689–13694 https://doi.org/10.1016/j.ceramint.2018.04.208.
[19] K.V. Manukyan, S.L. Kharatyan, G. Blugan, P. Kocher, J. Kuebler, $MoSi_2$-Si_3N_4 composites: Influence of starting materials and fabrication route on electrical and mechanical properties, J. Eur. Ceram. Soc. 29 (10) (2009) 2053–2060 https://doi.org/10.1016/j.jeurceramsoc.2008.12.015.
[20] T. Minasyan, H. Kirakosyan, S. Aydinyan, L. Liu, S. Kharatyan, I. Hussainova, Mo-Cu pseudoalloys by combustion synthesis and spark plasma sintering, J. Mater. Sci. 53 (24) (2018) 16598–16608 https://doi.org/10.1007/s10853-018-2787-1.
[21] S.T. Aruna, A.S. Mukasyan, Combustion synthesis and nanomaterials, Curr. Opin. Solid. St. M. 12 (3–4) (2008) 44–50 https://doi.org/10.1016/j.cossms.2008.12.002.
[22] S. Kolosov, G. Vansteenkiste, N. Boudeau, J.C. Gelin, E. Boillat, Homogeneity aspects in selective laser sintering (SLS), J. Mater. Process. Technol. 177 (1–3) (2006) 348–351 https://doi.org/10.1016/j.jmatprotec.2006.03.188.
[23] S.L. Sing, W.Y. Yeong, F.E. Wiria, B.Y. Tay, Z. Zhao, L. Zhao, S. Yang, Direct selective laser sintering and melting of ceramics: a review, Rapid Prototyp. J. 23 (3) (2017) 611–623 https://doi.org/10.1108/RPJ-11-2015-0178.
[24] N.K. Tolochko, S.E. Mozzharov, I.A. Yadroitsev, T. Laoui, L. Froyen, V.I. Titov, M.B. Ignatiev, Balling processes during selective laser treatment of powders, Rapid Prototyp. J. 10 (2) (2004) 78–87 https://doi.org/10.1108/13552540410526953.
[25] L.C. Zhang, H. Attar, Selective laser melting of titanium alloys and titanium matrix composites for biomedical applications: a review, Adv. Eng. Mater. 18 (4) (2016) 463–475 https://doi.org/10.1002/adem.201500419.
[26] M. Nakamura, S. Matsumoto, T. Hirano, Elastic constants of $MoSi_2$ and WSi_2 single crystals, J. Mater. Sci. 25 (7) (1990) 3309–3313 https://doi.org/10.1007/BF00587691.
[27] J. Pan, M.K. Surappa, R.A. Saravanan, B.W. Liu, D.M. Yang, Fabrication and characterization of SiC/$MoSi_2$ composites, Mater. Sci. Eng. A 244 (2) (1998) 191–198 https://doi.org/10.1016/S0921-5093(97)00553-4.
[28] Y. Okada, Y. Tokumaru, Precise determination of lattice parameter and thermal expansion coefficient of silicon between 300 and 1500 K, J. Appl. Phys. 56 (2) (1984) 314–320 https://doi.org/10.1063/1.333965.
[29] H. Choe, T. Hsieh, J. Wolfenstine, The effect of powder processing on the coefficient of thermal expansion of $MoSi_2$-Si_3N_4 composites, Mater. Sci. Eng. A 237 (2) (1997) 250–255 https://doi.org/10.1016/S0921-5093(97)00421-8.
[30] J. Yan, H. Xu, H. Zhang, S. Tang, $MoSi_2$ oxidation resistance coatings for Mo_5Si_3/$MoSi_2$ composites, Rare Met. 28 (4) (2009) 418–422 https://doi.org/10.1007/s12598-009-0081-8.

Paper III

Minasyan, T., Aydinyan, S., Liu, L., Volubujeva, O., Toyserkani, E., & Hussainova, I. (2020). Mo $(Si_{1-x},Al_x)_2$-based composite by reactive laser powder-bed fusion. *Materials Letters*, 128776.

Materials Letters 281 (2020) 128776

Contents lists available at ScienceDirect

Materials Letters

journal homepage: www.elsevier.com/locate/mlblue

$Mo(Si_{1-x},Al_x)_2$-based composite by reactive laser powder-bed fusion

T. Minasyan [a,c], S. Aydinyan [a], L. Liu [a], O. Volubujeva [b], E. Toyserkani [c], I. Hussainova [a,*]

[a] Department of Mechanical and Industrial Engineering, Tallinn University of Technology, Ehitajate 5, 19086 Tallinn, Estonia
[b] Department of Materials and Environmental Technology, Tallinn University of Technology, Ehitajate 5, 19086 Tallinn, Estonia
[c] Multi-scale Additive Manufacturing Laboratory, Department of Mechanical and Mechatronics Engineering, University of Waterloo, 200 University Ave., West Waterloo, Ontario N2L 3G1, Canada

ARTICLE INFO

Article history:
Received 11 July 2020
Received in revised form 22 August 2020
Accepted 28 September 2020
Available online 1 October 2020

Keywords:
$Mo(Si_{1-x},Al_x)_2$
Reactive laser powder-bed fusion
X-ray computed tomography
Hardness
Microstructure

ABSTRACT

Advantages and industrial importance of C40 $Mo(Si_{1-x},Al_x)_2$ structure for technical applications have been widely proven. This work details $Mo(Si_{1-x},Al_x)_2$ composite preparation by reactive selective laser melting of (Mo + 2Si) + 30 wt%AlSi10Mg powder. During the process, $Mo(Si_{1-x},Al_x)_2$ (x = 0.33) nucleates and grows as the primary phase alongside intergranular $Al_{0.85}Si_{0.15}$ from residual Al-Si eutectic liquid. The columnar dendritic structured laser-sintered composites exhibit 99% relative density and up to 500 HV5 hardness. The applied volumetric energy density between 67.2 and 112.0 J/mm^3 has remarkably influences on samples' microstructure with insignificant effect on density.

1. Introduction

Molybdenum disilicide ($MoSi_2$) is a promising intermetallic due to specific combination of physical and mechanical properties with excellent alloying potential for metals and other silicides [1–3]. However, low ductility/plasticity below the brittle-to-ductile transition temperature, low fracture toughness at ambient temperatures, and "pest" oxidation at low temperatures (773 K) limit its industrial applications [1]. The development of composites overcomes these drawbacks. Aluminum, as an alloying element to $MoSi_2$, is believed to enhance the oxidation resistance, fracture toughness, low temperature ductility, and to contribute to metallic nature of the compound. The validity of these assumptions still remains unclear. Aluminum is an excellent candidate to reduce composite weight and to suppress pest oxidation of $Mo(Si,Al)_2$ without compromising intermediate and high-temperature oxidation resistance [4]. The $Mo(Si,Al)_2$ based composites are promising materials for next generation structural applications at elevated temperatures, as they possess excellent oxidation resistance. Their main applications are ranged from heating elements in high-temperature furnaces to protective coatings [5].

Good processability of AlSi10Mg by selective laser melting (SLM) has recently garnered increasing research attention [6]. SLM, as LPBD manufacturing technique, offers design freedom compared to conventional manufacturing processes, and possibility of printing materials with new features and customized applications [7]. Various Al:Si ratios are tolerated by Mo(Al,Si)2 resulting in the development of $Mo(Si_{1-x},Al_x)_2$ with C40 hexagonal structures in a large homogeneity range ($0.11 < x < 0.5$) [6]. The hexagonal C40 is detected from x = 0.1 to 0.5, the orthorhombic C54 from x = 0.5, the monophase tetragonal C11b at x = 0, and the monophase C54 at $x = 0.6$ [8]. Laser powder-bed fusion (LPBF) of Mo-Si-Al systems have not been hitherto explored. In this context, the reactive SLM of Mo-Si-AlSi10Mg is demonstrated for the first time for stoichiometric mixture (Mo + 2Si) with 30 wt% AlSi10Mg alloy powder.

2. Experimental

The powders of Mo (PPM, Mo-7164, 99% purity, 1.0–3.0 μm), Si (Silgrain-Elkem, 99% purity, <20 μm) and AlSi10Mg (SLM Solutions, purity > 99%, 15–63 μm) were mixed by mechanical rotation for 2 h (20 rpm) according to weight ratio Mo:Si:AlSi10Mg = 44.2:25.8:30. Powder flowability was measured by Granudrum (GranuTools) with a drum rotation speed of 2–10 rpm. Differential scanning calorimetry (DSC) (NETZSCH-STA 449 F1) was performed to analyze thermal behavior at 25–1450 °C temperature range with 20 °C/min heating rate in argon environment. Cylindrical samples (∅10mm × 5mm) were manufactured by ReaLizer GmbH SLM-50 equipped with Yb:YAG fibre laser with the maximum power of 120 W. Argon was used as an inert gas in the build chamber.

* Corresponding author.
E-mail address: irina.hussainova@taltech.ee (I. Hussainova).

https://doi.org/10.1016/j.matlet.2020.128776
0167-577X/

The laser scanned bi-directionally (zigzag) in one direction (X-scan) with a subsequent 90° rotation for each next layer (XY-scan). Considering the optimal LPBF parameters reported elsewhere [7,9] for the preparation of AlSi10Mg and $MoSi_2$ bulks, the samples were produced using 100 W laser power (P). At fixed point distance (85 μm), hatching distance (85 μm), layer thickness (35 μm), the scanning speed (v) was set to 300, 350, 400 and 500 mm/s, respectively, for samples labelled A1-A4. The applied volumetric laser energy density (ED) was calculated to be 67.2, 83.9, 95.7 and 112.0 J/mm^3, respectively. Density was measured by Archimedes principles. Size, morphology and alignment of pores in as-built samples were studied by X-ray computed tomography (CT) (ZEISS Xradia 520 Versa) using 3D X-ray microscope. For microstructural examination, the specimens were polished to 1 μm finish, and evaluated by scanning electron microscope (HR-SEM Zeiss Merlin) equipped with EDS detector (Bruker EDX-XFlash6/30). The XRD patterns were collected by X-ray diffractometer (Siemens, D5005 analyzer with CuKα radiation). The phase composition was evaluated using Rietveld refinement method. Vickers hardness was estimated on polished surfaces using Indentec 5030 SKV at 49 N load (HV5) for 10 s and averaged for 5 indentations.

3. Results and discussion

Gas atomized spherical particles of AlSi10Mg (Fig. 1a), 2–3 μm spherical agglomerates of Mo (Fig. 1b) and irregular shaped Si particles (Fig. 1c) were dry mixed to prepare a feedstock for LPBF through SLM. The angle of repose and cohesion were measured to be 49° and 14.7, respectively, demonstrating the powder' applicability for processing. Micrographs of the samples sintered at 67.2–112.0 J/mm^3 ED (Fig. 1 e-l) illustrate diverse morphological textures as a result of the absorbed laser energy, solidification and cooling rates. Thermal gradient from cores of melt pools towards the periphery of step edges is a result of large heat flux in the center due to Gaussian intensity of the single-mode laser beam. At the center, perpendicular to the building direction, homogenously distributed fine columnar dendrites grow from the randomly oriented nuclei to the energetically favored directions. The nucleation starts at the substrate/powder interface and dendrites, which have the favorable growing toward the heat flow direction, develop opposite to the heat flow forming columnar dendrites. Further growth of dendrites to the centerline of sample results in formation of new dendrites with higher order arms. In contrast, LPBF built AlSi10Mg demonstrates fine cellular-dendritic structures [10]. In both cases, coarsening of dendrites to the border of the melt pools occurred. As heat dissipates from the back layer, the temperature gradient and the heat flux density perpendicular to the interface of layers is more intensive. Simultaneously, the eutectic liquid of alloy has a tight contact with the solid ceramic-intermetallic phase, and fast solidification of columnar dendrites results in preferential growth along the maximum temperature gradient.

The top view reveals an elliptical shape of the melt pools, which is often beheld as non-continuous indicating center segregation of Al-Si. At the bottom of the molten pool, solidification rate is low and planar interfaces are formed. The top surface of A1, A2 and A3 consists of fine columnar dendrites with occasional secondary arms. The melt pool core of A4 is composed of fine and equiaxed dendrites with secondary and occasional ternary branches (Fig. 1-h-l). These fine dendrites are surrounded with cellular dendrites and the latter is enveloped by the coarser and elongated columnar dendrites (Fig. 1l) caused by overlapping of adjacent melt pools when the overlapping areas are subjected to a double exposure to laser and, hence, a slow rate of solidification. From another hand, with an increase in scanning speed, the dwell time of the heat source at each point of the track decreases leading to increase in solidification rate.

Fig. 1m-n and Fig. 1q-r show the unpolished horizontal and vertical fracture surfaces of A2. The SEM images of horizontal fracture show fine (2–3 μm) and coarse (up to 10 μm) dendrites with branching distributed throughout Al rich phase. Vertical fracture images reinstate the presence of fine columnar dendrites in the core and coarse structures in overlapped regions (Fig. 1s).

EDS mapping of A2, Fig. 2, reveals Mo, Si and Al at the light-grey dendrites, while the black textures are the Al-rich phase (Fig. 2b). The XRD patterns, Fig. 2c, indicate the formation of hexagonal C40 $Mo_3(Si_4Al_2)$, which corresponds to $Mo(Si_{0.67}Al_{0.33})_2$ composition, along with face centered cubic $Al_{0.85}Si_{0.15}$ and silicon. The hexagonal C40 $Mo(Si,Al)_2$ phase is homogeneously nucleated and grown as the primary phase, and $Al_{0.85}Si_{0.15}$ is formed from Al-Si eutectic liquid.

Phase content analysis indicates 71.2% $Mo_3(Al_2Si_4)$, 19.9% $Al_{0.85}Si_{0.15}$ and 8.9%Si in A2; accordingly, the elemental composition is 45.2%Mo, 29.6%Si and 25.3%Al, which is in a good agreement with the composition of powder mixture. Despite the aluminum rich $Al_{0.85}Si_{0.15}$ phase is detected, the $Mo(Si_{1-x},Al_x)_2$ is formed with x = 0.33 mol although, according to the literature data, excess of aluminum *x* should attain up to 0.65 mol forming $MoAl_{1.3}Si_{0.7}$ [11,12] as localized heating and fast heating/cooling rates prevent further expansion of C40 lattice and form orthorhombic C54 aluminum-rich phase of a narrow range of homogeneity even at excess of aluminum. The theoretical density of the samples was calculated according to the rule of mixtures based on phase composition ($Mo_3(Al_2Si_4)$ (ρ = 6.09 g/cm^3), $Al_{0.85}Si_{0.15}$ (ρ = 2.71 g/cm^3) and Si (ρ = 2.33 g/cm^3)). As all samples have similar chemical composition, the theoretical density was calculated to be 4.37 g/cm^3. As Mo-Si-Al ternary compound is sensitive to the initial mixture, the stoichiometric Mo + 1.34Si + 0.66AlSi10Mg powder mixture was examined. The endothermic peak appeared at around 579 °C indicates Al-Si eutectic liquid phase formation (T_{start} = 570 °C). The intense exothermic interaction of Mo and Al-Si phase starts at 800 °C recording the largest heat flow at 869 °C (Fig. 2h). According to DSC, at the first stage, hypoeutectic AlSi10Mg and Si form Al-Si eutectic, then after start of an exothermic reaction with Mo, $Mo(Si, Al)_2$ is developed. During solidification, the precipitation of unreacted Si and $Al_{0.85}Si_{0.15}$ occurs, which serve as nucleation centers for $Mo(Si, Al)_2$. XRD analysis of DSC products detected 95.9% $Mo_3(Al_2Si_4)$ along with trace amount of 0.9%Mo, 1.9%$Al_{0.85}Si_{0.15}$ and 1.3%Mo_5Si_3 (ICDD card number 04-004-7607) manifesting that aluminum replaces silicon up to 0.66 mol (2x).

Fig. 3a shows the pore size and distribution in A2. The porosity level calculated by pore and part voxels is ~0.02% considering pores >40 μm size. Majority of the detected pores are in 40–50 μm range (Fig. 3d). The max frequency was observed for the pores with 0.3 aspect ratio indicating the existence of mostly elongated, non-spherical pores (Fig. 3c).

The samples possess relative density of 98–99% (corresponds to CT results), and the hardness values are in the range of 417-498 HV5 (Table 1), which is about 4 times higher than reported for SLM produced AlSi10Mg [10].

4. Conclusions

For the first time successful reactive laser powder-bed fusion through SLM of (Mo + 2Si) + 30 wt%AlSi10Mg mixture was performed achieving C40 hexagonal $Mo_3(Al_2Si_4)$ formation. Under chosen conditions (67.2–112.0 J/mm^3 ED) solubility limit of Al (x) in $Mo(Si_{1-x},Al_x)_2$ was 0.33 mol despite the excess amount of

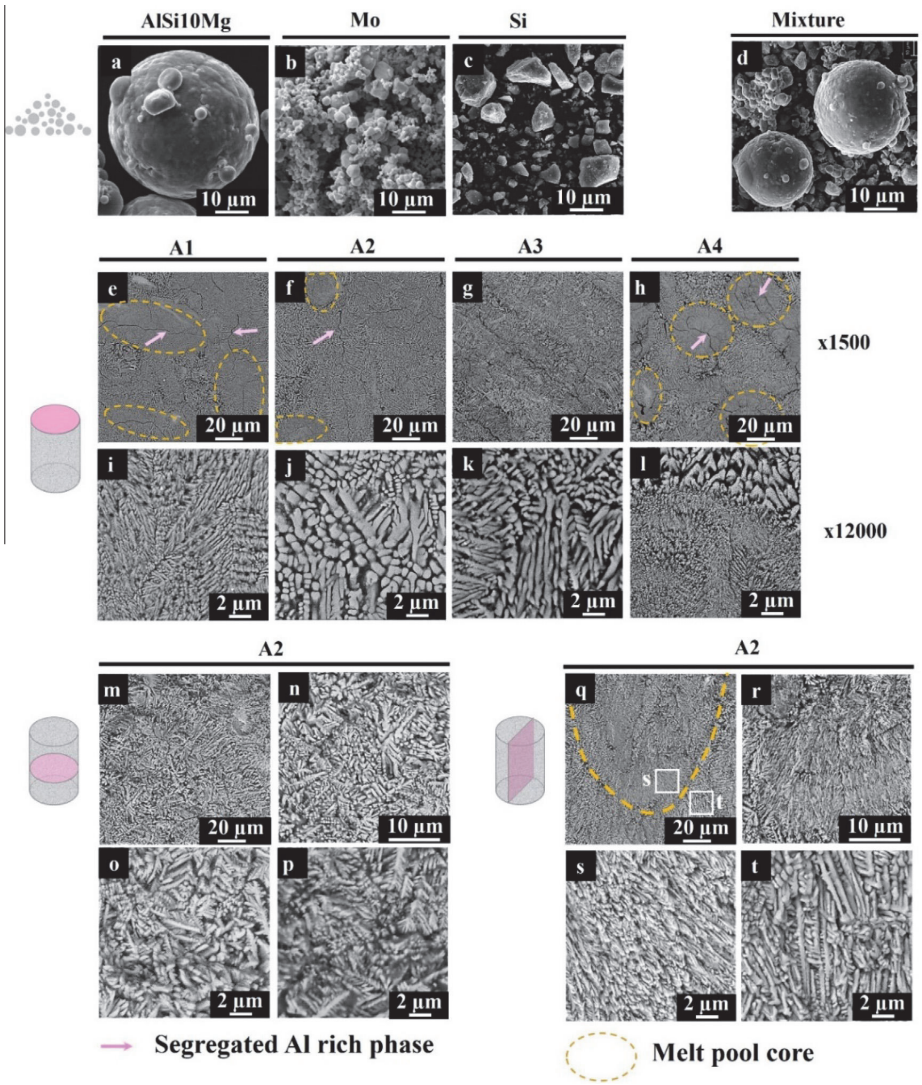

Fig. 1. SEM images of AlSi10Mg (a), Mo (b), Si (c), Mo + 2Si + 30wt.%AlSi10Mg mixture (d); and top surface SEM images of A1-A4 (e-l), unpolished top (m-p) and side fracture of A2 (q-t).

AlSi10Mg in initial powder mixture. Samples are composed of fine columnar dendrites and possess up to 99% relative density and ~500 HV5 hardness.

CRediT authorship contribution statement

T. Minasyan: Methodology, Formal analysis, Investigation, Writing - original draft. **S. Aydinyan:** Conceptualization, Software, Formal analysis, Resources, Data curation, Supervision, Funding acquisition. **L. Liu:** Methodology, Software, Investigation, Writing - original draft. **O. Volubujeva:** Investigation. **E. Toyserkani:** Resources, Writing - review & editing. **I. Hussainova:** Conceptualization, Software, Formal analysis, Resources, Data curation, Writing - review & editing, Supervision, Project administration, Funding acquisition.

Declaration of Competing Interest

The authors declare that they have no known competing financial interests or personal relationships that could have appeared to influence the work reported in this paper.

Acknowledgements

This work was supported by the Estonian Research Council under projects PSG220 and PRG643. T. Minasyan acknowledges

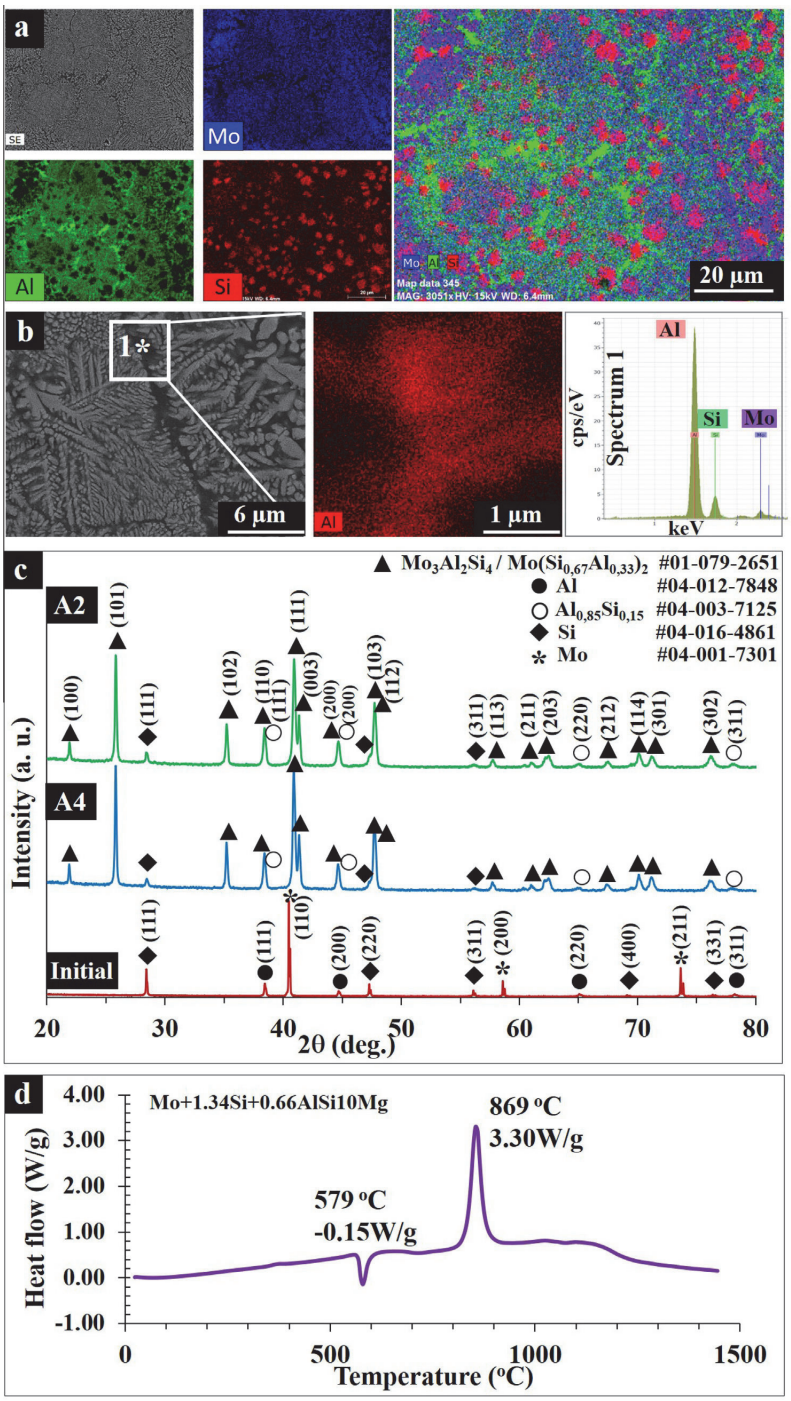

Fig. 2. EDS mapping of A2 (a); EDS of core area (b); top surface XRD patterns (f); and DSC of Mo + 1.34Si + 0.66AlSi10Mg mixture (d).

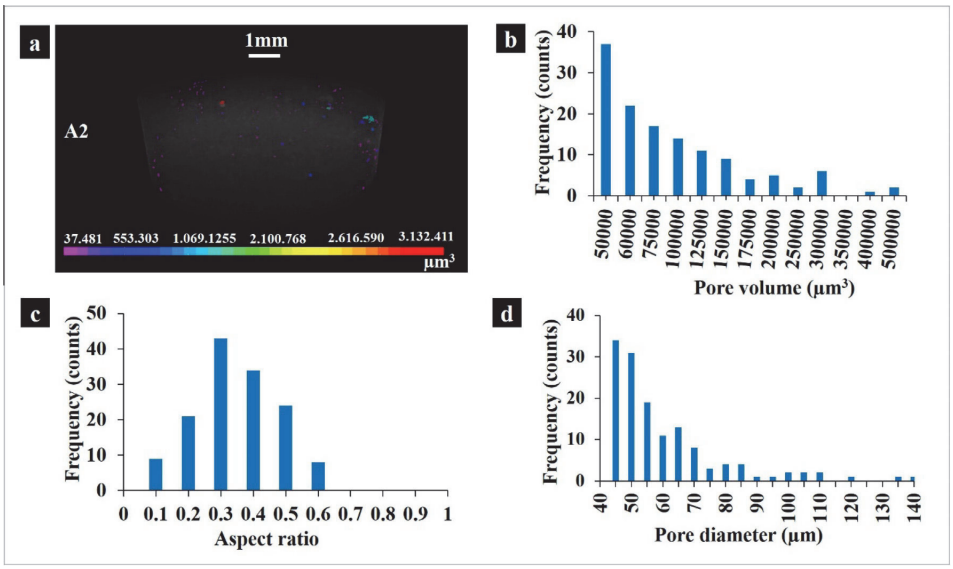

Fig. 3. 3D visualization of porosity in A2 (a); and CT: pore size distribution (b), aspect ratio of pores (c), calculated pore diameter (d).

Table 1
Density and hardness.

Sample ID	Energy density (J/mm^3)	Arch. Density (g·cm^{-3})	Relative Density (%)	Hardness HV5
A1	67.2	4.28	97.9	417 ± 11
A2	83.9	4.33	99.0	477 ± 20
A3	95.3	4.30	98.3	498 ± 17
A4	112.0	4.32	98.8	450 ± 15

the Archimedes foundation (DORA+). Authors thank Mr. Henry Ma, Mr. Rainer Traksmaa and Dr. Ehsan Marzbanrad for their help.

Appendix A. Supplementary data

Supplementary data to this article can be found online at https://doi.org/10.1016/j.matlet.2020.128776.

References

[1] A. K. Vasudevan, et al., A comparative overview of molybdenum disilicide composites, https://doi.org/10.1016/0921-5093(92)90308-N.
[2] A. Zehe et al, Migration-forced metal extrusion from molybdenum disilicide interconnects. https://doi.org/10.1016/S0167-577X(02)00698-5.
[3] P. Kang, et al., Phase formation during annealing powders of molybdenum disilicide, https://doi.org/10.1016/S0167-577X(03)00333-1.
[4] T. Maruyama, et al., High temperature oxidation and pesting of Mo(Si,Al)2. https://doi.org/10.1016/S0921-5093(97)00673-4.
[5] M. Sundberg, et al., Alumina forming HT silicides and carbides. https://doi.org/10.1016/j.ceramint.2003.12.046.
[6] N. Aboulkhair, et al., Reducing porosity in AlSi10Mg processed by SLM, https://doi.org/10.1016/j.addma.2014.08.001.
[7] C. Han, et al., Recent Advances on High-Entropy Alloys for 3D Printing. https://doi.org/10.1002/adma.201903855.
[8] T. Tabaru, et al., Effects of substitution of Al for Si on the lattice variations and thermal expansion of Mo(Si,Al)2. https://doi.org/10.1016/j.intermet.2003.07.002.
[9] K. Hagihara, et al., Successful AM of MoSi2 including crystallographic texture and shape control, https://doi.org/10.1016/j.jallcom.2016.11.191.
[10] L. Thijs, et al., Fine-structured aluminum products with controllable texture by SLM of AlSi10Mg powder, https://doi.org/10.1016/j.actamat.2012.11.052.
[11] A. Stergiou, et al., Study of the effects of Al, Ta, W additions on the microstructure and properties of MoSi2 alloys. https://doi.org/10.1557/PROC-364-91.
[12] M. E. Ghayoumabadi, et al., Lattice variations and phase evolutions during combustion reactions in Mo–Si–Al system. https://doi.org/10.1016/j.jallcom.2008.04.033.

Paper IV

Minasyan, T., Aydinyan, S., Toyserkani, E., & Hussainova, I. (2020). In situ $Mo(Si,Al)_2$-based composite through selective laser melting of a $MoSi_2$-30 wt.% AlSi10Mg mixture. *Materials*, 13(17), 3720.

materials

MDPI

Article

In Situ $Mo(Si,Al)_2$-Based Composite through Selective Laser Melting of a $MoSi_2$-30 wt.% AlSi10Mg Mixture

Tatevik Minasyan [1,2,*], Sofiya Aydinyan [1], Ehsan Toyserkani [2] and Irina Hussainova [1,*]

[1] Department of Mechanical and Industrial Engineering, Tallinn University of Technology, Ehitajate 5, 19086 Tallinn, Estonia; sofiya.aydinyan@taltech.ee

[2] Multi-Scale Additive Manufacturing Laboratory, Department of Mechanical and Mechatronics Engineering, University of Waterloo, 200 University Ave., West Waterloo, ON N2L 3G1, Canada; ehsan.toyserkani@uwaterloo.ca

* Correspondence: tatevik.minasyan@taltech.ee (T.M.); irina.hussainova@taltech.ee (I.H.)

Received: 2 August 2020; Accepted: 19 August 2020; Published: 23 August 2020

Abstract: The laser power bed fusion approach has been successfully employed to manufacture $Mo(Si,Al)_2$-based composites through the selective laser melting of a $MoSi_2$-30 wt.% AlSi10Mg mixture for high-temperature structural applications. Composites were manufactured by leveraging the in situ reaction of the components during printing at 150–300 W laser power, 500–1000 mm·s^{-1} laser scanning speed, and 100–134 J·mm^{-3} volumetric energy density. Microcomputed tomography scans indicated a negligible induced porosity throughout the specimens. The fully dense $Mo(Si_{1-x},Al_x)_2$-based composites, with hardness exceeding 545 HV1 and low roughness for both the top (horizontal) and side (vertical) surfaces, demonstrated that laser-based additive manufacturing can be exploited to create unique structures containing hexagonal $Mo(Si_{0.67}Al_{0.33})_2$.

Keywords: selective laser melting; molybdenum disilicide; composite; aluminum alloy; computed tomography; surface roughness

1. Introduction

Molybdenum disilicide $MoSi_2$ is regarded as a promising material for a wide variety of industrial applications due to its combination of outstanding properties, such as its high melting point (2293 K), moderate density (6.24 g·cm^{-3}), excellent intermediate- and high-temperature oxidation resistance, and metallic-like high electrical and thermal conductivity [1]. Exploitation of these properties opens up the prospect for the development of composites with tailored mechanical and physical behaviours. Aluminum is one of the most favorable alloying additions for $MoSi_2$, which may enhance the high-temperature oxidation resistance, fracture toughness, creep resistance, and low-temperature ductility of $MoSi_2$, along with introducing a more metallic character to the compound [2].

The main processing routes explored so far for preparation of $Mo(Si,Al)_2$ are arc melting [3–6], self-propagating high-temperature synthesis (SHS) [7–10], hot pressing [11], spark plasma sintering (SPS) [12], and some others [13], as specified in Table 1.

Table 1. Methods of $Mo(Si,Al)_2$ fabrication.

Initial Reagents	Preparation Technique	Final Product	Important Notes	Refs.
Mo + 2(1 − x)Si + 2xAl x = 0.14; 0.15; 0.28; 0.37	Arc melting of plates of the constituent elements Mo, Si, and Al in argon.	$Mo(Si_{1-x},Al_x)_2$ (0.11 < x < 0.55) x = 0.14; 0.15; 0.28; 0.37	The substitution of Si with Al gives $Mo(Si_{1-x},Al_x)_2$ of the C40 structure with a large homogeneity in the range of 0.11 < x < 0.55	[3]
33.3 at.% Mo + 44.2 at.% Si + 22.5 at.% Al	Arc melting	C40 $Mo(Al_{0.5},Si_{0.5})_2$ and C54 $MoAl_{1.3}Si_{0.7}$ phases	Addition of Al as a substitution for Si leads to formation of the higher symmetry C40 and C54 phases	[4]
Mo + 2(1 − x)Si + 2xAl x = 0.0075–0.225	Arc melting	$Mo(Si_{0.9925}Al_{0.0075})_2$ $Mo(Si_{0.985}Al_{0.015})_2$ $Mo(Si_{0.925}Al_{0.075})_2$ $Mo(Si_{0.85}Al_{0.15})_2$ $Mo(Si_{0.775}Al_{0.225})_2$	Al is soluble in $MoSi_2$ up to about x = 0.045. The excess of Al resulted in formation of the C40- or C49-type phases	[5]
Mo + 2Si + (1–2.5 at.%)Al	Arc melting	$Mo(Al, Si)_2$ Al-(1–2.5 at.%)	The addition of 2 at.% Al increased the high-temperature strength of $Mo(Al, Si)_2$, lowered the brittle to ductile transition temperature, and decreased the hardness	[6]
Mo + 2(1 − x)Si + 2xAl x = 0.01–0.5	Self-propagating high-temperature synthesis (SHS) + hot pressing	$Mo(Al_{0.5},Si_{0.5})_2$ $Mo(Al_{0.2},Si_{0.8})_2$ $Mo(Al_{0.05},Si_{0.95})_2$ $Mo(Al_{0.01},Si_{0.99})_2$	The substitution of 10 wt.% Al for Si yielded equal amounts of $Mo(Al,Si)_2$ and $MoSi_2$	[7]
Mo-2Si-0.04PTFE-0.88Al Mo-2Si-0.08PTFE-0.88Al	SHS	$MoSi_2$, Al, Mo_5Si_3, AlF_3 in $MoSi_2$-Al cermet foam	Porous product	[8]
Mo + 2(1 − x) + 2x x = 0–0.5	SHS + induction plasma spheroidization (IPS)	$Mo(Si_{1-x},Al_x)_2$ (x = 0–0.5) x = 0 → nearly pure C11b $MoSi_2$ x = 0.1 → C11b C40 0.2 ≤ x ≤ 0.4 → C40 + C11b (trace) x = 0.1 → C40 + C54	$Mo(Si,Al)_2$ with C40 structure designed as $Mo(Si_{0.6},Al_{0.4})_2$ with the maximum Al content in SHS. After IPS, the apparent density was remarkable improved	[9]
Mo + 2(1 − x)Si + 2xAl x = 0.0–0.5 mole (0 to 17.86 wt.% Al)	SHS	$Mo(Si_{1-x},Al_x)_2$ x = 0.08 → C11b $MoSi_2$ + C40 x = 0.2 → nearly pure C40 x = 0.5 → C40 + C54	Up to 2.84 wt.% Al, only C11b's tetragonal phase is present; up to 5.33 wt.% Al, a duplex of C11b/C40 phases is present. Increasing the Al reduces the amount of C11b in the biphasic region. A single C40 hexagonal forms at 7.11 wt.% Al. At 17.86 wt.% Al, orthorhombic C54 ($Al_4Mo_3Si_2$) appears	[10]
Mo + 2(1 − x) + 2x x = 0–0.6	Pseudo-HIP	$Mo(Si_{1-x},Al_x)_2$ x = 0 → C11b x = 0.1 → C11b + C40 x = 0.2–0.4 → C40 x = 0.5 → C40 + C54 x = 0.6 → C54	C40 is in the range of x = 0.1–0.5, while C11b is detected at x = 0.1 and C54 at x = 0.5. C11b is identified only atx = 0, while only C54 is detected at x = 0.6	[11]
SHS-ed powders $Mo_{1-x}Nb_x)Si_2$ (x = 0–0.3), $Mo(Si_{1-y},Al_y)_2$ (y = 0–0.3)	SPS at 1350 °C and 40 MPa for 6 min in vacuum	$(Mo_{1-x}Nb_x)Si_2$ $Mo(Si_{1-y},Al_y)_2$	Addition of Nb at x = 0–0.12 increased the strength and toughness	[12]
Mo plate and molten Al saturated with Si and Mo	Dipping Mo into Al-Si bath at 973 K for 350 ks	Mo plate covered with the layer of $Mo(Si,Al)_2$ of Mo:Si:Al = 30:12:58	The needle-like grains grow perpendicular to Mo's surface. The reaction goes through the solution–precipitation process in the Al(Si) liquid between Mo and $Mo(Si,Al)_2$ layers	[13]

Different Si/Al ratios in $Mo(Si_{1-x},Al_x)_2$ yield the formation and development of C40 hexagonal and C54 orthorhombic structures. The duplex C40/C54 phases appear when x = 0.5, while monophasic C54, often designated as $Mo_{10}Si_7Al_{13}$, is established at x = 0.6, as described in [11]. In [9], a similar trend of C54 phase formation was reported. It was also found that at 17.86 wt.% Al addition, the C54 phase with an $Al_4Mo_3Si_2$ composition is developed [10]. A higher percentage of Al does not promote the development of monophasic C54, since the segregation of Mo suppresses the combustion synthesis. The formation of C40 $Mo(Al_{0.5},Si_{0.5})_2$ and the orthorhombic C54 $MoAl_{1.3}Si_{0.7}$, as a result of the arc-melted mixture of 33.3 at.% Mo, 44.2 at.% Si, and 22.5 at.% Al, is reported in [4]. The Al-rich side of the $Mo(Si,Al)_2$ composition ends at the Al_8Mo_3 phase, as described in [14].

The main difficulties associated with the processing of $MoSi_2$-AlSi10Mg composites are the restrictive stoichiometry limits, high melting point, and low-temperature brittleness. Application of additive manufacturing (AM) techniques for the $MoSi_2$-Al system has not been explored yet. AM through selective laser melting (SLM) provides a wide range of new opportunities for the processing and fabrication of various products with complex constitutional designs and shapes, which are impossible to achieve via any conventional method.

In this paper, an attempt is made to produce $Mo(Si,Al)_2$-based composites in situ, exploiting the laser power bed fusion of $MoSi_2$ and AlSi10Mg alloy powders and taking into consideration the successful SLM of $MoSi_2$ [15,16] and AlSi10Mg [17]. In this context, we demonstrate for the first time the reactive selective laser melting of $MoSi_2$-30 wt.% AlSi10Mg, which results in fully dense bulks of good quality. This paper discusses the material structure and hardness; however, the high-temperature mechanical properties and oxidation are out of this paper's scope.

2. Experiments

2.1. Powder Preparation and Characterization

For SLM feedstock preparation, combustion-synthesized $MoSi_2$ powder (99% purity) was mixed with 30 wt.% gas-atomized AlSi10Mg (SLM, Solutions, purity >99%, 15–63 μm) for 3 h using mechanical rotation (20 rpm). The particle size and sphericity analyses of the $MoSi_2$, AlSi10Mg, and $MoSi_2$-30 wt.% AlSi10Mg powders were carried out in a CAMSIZER X2 device (MICROTRAC MRB, Haan, Germany), adopting dynamic image analysis (ISO 13322-2 [18]) as the measuring principle using 10 mL of powder. Sphericity is determined as the square of the circularity of a powder particle using the $4\sqrt{A}\cdot P^{-2}$ equation, where P is the measured perimeter of the particle and A is the computed area from the particle projection. The FT4 Powder Rheometer (Freeman Technology, Tewkesbury, UK) was used to determine the basic flowability energy (BFE) of powders and mixture. To define the resistance of a powder to flow, 8 test cycles were run. During each test, the precision blade rotated downwards (at a speed of −100 mm·s^{-1}) and upwards through the fixed volume of powder to create a flow pattern. The BFE is calculated with the following equation: $BFE = E_{test8}$, where E_{test8} is the energy recorded during downward rotation of the blade for the 8th test. The stability index (SI) is calculated as follows: $SI = E_{test8}/E_{test1.}$ The packing density of the mixture was measured by GranuPack (GranuTools, Awans, Belgium). The actual value for the average bulk density at the end of the trials (ρ[n]) was measured and the bulk density value for ρ[∞] was extrapolated.

Differential scanning calorimetry (DSC) analysis was performed to analyze the thermal behavior of $MoSi_2$-30 wt.% AlSi10Mg powder (70 mg) using a NETZSCH-STA 449 F1 Jupiter (NETZSCH-Gerätebau GmbH, Selb, Germany) thermal analyzer from 25 °C to 1450 °C, with a heating rate of 20 °C·min^{-1} in an argon atmosphere.

2.2. Selective Laser Melting

Consolidation of the $MoSi_2$-30 wt.% AlSi10Mg mixture by selective laser melting (SLM) was carried out using a Renishaw AM400 apparatus (Wotton-under-Edge, Gloucestershire, UK), which employs a high-power, continuous-wave, and a laser, modulated to work as a pulse laser. The device is equipped with an Ytterbium laser with a maximum power of 400 W and a wavelength of 1.07μm. Cylindrical samples with dimensions of Ø7 mm × 7 mm were built. The meander scan strategy was used, whereby scan patterns rotate by 67° after each printed layer. The whole manufacturing process was carried out inside a chamber containing a precisely controlled atmosphere of argon at an oxygen level below 500 ppm. The hatching distance (h) and laser spot size were set as 85 μm and 90 μm, respectively. The laser power (P) was in the range of 150–300 W and the scanning speed (ν) was in the range of in 500–1000 mm·s^{-1} range. The layer thickness (d) was chosen as 35 μm. The process parameters for preparation of the three samples are listed in Table 2.

Table 2. Process parameters for samples S1–S3.

Sample ID	Laser Power (W)	Scanning Speed ($mm \cdot s^{-1}$)	Laser Volumetric Energy Density ($J \cdot mm^{-3}$)	Build Rate ($mm^3 \cdot s^{-1}$)
S1	150	500	100.8	1.48
S2	200	500	134.4	1.48
S3	300	1000	100.8	2.97

The laser volumetric energy density (LED) and build rate were calculated according to E = P/vhd and BR = *vhd*, respectively.

2.3. Bulk Characterization

The density of printed parts was measured by Archimedes' principle (Mettler Toledo ME204, Greifensee, Switzerland) and by calculating the dimensions (digital Vernier caliper of 0.01 mm accuracy, Digital Caliper, KS Tools Werkzeuge-Maschinen GmbH, Heusenstamm, Germany) and weight (Eltra 84 analytical balance, 0.1 mg accuracy, Haan, Germany) of the samples. The size, morphology, and alignment of the pores in the SLM-fabricated samples were inspected via X-ray computed tomography (CT) (ZEISS Xradia 520 Versa 3D X-ray microscope Oberkochen, Germany). The surface roughness analysis was performed using a Keyence VK-X250 profile analyzing confocal laser microscope (Keyence Corporation, Osaka, Japan). On each studied surface, 4 areas with dimensions of 500 μm × 700 μm were scanned using a 20× lens. The maximum height (Sz) and arithmetical mean height (Sa) were averaged for 4 measurements.

Samples were ground and polished by conventional metallographic methods to a 0.5 μm diamond polish and to a finer 0.1 μm finish using a nylon disc and polishing suspension. The morphology and microstructure of the powders and printed bulks were examined by TESCAN VEGA3 (Brno, Czech Republic) and HR-SEM Zeiss Merlin scanning electron microscope (SEM, ZEISS, Oberkochen, Germany) equipped with an EDS detector (Bruker EDX-XFlash6/30, Billerica, MA, USA). Phase compositions were analyzed with the help of an X-ray diffractometer (Siemens/Bruker D5000 X-ray Powder Diffraction (XRD) System, Billerica, MA, USA) with CuKα radiation in the 2θ range of 20° to 80°. The concentrations of compounds and elements were estimated via the Rietveld refinement method. The Vickers hardness values were measured on the polished surfaces of the printed specimens using a tester (Indentec 5030 SKV, Stourbridge, West Midlands, UK) at a load of 9.8 N, applied over 10 s for 10 indents.

3. Results and Discussion

3.1. Powders

Powder flowability is one of the most influencing parameters affecting the powder bed density, and therefore affecting the produced item quality, including the density and roughness. [15,17]. The powder particle shape, size, and distribution are of primary importance for sintering kinetics and powder bed formation [17,19]. The SEM image of the gas-atomized AlSi10Mg alloy powder is shown in Figure 1a. As shown in Table 3, the median diameter (D50) of AlSi10Mg was evaluated as ~40 μm. The powder of $MoSi_2$ consists of agglomerates of fine (1–5 μm) particles (Figure 1b), with D50 < 19 μm (Table 3). The SEM image of the $MoSi_2$-30 wt.% AlSi10Mg powder mixture clearly demonstrates an apparent particle size difference between constituents. Fine $MoSi_2$ particles can serve as nucleation centers during cooling and provide homogeneous solidification after laser scanning.

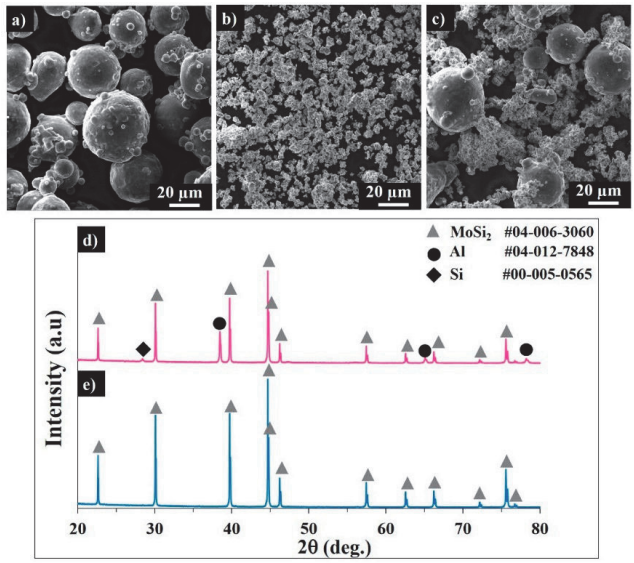

Figure 1. SEM images of the AlSi10Mg alloy (**a**) $MoSi_2$ and (**b**) $MoSi_2$-30 wt.% AlSi10Mg powder mixture (**c**). Corresponding XRD patterns of the $MoSi_2$-30 wt.% AlSi10Mg (**d**) and $MoSi_2$ (**e**) powders.

Table 3. Size distributions of the AlSi10Mg, $MoSi_2$, and $MoSi_2$-30 wt.% AlSi10Mg powders.

Particle Size / Composition	D10 (μm)	D50 (μm)	D90 (μm)
AlSiMg10	25.14 ± 0.53	38.72 ± 0.67	55.47 ± 0.44
$MoSi_2$	5.44 ± 0.26	18.95 ± 0.89	43.45 ± 0.65
$MoSi_2$-30 wt.% AlSi10Mg	7.68 ± 0.07	33.02 ± 1.18	54.19 ± 1.30

Usually, the spherical particles of narrow size distribution exhibit better flowability compared to the angularly shaped powders. The sphericity of the $MoSi_2$-30 wt.% AlSi10Mg mixture gradually decreased from ~0.9 to 0.79 in a particle size range of 3–55 μm, conditioned by the non-spherical shape of the $MoSi_2$ agglomerates.

The basic flowability energy values of AlSi10Mg, $MoSi_2$-30 wt.% AlSi10Mg, and $MoSi_2$ were not significantly different, being ~206, 252, and 307 mJ, respectively (Table 4). Therefore, the flowability of the mixture can be considered as fair and applicable for SLM processing.

Table 4. Average flow rate for the $MoSi_2$, $MoSi_2$-30 wt.% AlSi10Mg, and AlSi10Mg alloy powders.

Powders / FT4 Results	$MoSi_2$ (<45 μm)	$MoSi_2$-30 wt.% AlSi10Mg	AlSi10Mg (15–63 μm)
BFE, mJ	307.52 ± 13.74	252.27 ± 19.41	206.14 ± 8.92
SI	1.09999 ± 0.00606	0.95012 ±0.07664	0.96271 ± 0.06536

The bulk density of the powders is another important characteristic when choosing the powder feedstock for SLM. Figure 2 shows the packing density of the $MoSi_2$-30 wt.% AlSi10Mg powder mixture. The initial bulk density of the powder was 1.76 ± 0.012g·mL^{-1}; after 2000 taps, the bulk density increased up to 2.45 ± 0.048 g·mL^{-1} and the packing density was extrapolated to be 2.62 ± 0.064 g·mL^{-1}.

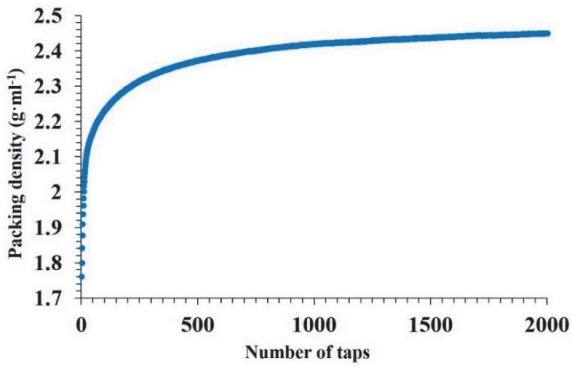

Figure 2. Average packing density of the $MoSi_2$-30 wt.% AlSi10Mg powder as a function of stress.

Small particles of $MoSi_2$ can fill voids between the large particles of AlSi10Mg and increase the packing density.

3.2. Bulks

Figure 3 demonstrates the 3D visualization of porosity in samples S1–S3. The porosity level calculated by part and pore voxels is less than 1% when supposing that the relative density of the bulks is ≥99%. Figure 4 displays X-ray CT analysis of the pore distribution and its aspect ratio. The samples S1 and S3 are printed with the same applied energy density (100.8 J·mm^{-3}), but at different scanning speeds and laser powers. The sample S3 possesses the lowest number of pores (Figures 3c and 4), pointing to the effect of the laser power on the decreased porosity; however, further SEM analyses revealed the susceptibility to cracking of the materials printed with a high laser power (300 W). For samples S1 and S2, the maximum frequency was observed for the pores with an aspect ratio of 0.4, while for S3 most of the pores had an aspect ratio of 0.5 (Figure 4c). For all three samples, the majority of the pores measured were of 30 – 35 µm. The relative geometric and Archimedes density results coincided with the CT scanning results (Figure 4d).

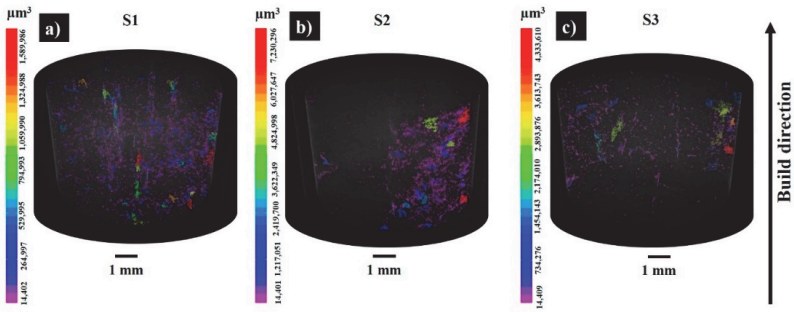

Figure 3. The 3D visualization of the porosity results in as-built samples S1 (**a**), S2 (**b**), and S3(**c**) (pores are labelled by volume (µm^3)).

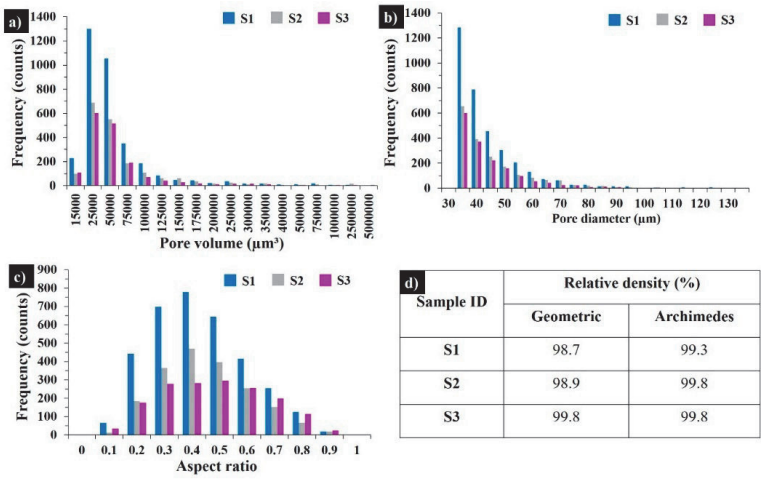

Figure 4. X-ray CT results in as-built samples S1, S2, and S3: pore size distributions (**a**), pore diameter distributions (**b**), aspect ratios of the pores (**c**), and relative geometric and Archimedes density results (**d**).

The average surface roughness (Sa) and the maximum height (Sz) of the top and side surfaces of the printed samples are listed in Table 5. A two-fold increase in the scanning speed results in a moderate increase in Sa and a dramatic increase in the maximum heights of irregularities for both top and side (vertical) surfaces. S2 produced the highest LED value but a moderate scan speed and possessed the smoothest top surface, which was conditioned by sufficient melting and sintering of the consecutive powder layers. The quality of the side surfaces was slightly inferior compared to the top surface. Particles on the sides were primarily formed by the partial melting at the build surface. For S3, a high applied LED value combined with a high build rate resulted in adhesion of the powder particles from the heat-affected zones onto the side surface of the piece, resulting in high surface roughness. The partially sintered particles detected on the top surface might be due to the blowing of metal particles into the laser-melted zones by the gas flow in the build chamber or from the powder bed due to vibration movement of the wiper during processing. Moreover, aluminum oxide can be formed due to oxidation of AlSi10Mg by the trace oxygen in the inert gas or by the inherent alumina layer on the powder surface. According to the EDS analysis, the adhered particles were examined and determined to be aluminum oxide (Figure 5, Spectrum 1).

Table 5. The roughness of the top and side surfaces of the printed samples.

Sample	Top Surface Roughness, µm		Side Surface Roughness, µm	
	Sa	Sz	Sa	Sz
S1	10.1	94.4	11.2	109.5
S2	9.9	75.5	13.2	130.8
S3	14.7	130.2	17.8	173.5

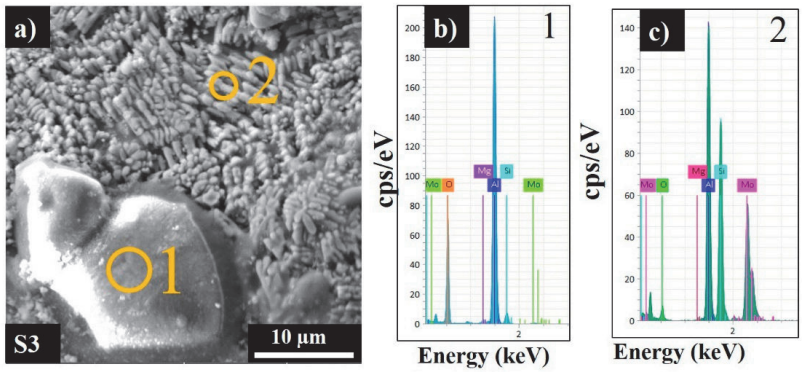

d) Elements / Spectrums	Mo (wt.%)	Si (wt.%)	Al (wt.%)	O (wt.%)	Mg (wt.%)
1	0.69	3.08	55.35	40.47	0.41
2	44.71	24.06	27.14	3.92	0.18

Figure 5. Side surface SEM image (**a**), EDS spectra (**b**,**c**), and corresponding elemental analysis results for sample S3 (**d**).

Spectrum 2 (Figure 5c) shows that the chosen section was composed of 44.71 wt.% Mo 24.06 wt.% Si and 27.14 wt.% Al, along with 3.92 wt.% oxygen.

3.3. Microstructural Analysis

The SEM images of the polished top surfaces of samples S1, S2, and S3 are depicted in Figure 6. The marked elliptical regions in Figure 6a–c demonstrate the core of the melt pools. The solidification process affects the crystallization in different regions due to various temperature gradients and heat flux directions, depending on the laser power and scanning speed. The melt pool dimensions depend on the applied laser power, LED, and temperature. There was a larger heat flux in the center of the melt pool due to Gaussian intensity of the single mode laser beam; hence, the surface tension varied between the center and outer edges, resulting in multifarious microstructures along the sample. Importantly, controlling the volume of the melt by increasing the scan speed was demonstrated to reduce the overlap and cause insufficient melting (Figure 6c).

The cores consisted of fine submicron- to micron-sized grains (Figure 6d–f), while at the border of each elliptical section, the coarser columnar dendrites were observed (Figure 6d,e). This phenomenon is caused by the cooling rate and temperature difference in the center of the melt pool and at the border, as the melt pool periphery is exposed to a longer laser exposure during overlapping of adjacent scan tracks. From the microstructure of S3 produced at the scan speed of 1000mm·s^{-1} (Figure 6c), a higher inhomogeneity of the morphological texture was detected as compared to samples S1 and S2. The bright regions in Figure 6 represent sintered $MoSi_2$, while the dark grey regions represent the segregated Al-rich phase that developed due to the incomplete reaction between $MoSi_2$ and Al at high scanning speeds. The light grey phase characterizes the Mo-Si-Al phase (which according to further XRD analysis was found to be the $Mo_3(Al_2Si_4)$ phase). A high scanning speed decreases the interaction time between a laser and a material, thus decreasing the solidification time and inducing a high temperature gradient [20]; therefore, a higher cooling rate at the interface results in a finer microstructure, as seen from Figure 6f.

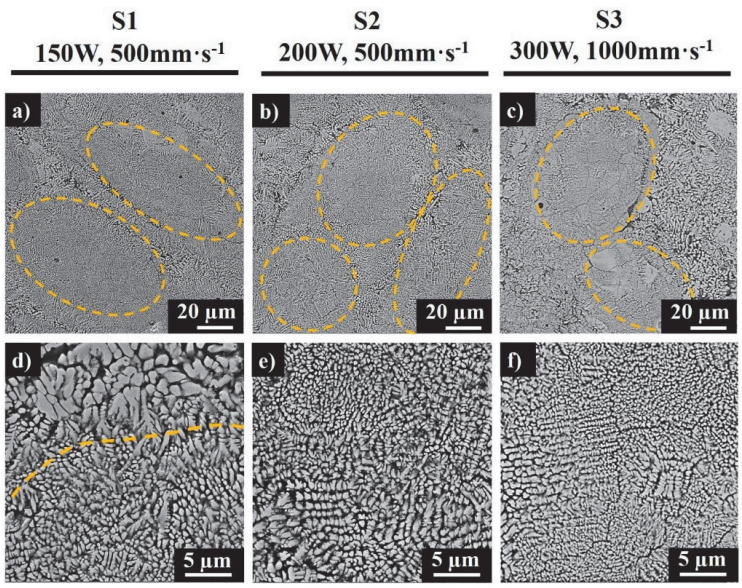

Figure 6. SEM images of polished top surfaces of samples S1 (**a**,**d**), S2 (**b**,**e**), and S3 (**c**,**f**).

Figure 7 demonstrates the backscattered electron (BSE) and secondary electron (SE) images of S2, along with corresponding elemental and mixed EDS maps.

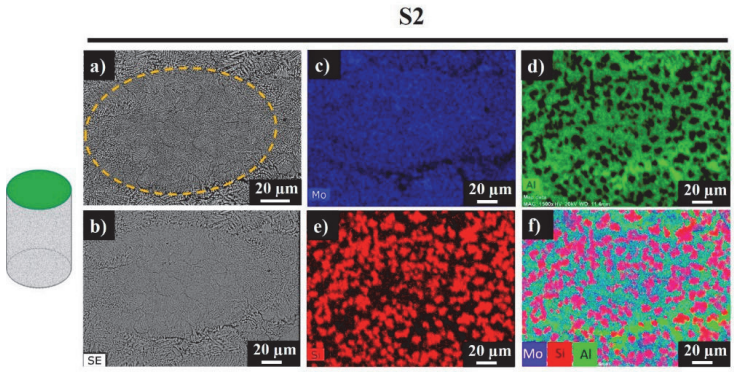

Figure 7. Top surface backscattered electron (BSE) image (**a**), secondary electron (SE) image (**b**), and EDS mapping results (**c**–**f**) for sample S2.

Signals of Mo were recorded everywhere expect the darkest regions, which correspond to the Al-rich phase (Figure 7d, bright green regions). Silicon was also observed in the studied area, while the bright red sections revealed the existence of replaced free Si, where no Al was detected. Accordingly, the sample was composed of Mo-Si-Al-, Al-, Al-, and Si-rich phases. Figure 8 shows the polished side fracture of sample S2 and the corresponding EDS maps. The yellow dashed regions (Figure 8a,b) represent the melt pools. The core of the melt pool was composed of fine elongated columnar dendrites with secondary arms grown parallel to the build direction, whereas the edges consisted of the coarser columnar dendrites (marked with white arrows) with occasional secondary branching due to overlap with the neighboring melt pools (Figure 8b).

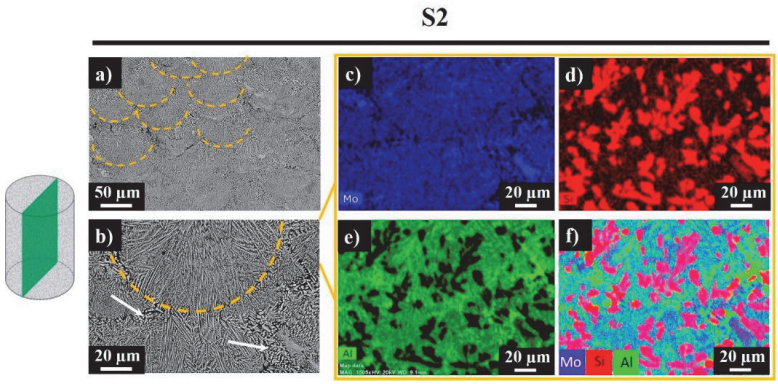

Figure 8. Top surface SEM images (**a**,**b**) and EDS mapping results for sample S2 (**c**–**f**).

The EDS maps corresponding to the SEM image in Figure 8b reveal a similar composition as for the top surface of the sample. Most of the studied area was composed of the Mo-Si-Al-containing phase. The dark regions in Figure 8b reveal the absence of Mo and the presence of the Al-rich phase. The black regions in the Al green map and the bright red regions in the Si map disclose the partial substitution of Si by Al.

Figure 9 displays the XRD patterns and Table 6 shows the phases and elemental compositions of the samples according to the Rietveld refinement method.

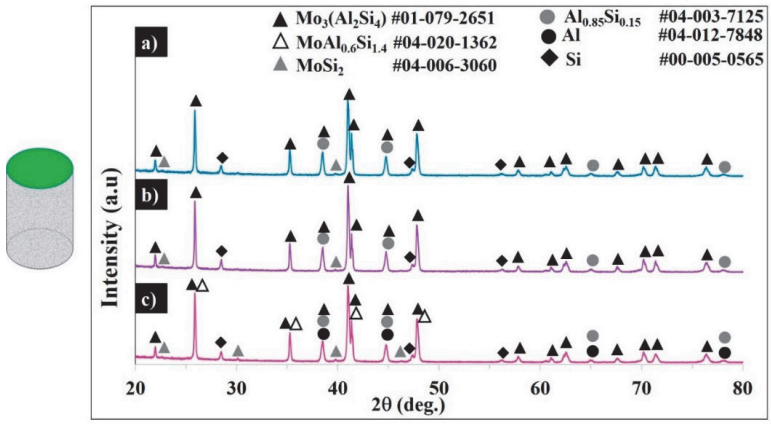

Figure 9. XRD patterns of samples S1 (**a**), S2 (**b**), and S3 (**c**).

Table 6. Compositions of the samples estimated from XRD patterns via the Rietveld refinement method.

Sample ID	Composition (%)					Elemental Composition (%)		
	$Mo_3(Si_4Al_2)$	$MoAl_{0.6}Si_{1.4}$	$MoSi_2$	$Al_{0.85}Si_{0.15}$	Al	Si	Mo	Si	Al
S1	69.4	0.5	1.2	19.7	0.0	9.1	45.1	30.0	24.9
S2	70.9	0.7	1.1	17.5	0.0	9.7	46.1	30.6	23.3
S3	67.0	3.7	2.4	17.0	1.2	8.7	46.3	29.8	23.9

The diffractograms of sample S3 confirm the presence of tetragonal $MoSi_2$, face-centered cubic Al, the substituted face-centered Si, the coexistence of the in-situ-formed hexagonal $Mo_3(Al_2Si_4)/MoAl_{0.6}Si_{1.4}$ phases (corresponds to $Mo(Si_{1-x},Al_x)_2$, x = 0.3–0.33) composition), and the Si-saturated Al-rich $Al_{0.85}Si_{0.15}$ phase.

The patterns for samples S1 and S2 evidenced the complete transformation of $MoSi_2$ to C40 $Mo_3(Al_2Si_4)$, with weak peaks of unreacted C11b, negligible $MoAl_{0.6}SiSi_{1.4}$, and with $Al_{0.85}Si_{0.15}$ being formed. For the applied high scanning speed, apparently the unreacted $MoSi_2$ and face-centered Al were found in the final product. In samples S1 and S2, no pure Al was detected, but the Si-saturated Al-rich $Al_{0.85}Si_{0.15}$ phase was detected. Under the chosen conditions (100.8–134.4 J·mm^{-3} ED) and with the addition of 30 wt.% AlSi10Mg to the $MoSi_2$, the C11b tetragonal lattice of $MoSi_2$ expanded until achieving a hexagonal $Mo(Si_{0.67}Al_{0.33})_2$ (x = 0.33 mol) structure, while no further C40 lattice expansion was detected in forming the Al-rich orthorhombic C54 structure. In contrast, the formation of C54 orthorhombic structures with $Mo_{10}Si_7Al_{13}$, $MoAl_{1.3}Si_{0.7}$, and $Al_4Mo_3Si_2$ is claimed in [4,9–11]; the formation of the silicon lean Al_8Mo_3 phase is reported in [14].

To study the mechanism of the $MoSi_2$–AlSi10Mg interaction, the thermogravimetric analysis for $MoSi_2$-30 wt.% AlSi10Mg was performed. Figure 10a shows the DSC-TG curves of the $MoSi_2$-30 wt.% AlSi10Mg mixture heated up to 1450 °C. The DSC curves exhibit the endothermic peak of the reaction of the aluminum melting and the Al-Si eutectic phase formation, where the heat absorption recorded was 0.9575W·g^{-1}. The weak exothermic reaction was observed starting from 944 °C and the maximum heat flow was 0.2393 W·g^{-1} at 1019 °C.

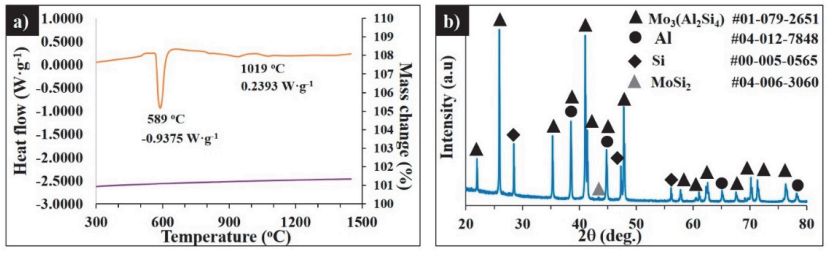

Figure 10. DSC-TG curves of $MoSi_2$-30 wt.% AlSi10Mg heated up to 1450 °C at 20°·min^{-1} in Ar (**a**) and the corresponding XRD pattern of the quenched sample (**b**).

No further chemical reactions were detected. According to the XRD patterns in Figure 10b, the sample contained 62.4% $Mo_3(Al_2Si_4)$, 0.7% $MoSi_2$, 12.4% Si, 3.3% $MoAl_{0.6}Si_{1.4}$, and 21.2% Al; however, the $Al_{0.85}Si_{0.15}$ phase was not detected.

The measured hardness of all SLM-processed materials was HV1 ~ 545 ± 48, which was around four times higher than for the printed AlSi10Mg alloy [21]. The high hardness is attributed to the significant effect of the $MoSi_2$ addition and the development of new phases during solidification.

4. Conclusions

Nowadays, there is huge interest in the development of new alloys for AM processes. The in situ SLM of mixed powders allows the production of hard materials with tailored properties, taking into consideration specific needs.

Fully dense $Mo(Si_{1-x},Al_x)_2$-based composites with hardness exceeding 500 HV1 were successfully SLM-processed at laser volumetric energy density values of 100.8 and 134.4 J·mm^{-3} and with scanning speeds of either 500 or 1000 mm s^{-1} from a $MoSi_2$-30 wt.% AlSi10Mg powder mixture. The bulks demonstrated relatively low roughness for both the top (horizontal) and side (vertical) surfaces, indicating the good quality of the produced parts.

Under the chosen conditions, with the addition of 30 wt.% AlSi10Mg to the $MoSi_2$, the C11b tetragonal lattice of $MoSi_2$ was expanded until achieving a hexagonal $Mo(Si_{0.67}Al_{0.33})_2$ (x = 0.33 mol) structure, while no further C40 lattice expansion was detected in forming the Al-rich orthorhombic C54 structure.

Author Contributions: Conceptualization, I.H. and S.A.; methodology, T.M., S.A., and E.T.; software, T.M.; validation, I.H., S.A., and E.T.; formal analysis, T.M.; investigation, T.M.; resources, I.H. and E.T.; data curation,

I.H.; writing—original draft preparation, T.M.; writing—review and editing, I.H., and S.A; visualization, T.M.; supervision, I.H. and S.A.; project administration, E.T. and I.H.; funding acquisition, I.H., and S.A. All authors have read and agreed to the published version of the manuscript.

Funding: This research was funded by the Estonian Research Council, grants PSG220 (S.A.) and PRG643. (I.H.).

Acknowledgments: This work was supported by the Estonian Research Council PSG220 (S.A.), PRG643 (I.H.). T.M. acknowledges the Archimedes foundation under the DORA + scholarship program for funding the travel visit to the University of Waterloo (Canada). The authors would like to thank also Rainer Traksmaa, Henry Ma and Ehsan Marzbanrad for their help with XRD, CT scanning, and DSC analyses.

Conflicts of Interest: The authors have no conflict of interest to declare.

References

1. Yao, Z.; Stiglich, J.; Sudarshan, T.S. Molybdenum silicide based materials and their properties. *J. Mater. Eng. Perform.* **1999**, *8*, 291–304. [CrossRef]
2. Vasudevan, A.K.; Petrovic, J.J. A comparative overview of molybdenum disilicide composites. *Mater. Sci. Eng. A* **1992**, *155*, 1–17. [CrossRef]
3. Maruyama, T.; Yanagihara, K. High temperature oxidation and pesting of Mo(Si,Al)2. *Mater. Sci. Eng. A* **1997**, *239*, 828–841. [CrossRef]
4. Stergiou, A.; Tsakiropoulos, P. Study of the effects of Al, Ta, W additions on the microstructure and properties of MoSi2 base alloys. *MRS Online Proc. Libr. Arch.* **1994**, *364*, 991. [CrossRef]
5. Harada, Y.; Murata, Y.; Morinaga, M. Solid solution softening and hardening in alloyed MoSi2. *Intermetallics* **1998**, *6*, 529–535. [CrossRef]
6. Sharif, A.A.; Misra, A.; Petrovic, J.J.; Mitchell, T.E. Alloying of MoSi2 for improved mechanical properties. *Intermetallics* **2001**, *9*, 869–873. [CrossRef]
7. Ramberg, C.E.; Worrell, W.L. Fabrication and High-Temperature Phase Stability of Mo (Al, Si) 2—MoSi2 Intermetallics. *J. Am. Ceram. Soc.* **2000**, *83*, 946–948. [CrossRef]
8. Hobosyan, M.A.; Khachatryan, H.L.; Davidova, A.; Kharatyan, S.L. Chemically activated combustion synthesis of MoSi2/Al cermet foams. *Chem. Eng. J.* **2011**, *170*, 286–291. [CrossRef]
9. Hou, H.D.; Ning, X.J.; Wang, Q.S.; Bin, G.A.O.; Liu, Y.B.; Ying, L.I.U. Preparation of Mo(Si,Al)2 feedstock used for air plasma spraying. *Trans. Nonferrous Met. Soc.* **2016**, *26*, 2939–2946. [CrossRef]
10. Ghayoumabadi, M.E.; Saidi, A.; Abbasi, M.H. Lattice variations and phase evolutions during combustion reactions in Mo–Si–Al system. *J. Alloys Compd.* **2009**, *472*, 84–90. [CrossRef]
11. Tabaru, T.; Shobu, K.; Sakamoto, M.; Hanada, S. Effects of substitution of Al for Si on the lattice variations and thermal expansion of Mo(Si,Al)2. *Intermetallics* **2004**, *12*, 33–41. [CrossRef]
12. Wang, X.H.; Wu, G.Z.; Lu, Q.; Sun, Z. Synthesis and mechanical properties of Nb and Al substituted MoSi2. *Mater. Res. Innov.* **2015**, *19* (Suppl. 4), S175–S180. [CrossRef]
13. Nanko, M.; Kitahara, A.; Ogura, T.; Kamata, H.; Maruyama, T. Formation of Mo(Si,Al)2 layer on Mo dipped in Al melt saturated with Si and the effects of transition metals added in the melt. *Intermetallics* **2001**, *9*, 637–646. [CrossRef]
14. Liu, Y.; Shao, G.; Tsakiropoulos, P. Thermodynamic reassessment of the Mo–Si and Al–Mo–Si systems. *Intermetallics* **2000**, *8*, 953–962. [CrossRef]
15. Minasyan, T.; Aghayan, M.; Liu, L.; Aydinyan, S.; Kollo, L.; Hussainova, I.; Rodríguez, M.A. Combustion synthesis of MoSi2 based composite and selective laser sintering thereof. *J. Eur. Ceram. Soc.* **2018**, *38*, 3814–3821. [CrossRef]
16. Minasyan, T.; Liu, L.; Holovenko, Y.; Aydinyan, S.; Hussainova, I. Additively manufactured mesostructured MoSi2-Si3N4 ceramic lattice. *Ceram. Int.* **2019**, *45*, 9926–9933. [CrossRef]
17. Read, N.; Wang, W.; Essa, K.; Attallah, M.M. Selective laser melting of AlSi10Mg alloy: Process optimisation and mechanical properties development. *Mater. Des.* **2015**, *65*, 417–424. [CrossRef]
18. ISO 13322-2. Particle Size Analysis—Image Analysis Methods—Part 2: Dynamic Image Analysis Methods. International Organization for Standardization: Geneva, Switzerland, 2006.
19. Aboulkhair, N.T.; Everitt, N.M.; Ashcroft, I.; Tuck, C. Reducing porosity in AlSi10Mg parts processed by selective laser melting. *Addit. Manuf.* **2014**, *1*, 77–86. [CrossRef]

20. Zhang, J.; Song, B.; Wei, Q.; Bourell, D.; Shi, Y. A review of selective laser melting of aluminum alloys: Processing, microstructure, property and developing trends. *J. Mater. Sci. Technol.* **2019**, *35*, 270–284. [CrossRef]
21. Liu, B.; Li, B.Q.; Li, Z. Selective laser remelting of an additive layer manufacturing process on AlSi10Mg. *Results Phys.* **2019**, *12*, 982–988. [CrossRef]

Paper V

Minasyan, T., Aydinyan, S., Toyserkani, E., & Hussainova, I. (2020) Parametric study on in-situ laser powder-bed fusion of $Mo(Si_{1-x},Al_x)_2$. *Materials,* 13(21), 4849.

materials

MDPI

Article

Parametric Study on In Situ Laser Powder Bed Fusion of $Mo(Si_{1-x},Al_x)_2$

T. Minasyan [1,2,*], S. Aydinyan [1], E. Toyserkani [2] and I. Hussainova [1,*]

[1] Department of Mechanical and Industrial Engineering, Tallinn University of Technology, Ehitajate 5, 19086 Tallinn, Estonia; sofiya.aydinyan@taltech.ee

[2] Multi-Scale Additive Manufacturing Laboratory, Department of Mechanical and Mechatronics Engineering, University of Waterloo, 200 University Ave., West Waterloo, ON N2L 3G1, Canada; ehsan.toyserkani@uwaterloo.ca

* Correspondence: tatevik.minasyan@taltech.ee (T.M.); irina.hussainova@taltech.ee (I.H.)

Received: 10 September 2020; Accepted: 27 October 2020; Published: 29 October 2020

Abstract: $Mo(Si_{1-x},Al_x)_2$ composites were produced by a pulsed laser reactive selective laser melting of $MoSi_2$ and 30 wt.% AlSi10Mg powder mixture. The parametric study, altering the laser power between 100 and 300 W and scan speed between 400 and 1500 mm·s^{-1}, has been conducted to estimate the effect of processing parameters on printed coupon samples' quality. It was shown that samples prepared at 150–200 W laser power and 400–500 mm·s^{-1} scan speed, as well as 250 W laser power along with 700 mm·s^{-1} scan speed, provide a relatively good surface finish with 6.5 ± 0.5 µm–10.3 ± 0.8 µm roughness at the top of coupons, and 9.3 ± 0.7 µm–13.2 ± 1.1 µm side surface roughness in addition to a remarkable chemical and microstructural homogeneity. An increase in the laser power and a decrease in the scan speed led to an apparent improvement in the densification behavior resulting in printed coupons of up to 99.8% relative density and hardness of ~600 HV1 or ~560 HV5. The printed parts are composed of epitaxially grown columnar dendritic melt pool cores and coarser dendrites beyond the morphological transition zone in overlapped regions. An increase in the scanning speed at a fixed laser power and a decrease in the power at a fixed scan speed prohibited the complete single displacement reaction between $MoSi_2$ and aluminum, leading to unreacted $MoSi_2$ and Al lean hexagonal $Mo(Si_{1-x},Al_x)_2$ phase.

Keywords: molybdenum disilicide; aluminum alloy; additive manufacturing; laser powder bed fusion; molybdenum aluminosilicide; parametric study; surface roughness; hardness; density

1. Introduction

The research interests for metal silicides have continuously revolved around the development of a composite material with sufficient operating temperatures thresholds employable in applications across the lucrative aerospace and energy production sectors [1]. $MoSi_2$ is an attractive transition metal silicide for structural applications at elevated temperatures as it possesses an outstanding oxidation resistance up to 1700 °C [2], increasing with temperature electrical resistivity, which makes the material to be considered as a promising heating element [3]. Moreover, $MoSi_2$ exhibits an excellent alloying compatibility when paired with some compounds including metals [4,5], silicides [6], and ceramics [7]. Aluminum is one of the alloying elements negating the pest oxidation of $MoSi_2$ through the formation of alumina (or mullite) due to the development of the $Mo(Si,Al)_2$ compound [8–10]. Manufacturing of $Mo(Si,Al)_2$ composites into bulks is a challenging task with the conventional press and/or sintering methods; however, additive manufacturing techniques, which offer flexible fabrication, are prone to overcome many obstacles.

The laser powder bed fusion (LPBF)/selective laser melting (SLM) technique, a class of additive manufacturing (AM), enables the construction of intricately shaped objects. LPBF offers design freedom, while mitigating the problems associated with traditionally produced complex shapes [11]. The technique uses a 3D computer-aided design blueprint constructing 2D cross section slices of the model. As a powder distribution system evenly spreads a thin layer of powder on the build area, a high-power laser selectively melts the powder zones provided by an execution build file, which references consecutive layers of computer-aided design (CAD) model. Each laser cycle produces a new cross section slice of the constructed object; the work platform is incrementally lowered before a new powder layer is spread. The various processing parameters influence the microstructure, mechanical, and even chemical properties of the fabricated parts, which are related to (i) laser (wavelength, power, spot diameter, focal length, transverse electromagnetic mode, beam shape, pulse duration, and pulse repetition rate (if a pulsed laser is used)) [12], (ii) scan (speed, scanning pattern, scan line space, and scanning angle change) [13], (iii) feedstock (particle size, shape and distribution, packing density, layer thickness, powder flowability, melting point, chemical composition, laser absorptivity, etc. [14,15]), (iv) temperature (powder bed or feeder temperature) [15], (v) reaction chamber environment (inert gas type, pressure, flow rate, and direction) [16,17], (vi) build platform (material, melting point, thickness, possible reactivity with powder) [17], (vii) process setup (sample location, build angle, orientation) [18,19], (viii) powder reuse [20,21], and some others.

The effect of various parameters on the quality of LPBF-printed AlSi10Mg and $MoSi_2$-based items have recently been widely studied. The influence of scan path and gas flow rate on tensile properties of LPBF-printed AlSi10Mg parts using laser power of 350 W laser, a layer thickness of 100 μm, scanning speed of 900 mm·s^{-1}, and hatch distance of 120 μm was reported in [22]. It was shown that scanning against the gas flow nearby a gas outlet and an increase in gas flow rate improve the tensile properties of the material. The optimization of process parameters is given in [23]. The minimal porosity of 0.8% for AlSi10Mg samples was achieved at 175–200 W laser power, 1025–1350 mm·s^{-1} scan speed, and 50–65 μm hatch distance. As aluminum is a highly reflective metal and possesses a high thermal conductivity, a high enough laser power has been recommended for use [16].

The AlSi10Mg single tracks were produced by LPBF at a fixed laser power of 180 W and a layer thickness of 35 μm and scanning speed altered in 600 to 1600 mm·s^{-1} range [24]. The fully dense sample was fabricated only at a scanning speed of 1000 mm·s^{-1}. In [25], the preparation of $MoSi_2$ 10–13 wt.% Si composite lattices applying 36–84 W of laser power and low 80 mm·s^{-1} scan speed was reported. Manufacturing of $MoSi_2$ bulks using 100 W laser power and 400–1200 mm·s^{-1} scanning speed showed that the volume fraction of voids enlarged with an increase in the scanning speed hindering the continuous growth of grains along the building direction [26]. The authors' previous paper [27] reports on a successful reactive powder bed fusion of Mo–Si–AlSi10Mg alloy applying 100 W laser power and 300–500 mm·s^{-1} scanning speed yielding at preparation of almost fully dense $Mo(Si_{1-x,}Al_x)_2$ based composite.

In our previous work [28], we reported the in situ preparation of $Mo(Si,Al)_2$-based composite bulks by selective laser melting of a $MoSi_2$-30 wt.% AlSi10Mg powder mixture covering the powder characteristics, printability, and phase composition of the produced bulks. The main goal of this work is to analyze the impact of process parameters on surface roughness, densification behavior, hardness, and microstructure development of the printed parts to identify the optimum processing window for an efficient materials fabrication. The parametric study considers the laser power and scanning speed as variables of primary importance, which strongly influence the microstructure, surface roughness, and mechanical properties of the samples. Therefore, the current study is mostly concentrated at these parameters leaving other process variables out of scope. The motivation behind the work is the preparation of molybdenum aluminosilicide-based samples with high relative density, low surface roughness, microstructural and compositional homogeneity, as well as sufficient hardness to be used as a structural material or a heating element.

2. Experimental

The powder mixture of $MoSi_2$ and 30 wt.% AlSi10Mg was used as a feedstock for LPBF process. $MoSi_2$ powder was prepared by combustion synthesis of stoichiometric Mo–Si reactant mixture (Mo:Si; 1:2 molar ratio), then mixed with 30 wt.% commercial AlSi10Mg alloy powder by mechanical mixing for 3 h as reported in [28]. Particle size distribution, packing density, and basic flowability energy of the powder are detailed in [28]. Powder cohesion and the flowing angle were measured by GranuDrum (GranuTools, Awans, Belgium). The powder was half filled into the drum rotating around its axis at 2–10 rpm angular velocity. Images were captured after each rotation. The position of air/powder interface or the angle of repose was determined by an edge detection.

A Renishaw AM400 customized machine (Renishaw, Wotton-under-Edge, UK) was used for the consolidation of $MoSi_2$-30 wt.% AlSi10Mg mixture. The device possesses an effective build volume (X × Y × Z) of 250 mm × 250 mm × 300 mm and is equipped with a Gaussian distributed ytterbium continuous wave laser with a maximum power of 400 W and wavelength of 1070 nm, modulated to operate as a pulsed laser. Prior to laser initiation, the chamber was filled with argon gas with the oxygen level lower than 500 ppm. A meander scan pattern was used, and the scanning angle was interchanged by 67° upon the antecedent layer. Cylindrical samples with 7 mm × 7 mm were built on a reduced size (100 mm (X) × 100 mm (Y)) aluminum platform. For the parametric study, two parameters, namely, the laser power (P) and scan speed (v), were altered. The laser spot size and hatching distance (h) were maintained at 85 µm and 90 µm, respectively, while the laser power was changed from 100 W to 300 W with the step size of 50 W. The beam spot diameter at the focused position was 70 µm. To get a beam spot diameter of 90 µm, the focal point of the laser beam was defocused to a point above the build plate of the system. Point distance was chosen 85 µm and exposure time accordingly to achieve 400–1500 mm·s^{-1} scan speed (v). All samples were built using a Z vertical increment of 35 µm (layer thickness (d)). The built rate and the laser volumetric energy density (LVED) were derived from $BR = vhd$ and $E = P/vhd$ equations, respectively. The labels for each sample, the scheme of the corresponding process parameters based on the laser power, scanning speed and the corresponding energy density and build rate are depicted in Figure 1. Three samples were prepared under each condition and subjected for further investigation.

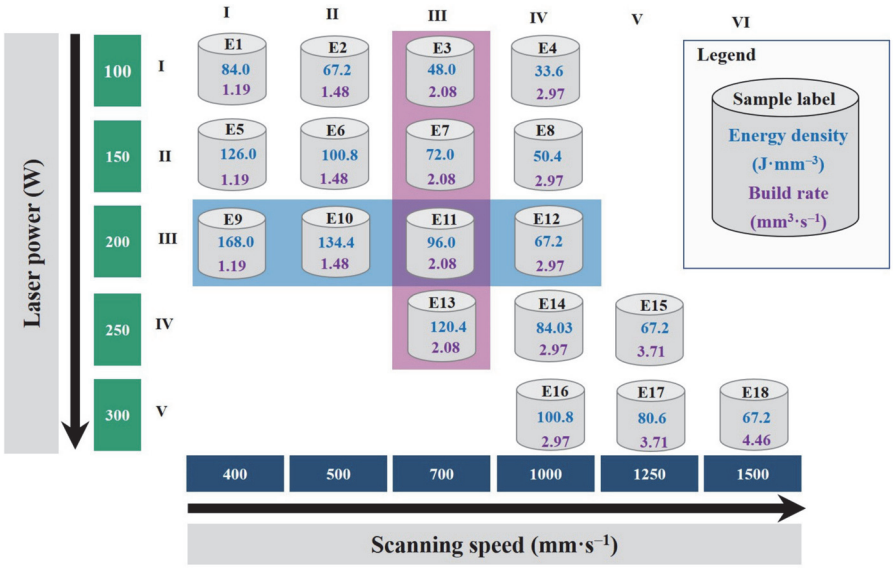

Figure 1. Scheme of used parameters according to scan speed and laser power (Note: The samples highlighted with background blue and purple colors are subjected to microstructural analysis).

The dimensional accuracy by means of surface roughness was estimated by Keyence VK-X250 laser scanning microscope (Keyence Corporation, Osaka, Japan) using 20× lens. Four measurements were performed for each surface, and the average values of the maximum height (Sz) and the arithmetical mean height (Sa) were taken.

Two scanning electron microscopes (SEM)—TESCAN VEGA3 (Brno, Czech Republic) and HR-SEM Zeiss Merlin (ZEISS, Oberkochen, Germany) equipped with Bruker QUANTAX 200 and Bruker EDX-XFlash 6/30 (Billerica, MA, USA) EDS detectors, respectively, were used to examine the morphology and chemical composition of the initial powder, as well as the microstructural development in as-built and polished parts.

The phase composition analysis was performed by Rigaku SmartLab SE X-ray diffractometer (Tokyo, Japan) (with CuKα radiation, λ = 1.54056 Å), with 1D detector D/teX Ultra 250. Samples were analyzed at 20–100° 2θ range, 0.01° step size, and 2.5°·min^{-1} measuring speed, using Bragg–Brentano geometry.

Additionally, the splashed powders during laser scanning were studied, as it has a critical role in process outcome. The blown powders located close to the gas outlet were collected after the completion of the whole process and analyzed.

The density of the fabricated specimens was measured by Archimedes' method (Mettler Toledo ME204, Greifensee, Switzerland) and by calculating samples' dimensions (by digital Vernier caliper, KS Tools Werkzeuge-Maschinen GmbH, Hessian, Germany, 0.01 mm accuracy) and weight. Relative density was calculated by taking the materials' bulk density as 4.37g·cm^{-3}.

The hardness was measured at different locations using a Vickers microhardness tester (Indentec 5030 SKV, Stourbridge, UK) with 1 kg and 5 kg loads (9.8 N and 49 N) and 10 s dwell time.

3. Results and Discussion

3.1. Feedstock Powders

Powder feedstock represents 70 wt.% $MoSi_2$ and 30 wt.% AlSi10Mg mixture (Figure 2c) with a negatively skewed Gaussian size distribution (D10 = 7.68 μm, D50 = 33 μm, D90 = 54 μm). AlSi10Mg alloy contains spherical and occasional satellite particles with Gaussian size distribution centered on 38 μm (Figure 2a).

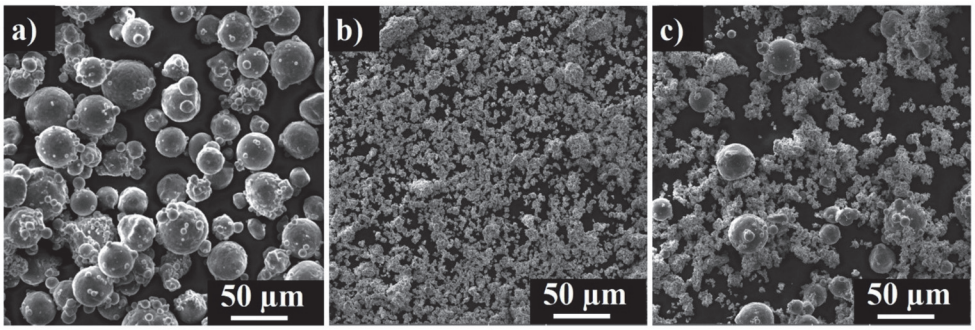

Figure 2. SEM images of AlSi10Mg alloy (**a**), $MoSi_2$ (**b**), and $MoSi_2$-30 wt.% AlSi10Mg powder mixture (**c**).

The $MoSi_2$ powder displays 1–5 micron-sized $MoSi_2$ particles with frequent agglomerates (D50 = 18 μm) (Figure 2b).

The angle of repose at 2 and10 rpm drum cell rotation speed was 44.85° and 45.5°, respectively. The cohesion was measured to be 13.25–14.25 highlighting the fair flowability of the powder and applicability for the LPBF process.

3.2. Surface Roughness

Figure 3 shows the top (a) and side surface profiles (b) of samples E5, E6, E9, E10, E13, and E16. The average top surface roughness (Sa) and the maximum height (Sz) are presented in Figure 4. The S_z is defined as the sum of the largest peak height and the largest pit depth values within the target areas. The zero level is based on the mean plane. SLM fabrication quality and surface integrity vary significantly depending on different process parameters.

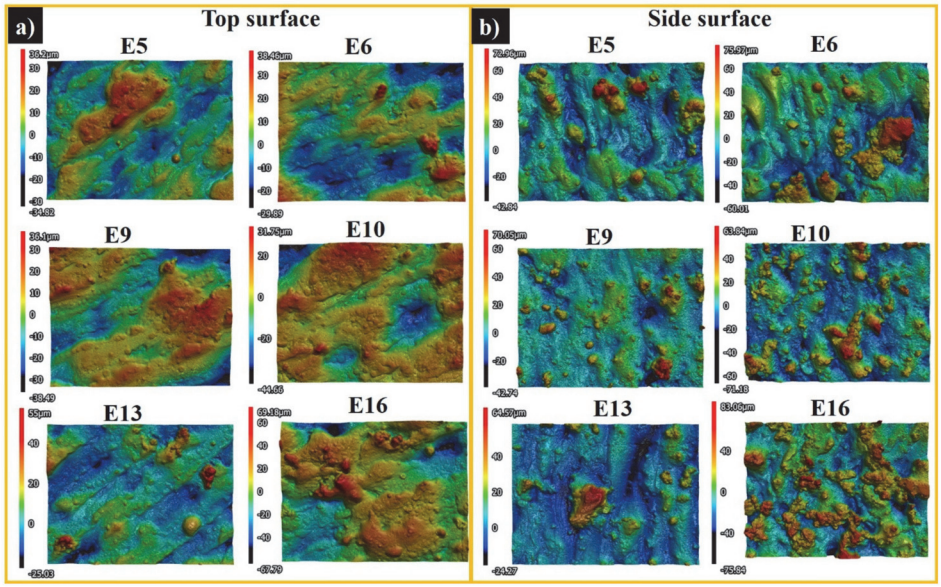

Figure 3. Top (**a**), and side (**b**) surface profiles of samples E5, E5, E9, E10, E13, and E16.

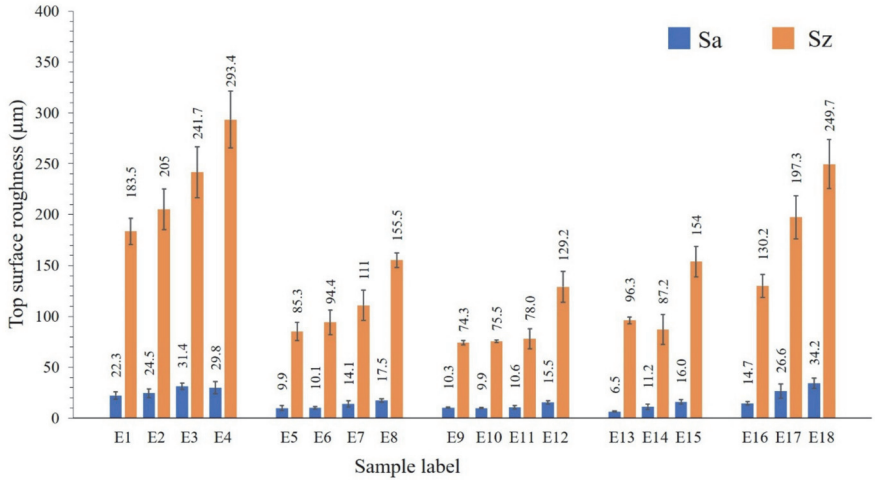

Figure 4. Top surface roughness results of samples E1–E18.

An increase in the scanning speed at a fixed laser power leads to an increase of top surface irregularities and affects the dimensional precision of fabricated parts. This is mainly attributed to the fact that at a higher scanning speed, the likelihood of balling phenomenon, and insufficient fusion

could be higher; both resulting in a poor surface quality. However, at the same scanning speed, the samples produced with a higher laser power possess smoother surfaces (e.g., samples E1–E5–E9 and E4–E8–E12) (Figure 4).

The samples produced using the lowest laser power of 100 W (E1–E4) have deep pits and high peaks. This may be conditioned by an insufficient heat for complete melting of consecutive layers causing major "lack of fusion" zones. In this case, the pattern of the scan track is not formed and the portion of the scanned powder layer remains in sintered condition. Moreover, when the powder layer is not completely melted, some of the powder particles become irregular in shape and larger in size, surpassing the set layer thickness and preventing the homogeneous spread of the subsequent virgin powder layer. The thickened layers increase the instability of the pool, weakening the bonding of the pool and the substrate, meantime promoting the balling effect. As a result, as the part fabrication is beyond the melting zone, the relative density and surface quality of LPBF-produced E1–E4 parts are low.

From the top surface profiles of E6 and E13 (Figure 3a), the laser scanning tracks are clearly visible. There are spherically shaped spattered particles at the surfaces of samples E5 and E13, which can potentially be either (i) surface oxidized Al alloy from the initial powder or heat affected zones, (ii) splashed droplets from the melt pool, or (iii) droplets spattered from other printed samples during laser scanning. Because of instability of the melt and an inevitable oxidation phenomenon during the melting process, the melted mass is not sufficiently wetting the underlying layer, which results in a rough surface finish, subsequently obstructing a smooth layer deposition and decreasing the density of the produced part [29].

In all probability, the use of higher laser powers and high scan speeds, such as 150–250 W/1000–1250 mm·s^{-1} or 300 W/1000–1500 mm·s^{-1} (Figure 1, samples in columns iv–vi), the balling phenomenon may occur due to capillary and wetting forces between the partially and fully melted particles interfaces.

Relatively smooth top surfaces were built for samples E5, E6, E9, E10, E11, and E14, as Sa was measured to be in the 9 to 11 μm range. The lowest Sa was estimated for the sample E13 (6.5 ± 0.5 μm). When the laser heats the powder layer, there is an obvious temperature difference among the laser beam and the scanned area. This induces shear forces on the molten mass surface, which is counteracted by surface tension forces [30]. After scanning the selected zone, the heat source moves, and the temperature evenly dissipates through the samples. The gravity force and the curved surface then neutralize the external shear force reinstating the leveled surface height of the melt pool. Due to an extended solidification time, this relaxation process will complete with a smooth surface finish [30].

A gradual increase is observed for Sz value when the scanning speed is increased, and the laser power is kept constant (Figures 1 and 4 samples in I–V rows).

Samples E9, E10 and E11, which are produced at 200W laser power and 400–700 mm·s^{-1} scanning speed, demonstrate the low Sa and Sz values. Sample E16 is produced using the highest laser power of 300 W; nonetheless, the surface finish is mediocre as compared to E9–E11 samples. This is associated with (i) the capillary effect and wetting forces changing the thermal domain, as when capillary force is not high enough to grab the particles inside the melt pool, the particles partially melt on the skin, and (ii) fast solidification and an insufficient relaxation time of the melt pool, enduring rippling on the surface and deterioration of surface quality.

Some other factors, such as leveled powder spreading, unchangeable effective spot diameter, and oxygen level in the chamber, are also decisive to secure a stable manufacturing process.

Analogous to the top surfaces, the samples' side surfaces produced using 100 W laser power show the enlarged roughness (Figure 5). A higher laser power and a lower scanning speed result in a higher quality of side surface, supposing a complete melting/sintering of the outer surfaces. The poor side surface roughness of samples E1–E4 is determined by the incomplete melting of the outer layers. If the outer powder layer is not completely melted/sintered, then the partially melted or unmelted particles may remain attached to the surface. However, in case of a high applied energy density, there

are incidences of adhesion of feedstock particles from the partially heated belts occasioning a high surface roughness.

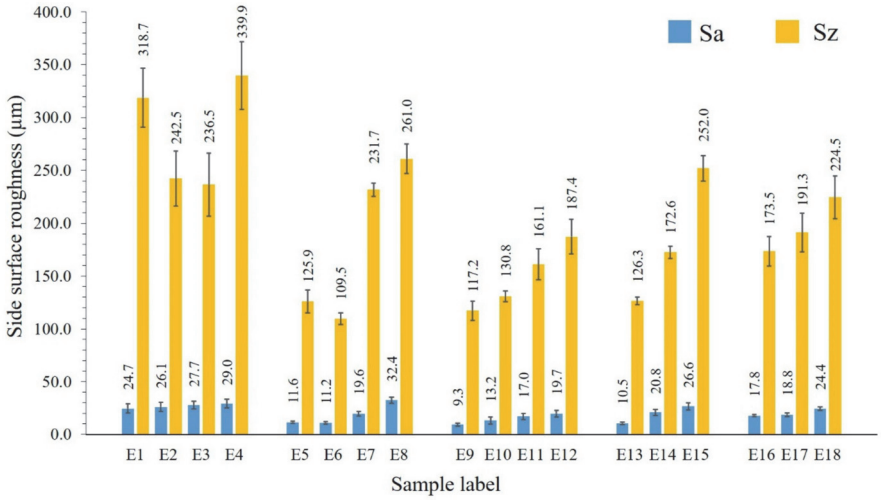

Figure 5. Side surface roughness results for samples E1–E18.

Sa represents the difference of every point's height in comparison with the arithmetical mean of the surface in the definition area. The low Sa and Sz values are measured for samples E5, E6, E9, E10, and E13 to be in the range of 9.3 to 13.2 μm and 109.5 to 139.8 μm, respectively (Figure 5). Samples printed using 300 W laser power possess comparatively high Sa and Sz values, due to the high number of adhered particles. For the sample E14, a relatively higher laser power was used, which favors the adherence of the powders from the heat affected zones, and relatively high scan speed, decreasing the applied energy per volume. This might cause insufficient fusion of the powder in outer boundary. For E11, as well, the reason of higher side surface roughness can be explained by the attached particles from a powder bed and insufficient heat provided for melting the powder in the outer boundary. As compared to the top surface, the roughness of the side surface is doubled. The adhered particles from the heat affected zone influence not only the maximum height, but also the arithmetical mean height, as demonstrated by this case.

Therefore, the parameters of 150–200 W along with 400–500 mm·s^{-1} scanning speed and 250 W laser power with 700 mm·s^{-1} provide a relatively good surface finish with moderate surface roughness.

Additional studies were made to find out the nature of spattered particles, as they were detected in both top and side surfaces of samples (Figure 3a,b). They were collected from the left side of the chamber. Apparently, the right surfaces of the samples are more vulnerable to a higher roughness, as gas flows from right to left blowing away the debris (Figure 6h,i). The SEM images of the spattered powders display that the particles became more acicular in shape and about 1.5–2 times bigger in size (Figure 6a,b) as compared to the virgin powder. The presence of oxygen was detected in the range of 4–11% by EDS. Moreover, Mo, Al, and Si contents have been reduced because of increased oxygen content. The change in powder composition disturbed the balance of Mg amount, as well.

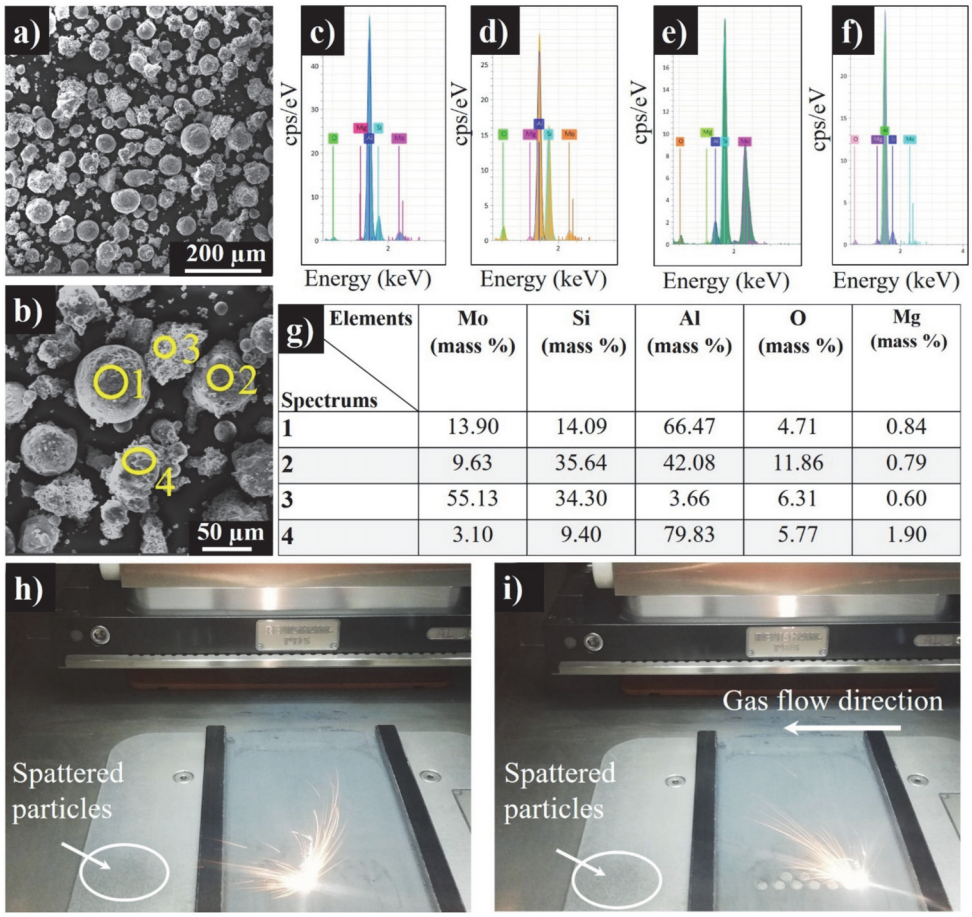

g)

Spectrums \ Elements	Mo (mass %)	Si (mass %)	Al (mass %)	O (mass %)	Mg (mass %)
1	13.90	14.09	66.47	4.71	0.84
2	9.63	35.64	42.08	11.86	0.79
3	55.13	34.30	3.66	6.31	0.60
4	3.10	9.40	79.83	5.77	1.90

Figure 6. SEM images of spattered powder (**a**,**b**), corresponding EDS spectrums (**c**–**f**), chemical composition of spattered particles 1–4 (**g**), and the spattering observed during the process (**h**,**i**) (Note that the gas flow direction is from the right to the left side of the chamber.).

Theoretically, the spherical particles are expected to be originated from the molten AlSi10Mg droplets, and the irregular-shaped ones from $MoSi_2$ powder splashing. Spectrums 1–4 (Figure 6c–f) confirm the above-mentioned statement, as the particles of rounded morphology have the high content of aluminum (Figure 6b–f). According to Spectrum 3 (Figure 6e), "Particle 3" contains mostly Mo and Si together with a small amount of Al; however, it contains up to 6% oxygen pointing to the oxidation by residual oxygen in argon. The AlSi10Mg debris has a rough texture with the presence of surface oxides rich with Mg. Mg is also oxidizing due to its instability and has a high affinity towards oxygen [31].

3.3. Microstructural Analysis

The SEM images of top and side surfaces of as-built sample E9 (150 W, 400 mm·s^{-1}) and the unpolished side fracture are depicted in Figure 7. The distance between the center of the 2 scan tracks is approximately 90 µm, which corresponds to the set hatching space (85 µm).

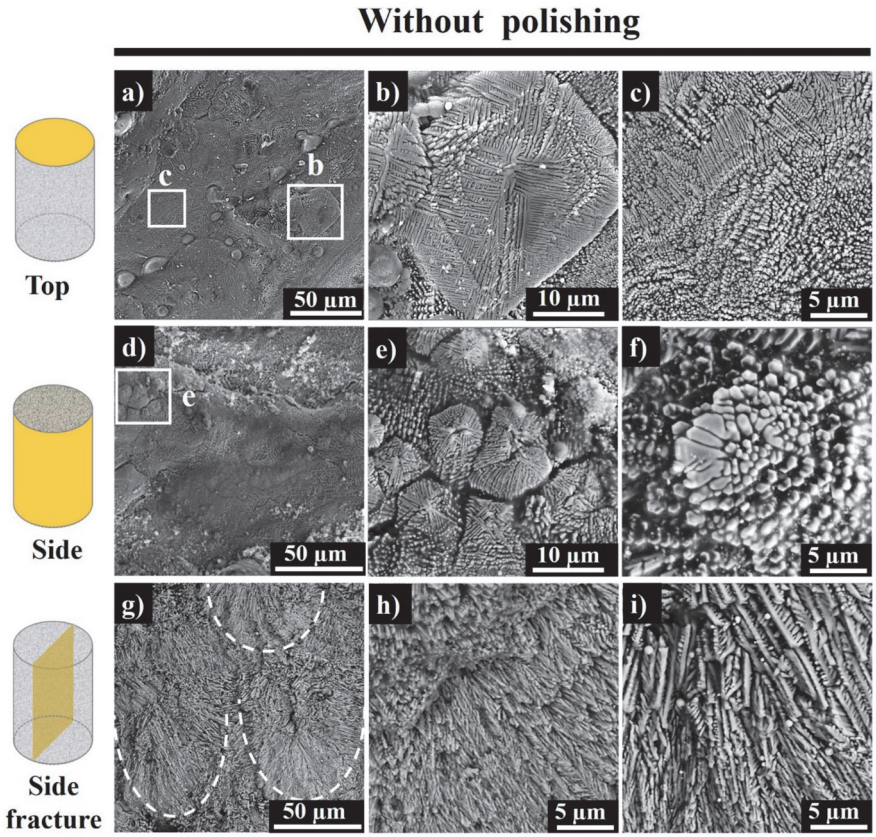

Figure 7. Top (**a**–**c**) and side (**d**–**f**) surface SEM images of as-built sample E9 and SEM images of unpolished side fracture (**g**–**i**) of E9 (white dashed ovals show the melt pools).

There are a few particles trapped in step edges, which represent the surface oxidized Al alloy particles (Figure 7a). Aluminum is susceptive to the formation of an alumina layer on the surface, which suppresses the melting procedure and subsequent wettability.

Each scanned region of sample E9 consists of fine submicron particles and columnar dendritic structures. These fine particles are the tips of columnar dendrites grown parallel to build direction, while the long dendritic structures are formed perpendicular to the build direction (Figure 7c). Thus, there is a change in dendritic growth direction in the top printed layer. Large equiaxed dendrites with around 20 µm were found on the samples' top surface (Figure 7b). Quite a few of the dendrites have secondary arms of 2–3 µm in size. The equiaxed dendritic crystals are originated from the undercooled molten mass when the latent heat of fusion is diffused across a cooler liquid forward to the intersection. Apparently, the temperature gradient is negative at the molten mass' interface, whereas in the solidified area, it is about zero [32].

Figure 7d–f shows the side surface morphology of the as-built sample E9 along with the build direction. Each printed layer is composed of fine particles and dendritic structures, which is similar to the observed ones on the top surface as well. "Star-like" equiaxed dendritic structures with 5–10 µm dimensions were found on each scanned layer along with fine particles, which might represent the tips of the long dendrites grown perpendicular to build direction.

Figure 7g–i shows the unpolished side fracture of sample E9. The area marked with white dashes illustrates the core of the melt pool with fine, columnar branched dendrites, while the surrounding

overlapped regions of adjacent and consecutive melt pools have the comparatively coarser columnar dendrites due to the melt pool overlapping.

Figure 8 shows the respective diffractograms of samples E13 and E3, when laser scan speed was fixed, but laser power was changed from 100 W to 250 W.

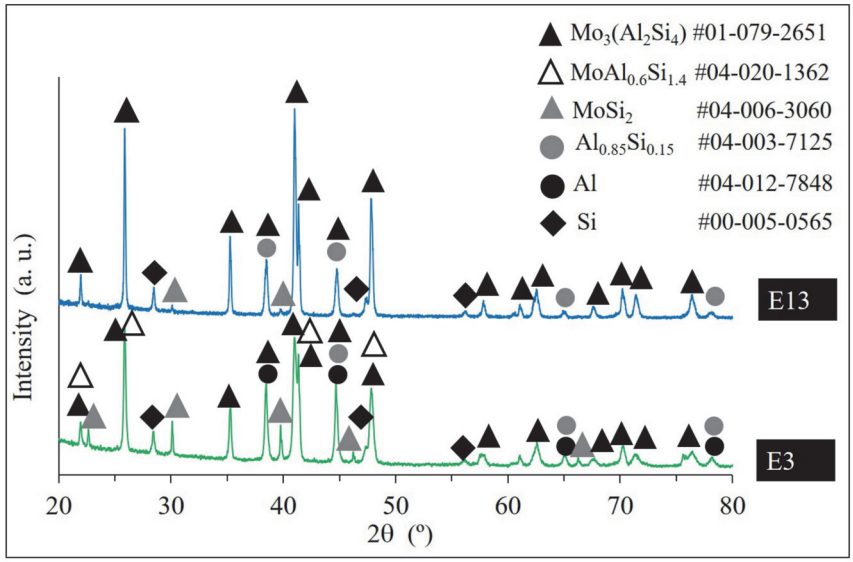

Figure 8. X-ray diffraction (XRD) patterns of samples E13 and E3.

The X-ray diffraction (XRD) pattern of E13 indicates the characteristic peaks of $Mo_3(Al_2Si_4)$ phase (corresponding to $Mo(Si_{1-x},Al_x)_2$ composition, $x = 0.33$) with substituted Si and formed $Al_{0.85}Si_{0.15}$ phase, and weak peaks of unreacted $MoSi_2$. In contrast to E13, the XRD pattern of E3 (laser power 100 W) shows that with a decrease in a laser power, the intensity of the unreacted $MoSi_2$ peaks increases. Moreover, the XRD analysis revealed the coexisting hexagonal C40 $Mo_3(Al_2Si_4)$ and $MoAl_{0.6}Si_{1.4}$ (corresponding to Al unsaturated $Mo(Si_{1-x},Al_x)_2$, x = 0.3) phases. Conclusively, in case of a higher laser power, the completion of a single displacement reaction of $MoSi_2$ and Al occurs and Al substitutes Si up to $x = 0.33$ mol.

The effect of the scanning speed increase exhibits a similar trend. For sample E12, some amount of unreacted $MoSi_2$ was detected, while in sample E9 remaining $MoSi_2$ was not observed. Accordingly, the high scan speeds combined with the low laser powers result in chemical inhomogeneity.

Figure 9 shows the top surface SEM images of samples E9–E12. The top view micrographs demonstrate long scan lines composed of elliptical cross sections of the melt pool cores from the sequence of printed layers (marked with white dashed ovals). The change in microstructure highlights the melt pools in Figure 9. For samples E9 and E10, the melt pool core solidification mode is observed to be mostly columnar dendritic together with periodically cellular dendrites. The solidification mode for E11 is cellular and cellular dendritic. For E12, differentiation of the melt pools is rather difficult. This is because the process was out of the melting zone and the powder was sintered. Both E11 and E12 demonstrate the heterogeneity in microstructure caused by a fast scanning and not complete chemical reaction between $MoSi_2$ and aluminum.

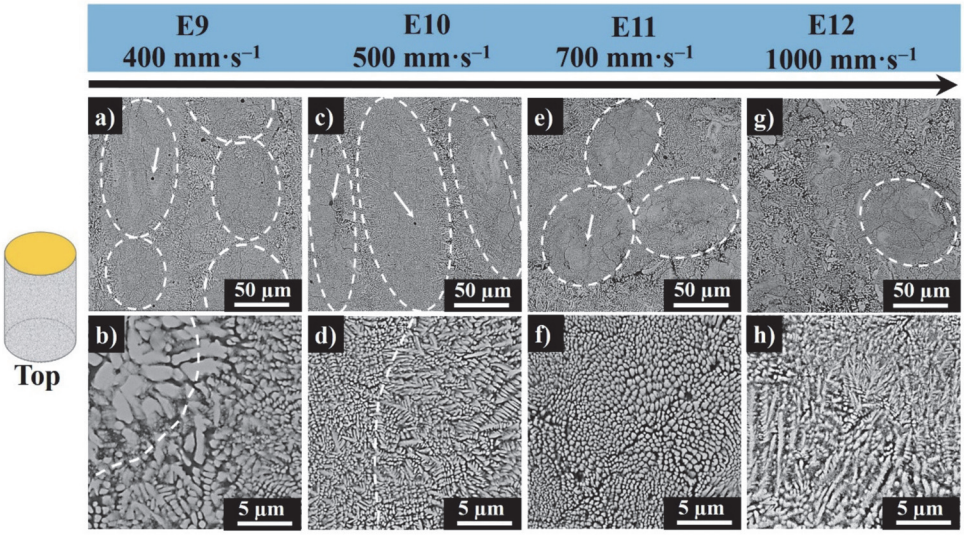

Figure 9. Top surface SEM images of E9 (**a**,**b**), E10 (**c**,**d**), E11 (**e**,**f**), and E12 (**g**,**h**) produced at 200W laser powers and at 400 mm·s^{-1}, 500 mm·s^{-1}, 700 mm·s^{-1}, and 1000 mm·s^{-1} scanning speed, respectively (white dashed ovals represent melt pool cores, the white arrow points the precipitates of Al–Si rich phase, white dashes in b and d highlight the morphology transition zones).

The melt pool cores in E9 represent the fine cellular or columnar dendrites of $Mo_3(Si_4Al_2)$ neighbored by a continuous network of hypoeutectic $Al_{0.85}Si_{0.15}$ in interdendritic regions, and Al has replaced the Si phase. In E10, the dendritic features are finer and, in E11, even smaller, conditioned by an increase in the scanning speed and a high cooling rate. The solidification mode of overlapping regions is columnar dendritic; thus, the core structure is enveloped with the coarser columnar dendritic crystals in the periphery.

The moving laser beam causes thermal gradients and growth rate variation in the center and the border of the melt pool, therefore the fineness of the $Mo_3(Al_2Si_4)$ grains in the core and the coarser grains at the border of the scan track as a higher cooling and solidification rates are associated with the core (see, e.g., Figure 9b,d). The columnar dendrites in E9 are misoriented, while in E10, they are well-oriented. The formation of columnar dendrites from cellular dendrites is affected by the thermal noise increase at the dendritic tips [33].

In all samples, fine and spherical precipitates of Al-Si rich phase of few micron size were observed (Figure 9, E9–E12, marked with white arrows). Moreover, form the top surface images, center-segregation of Al-Si rich phase was detected in the core of melt pools.

Figure 10 represents the side surfaces of E9–E12. The semi-elliptical white lines depict the melt pool centers along to "Z" direction and perpendicular to the scan direction. The white dashes in Figure 10b,d,f,g indicate the morphology transition zone. The side fracture images of E9 (produced at the highest LVED) (Figure 10, E9) show that the vertical cross sections of the melt pool cores consist of well-oriented ultrafine columnar dendrites with secondary branches and casual ternary arming is grown parallel to the build direction following the maximum thermal gradient along the build direction [34]. In E10, the melt pools become slightly broader in the X–Y direction and narrower in the X–Z direction. In E11, a similar trend is noticed, and in E12, the melt pools were difficult to differentiate. Therefore, it can be concluded that the increase in laser scanning speed at a fixed laser power leads to a decrease in melt pool depth, which weakens the bonding between the consecutive layers, causing lack of fusion defects. The cores of the melt pools in samples E9–E11 are ringed by coarser columnar

dendritic crystals in the overlapped areas of melt pool borders. The light gray regions found in sample E12 represent unreacted $MoSi_2$ phase, and the dark gray regions represent Al- and Si-saturated phase.

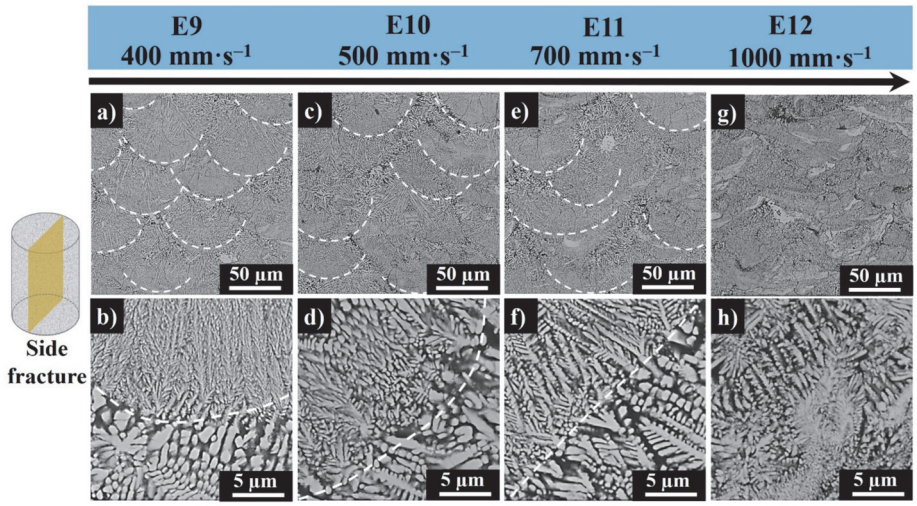

Figure 10. Side surface SEM images E9 (**a**,**b**), E10 (**c**,**d**), E11 (**e**,**f**), and E12 (**g**,**h**) produced at 200W laser powers and at 400 mm·s^{-1}, 500 mm·s^{-1}, 700 mm·s^{-1}, and 1000 mm·s^{-1} scanning speed, respectively (the white dashed semi-ovals in panels (**a**–**g**) represent melt pools, and the white dashes in panels (**b**–**f**) show the morphology transition zone from melt pool core to edges).

Figure 11 shows the top surface SEM images of samples E3–E13, where laser scanning speed was kept at the fixed value of 700 mm·s^{-1}, and the laser power was increased from 100 W to 250 W with 50 W step size. In E3 and E7 (produced at 100 W and 150 W laser power), different grain structures were observed ranging from cellular to equiaxed dendritic. The equiaxed dendrites mostly grow on the periphery of the melt pools due to incomplete melting of the previously spread powder layer. Fine round-shaped precipitates, highlighted by white arrows, were observed in sample E13, as well. As seen from Figure 11a–g, the microstructural homogeneity is improved with the increase in the laser power (from 100 W to 250 W).

The surface morphology of E13 represents the bimodal cellular and columnar dendritic structures. The columnar dendrites were nucleated and grown from the cellular grains due to the overlying of diffusive boundaries of cells leading to the dominance of columnar dendritic growth over the cellular ones.

Figure 12 shows the side fractures of samples E3–E13. For E3, the process went in a sintering mode as the apparent melt pool regions are not recognizable. For E7, the process went in a sintering/melting mode as the non-continuous melt pools are clearly visible. E11 and E13 have a more homogenous morphological texture as compared to sample E3 and E7. The finer regions (seen above a white dash line in Figure 12d–h) consist of fine columnar dendrites epitaxially grown parallel to the powder deposition direction. The region below the white dash is composed of the slightly disoriented coarser columnar dendrites.

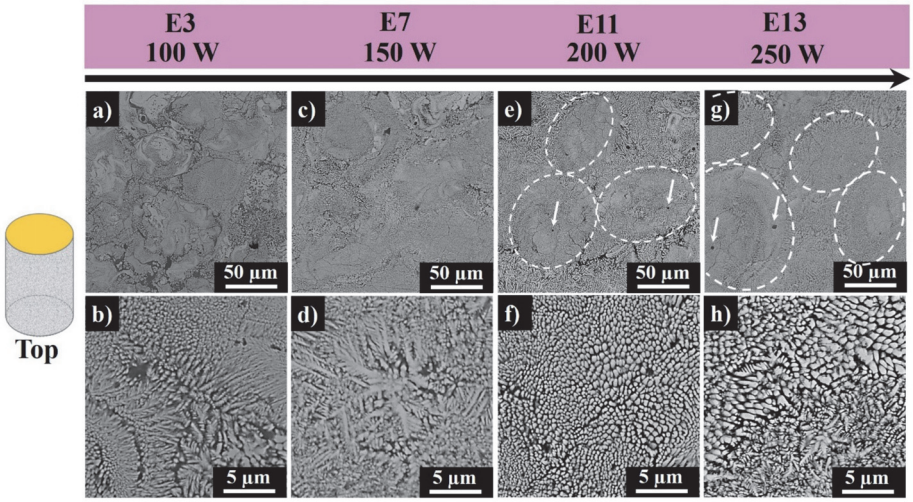

Figure 11. Top surface SEM images of sample E3 (**a**,**b**), E7 (**c**,**d**), E11 (**e**,**f**), and E13 (**g**,**h**) produced at 100 W, 150 W, 200 W, and 250 W laser powers, respectively, and at 700 mm·s^{-1} scanning speed (dashed ovals represent melt pool cores, and the white arrow points to the precipitates of Al–Si-rich phase).

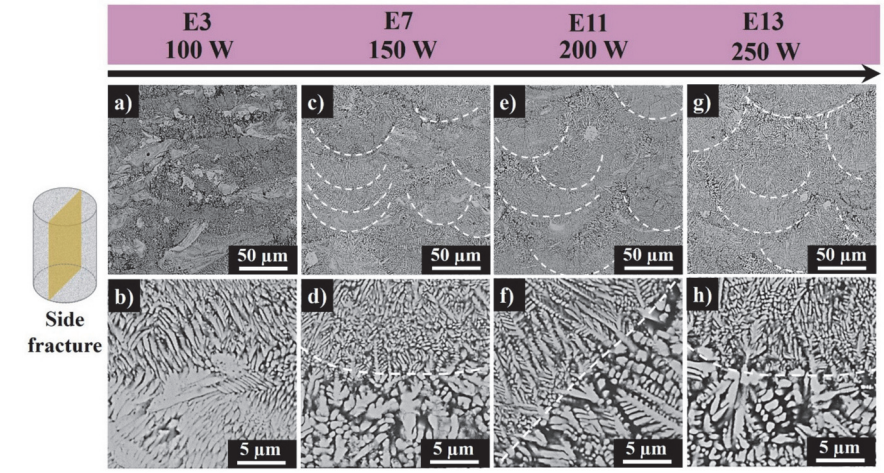

Figure 12. Side surface SEM images of sample E3 (**a**,**b**), E7 (**c**,**d**), E11 (**e**,**f**), and E13 (**g**,**h**) produced at 100 W, 150 W, 200 W, and 250 W laser powers, respectively, and at 700 mm·s^{-1} scanning speed (white dashed semi-ovals in panels (**c**–**g**) represent melt pools, and the white dashes in panels (**d**–**h**) show the morphology transition zone from melt pool core to edges).

Conclusively, samples E9 and E10 prepared at 200 W laser power and 400–500 mm·s^{-1} scanning speed and sample E13 prepared at 250 W laser power and 700 mm·s^{-1} scan speed, show homogenous top microstructure and clearly expressed melt pools in the side. Accordingly, these parameters were considered as optimal to achieve the microstructurally and compositionally homogeneous materials.

3.4. Density and Hardness

Figure 13 displays the geometric and Archimedes density values and the corresponding relative density results. For E3 and E4, the Archimedes density was not evaluated because of the huge amount

of open porosity. An increase in the scan speed in all five sets results in a gradual decrease in density, as the applied volumetric energy decreases with an increase in the scan speed (Figure 13).

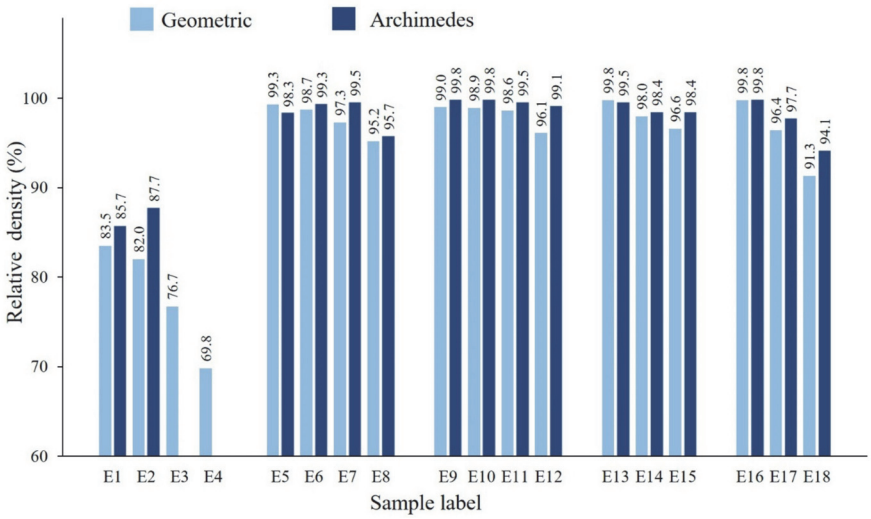

Figure 13. Relative geometric and Archimedes density results of E1–E18 samples (standard deviation is in the 0.1–0.4% range).

For the samples in columns I–V, Figure 1, where the laser power is increased with a step size of 50 W, the density is gradually increased, as the applied energy promoted the complete melting of the deposited layers and the sufficient bonding between consecutive layers.

Samples E15, E17, and E18 produced using the high scanning speeds (1250–1500 mm·s^{-1}), have a relatively low density being almost insensitive to the laser power, nonetheless greatly dependent on the scan speed. Moreover, though samples E2, E12, E15, and E18 were produced using the same LED (67.2 J·mm^{-3}), but sample E2 demonstrates the least densification followed by sample E18.

By optimizing process parameters samples possessing up to 99.8% relative density were manufactured.

It is well documented that the hardness depends not only on density, but also on developed phases; solidification mode; and respective microstructure of phase constituents, grain size, morphology, and phase segregation [35,36]. To ensure the reliability of hardness results, both HV1 and HV5 were taken into consideration.

Because of high porosity, the hardness of samples E1–E4 (Figure 14) was not measured. Unreacted $MoSi_2$ remained during scanning is responsible for insignificant fluctuations in hardness measured for materials produced at the same laser power.

The standard deviation bars show the higher fluctuations in the HV1 results, because of the small size of indentation marks. The heterogeneous microstructure of E8 and E18 is responsible for a relatively low hardness of 500 ± 57 HV1. All other samples exhibit hardness of up to ~600 HV1 and ~560 HV5.

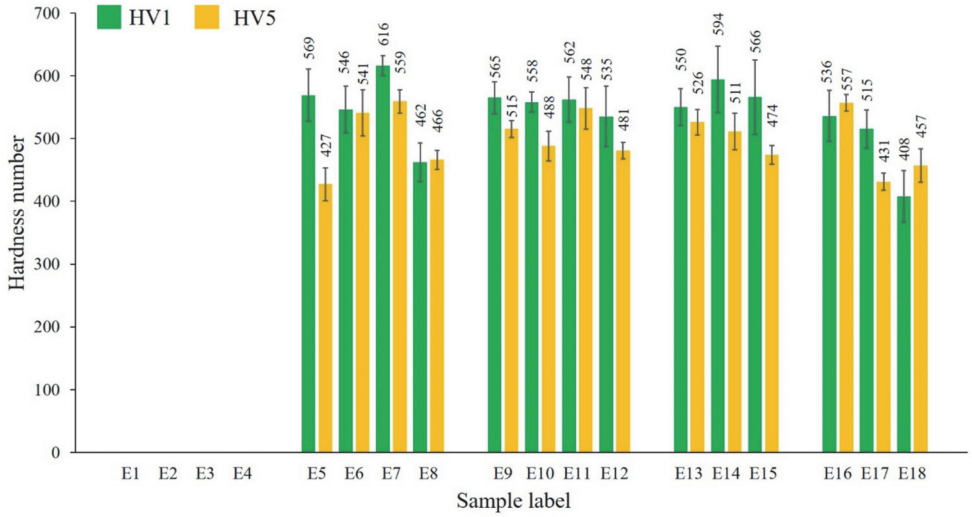

Figure 14. Hardness results of samples E1–E18, averaged for 10 indentations.

4. Conclusions

The composites of $Mo(Si_{1-x},Al_x)_2$, x = 0.3–0.33 mol, were successfully manufactured by reactive LPBF of fairly flowable $MoSi_2$-30 wt.% AlSi10Mg powder mixture.. The study of the process parameters in terms of laser power and laser scanning speed was performed to optimize the LPBF processing of mechanically reliable and microstructurally homogeneous materials for possible industrial applications where materials of high resistance to the pest oxidation are needed. The applied conditions were changed in the wide range of the laser power and the scanning speed of 100–300 W and 400–1500 mm·s^{-1}, respectively. It was shown that the samples produced at 150–200 W laser power and 400–500 mm·s^{-1} scanning speed, as well as at 250 W laser power and 700 mm·s^{-1} scanning speed, possess an admissible surface finish and the notable chemical and microstructural homogeneity. The longitudinal cross section analysis of the melt pools discloses the fine columnar dendritic structures of $Mo(Si_{1-x},Al_x)_2$ phase encircled with the coarser dendrites along with interdendritic hypoeutectic $Al_{0.85}Si_{0.15}$ phase and substituted Si. It was revealed that an increase in the laser scanning speed at a fixed laser power and a decrease in the laser power at a fixed scan speed result in the density reduction, as well as in the chemical and microstructural inhomogeneity.

The recommended LPBF process parameters (for the LPBF setup indicated in the experimental section of this paper) to produce the industrially applicable materials can be specified as the following.

- Laser power in the range of 150 to 250 W
- Scanning speed in the range of 400 to 700 mm·s^{-1}
- Layer thickness: 35 μm
- Hatching distance: 85 μm

Author Contributions: Conceptualization, I.H. and S.A.; methodology, T.M., S.A., and E.T.; software, T.M.; validation, I.H., S.A., and E.T.; formal analysis, T.M.; investigation, T.M.; resources, I.H. and E.T.; data curation, I.H.; writing—original draft preparation, T.M.; writing—review and editing, I.H., and S.A; visualization, T.M.; supervision, I.H. and S.A.; project administration, E.T. and I.H.; funding acquisition, I.H., and S.A. All authors have read and agreed to the published version of the manuscript.

Funding: This research was funded by the Estonian Research Council, grants PSG220 (S.A.) and PRG643. (I.H.).

Acknowledgments: This work was supported by the Estonian Research Council PSG220 (S.A.), PRG643 (I.H.). T.M. acknowledges the Archimedes foundation under the DORA + scholarship program for funding the travel visit to the University of Waterloo (Canada). The authors would like to thank Rainer Traksmaa for XRD analysis.

Conflicts of Interest: The authors declare no conflict of interest.

References

1. Pan, Y.; Wang, S. Insight into the oxidation mechanism of $MoSi_2$: Ab-initio calculations. *Ceram. Int.* **2018**, *44*, 19583–19589. [CrossRef]
2. Dai, L.; Yu, Y.; Zhou, H.; Yan, X.; Zhu, J.; Li, Y.; Wang, L. In-Situ synthesis of $MoSi_2$ coating on molybdenum substrate by electro-deoxidation of a SiO_2 layer in molten salt. *Ceram. Int.* **2015**, *41*, 13663–13670. [CrossRef]
3. Manukyan, K.V.; Aydinyan, S.V.; Kirakosyan, K.; Kharatyan, S.; Blugan, G.; Müller, U.; Kuebler, J. Molten salt-assisted combustion synthesis and characterization of $MoSi_2$ and $MoSi_2$-Si_3N_4 composite powders. *Chem. Eng. J.* **2008**, *143*, 331–336. [CrossRef]
4. Sun, S.; Li, X.; Zhang, Y.; Wang, H.; Yu, Y.; Jiang, Y.; Yi, D. Prediction of the mechanical properties of $MoSi_2$ doped with Cr, Nb and W from first-principles calculations. *J. Alloys Compd.* **2017**, *714*, 459–466. [CrossRef]
5. Zenk, C.; Gibson, J.S.-L.; Maier-Kiener, V.; Neumeier, S.; Göken, M.; Korte-Kerzel, S. Low temperature deformation of $MoSi_2$ and the effect of Ta, Nb and Al as alloying elements. *Acta Mater.* **2019**, *181*, 385–398. [CrossRef]
6. Xu, J.; Wu, H.; Li, B. Synthesis of $MoSi_2$/WSi_2 nanocrystalline powder by mechanical-assistant combustion synthesis method. *Int. J. Refract. Met. Hard Mater.* **2010**, *28*, 217–220. [CrossRef]
7. Han, X.-X.; Wang, Y.-L.; Xiong, X.; Li, H.; Chen, Z.-K.; Sun, W. Microstructure, sintering behavior and mechanical properties of SiC/$MoSi_2$ composites by spark plasma sintering. *Trans. Nonferrous Met. Soc. China* **2018**, *28*, 957–965. [CrossRef]
8. Meddar, L.; Magnien, B.; Clisson, M.; Roué, L.; Guay, D. Effect of Al addition on the microstructure and low-temperature reactivity to oxygen of pre-formed $MoSi_2$. *J. Mater. Sci.* **2012**, *47*, 6792–6800. [CrossRef]
9. Dasgupta, T.; Umarji, A. Thermal properties of $MoSi_2$ with minor aluminum substitutions. *Intermetallics* **2007**, *15*, 128–132. [CrossRef]
10. Zhang, H.; Long, C.; Chen, P.; Tang, G.; Liu, X. Synthesis and properties of $MoSi_2$ alloyed with aluminum. *Int. J. Refract. Met. Hard Mater.* **2003**, *21*, 75–79. [CrossRef]
11. Zhang, Z.; Huang, Y.; Kasinathan, A.R.; Shahabad, S.I.; Ali, U.; Mahmoodkhani, Y.; Toyserkani, E. 3-Dimensional heat transfer modeling for laser powder-bed fusion additive manufacturing with volumetric heat sources based on varied thermal conductivity and absorptivity. *Opt. Laser Technol.* **2019**, *109*, 297–312. [CrossRef]
12. King, E.W.; Anderson, A.T.; Ferencz, R.M.; Hodge, N.E.; Kamath, C.; Khairallah, S.A.; Rubenchik, A.M. Laser powder bed fusion additive manufacturing of metals; physics, computational, and materials challenges. *Appl. Phys. Rev.* **2015**, *2*, 041304. [CrossRef]
13. Jhabvala, J.; Boillat, E.; Antignac, T.; Glardon, R. On the effect of scanning strategies in the selective laser melting process. *Virtual Phys. Prototyp.* **2010**, *5*, 99–109. [CrossRef]
14. Brandt, M. (Ed.) *Laser Additive Manufacturing: Materials, Design, Technologies, and Applications*; Woodhead Publishing: Cambridge, UK, 2016; pp. 163–176.
15. Munir, K.S.; Li, Y.; Wen, C. Metallic scaffolds manufactured by selective laser melting for biomedical applications. In *Metallic Foam Bone*; Elsevier: Cambridge, UK, 2017; pp. 1–23.
16. Patel, S.; Vlasea, M. Melting modes in laser powder bed fusion. *Materialia* **2020**, *9*, 100591. [CrossRef]
17. Sames, W.J.; List, F.A.; Pannala, S.; Dehoff, R.R.; Babu, S.S. The metallurgy and processing science of metal additive manufacturing. *Int. Mater. Rev.* **2016**, *61*, 315–360. [CrossRef]
18. Esmaeilizadeh, R.; Ali, U.; Keshavarzkermani, A.; Mahmoodkhani, Y.; Marzbanrad, E.; Toyserkani, E. On the effect of spatter particles distribution on the quality of Hastelloy X parts made by laser powder-bed fusion additive manufacturing. *J. Manuf. Process.* **2019**, *37*, 11–20. [CrossRef]
19. Simonelli, M.; Tse, Y.Y.; Tuck, C. Effect of the build orientation on the mechanical properties and fracture modes of SLM Ti–6Al–4V. *Mater. Sci. Eng. A* **2014**, *616*, 1–11. [CrossRef]
20. Slotwinski, J.A.; Garboczi, E.; Stutzman, P.; Ferraris, C.F.; Watson, S.S.; Peltz, M.A. Characterization of Metal Powders Used for Additive Manufacturing. *J. Res. Natl. Inst. Stand. Technol.* **2014**, *119*, 460–493. [CrossRef]
21. Tang, H.P.; Qian, M.; Liu, N.; Zhang, X.Z.; Yang, G.Y.; Wang, J. Effect of Powder Reuse Times on Additive Manufacturing of Ti-6Al-4V by Selective Electron Beam Melting. *JOM* **2015**, *67*, 555–563. [CrossRef]

22. Anwar, A.B.; Pham, Q.-C. Selective laser melting of AlSi10Mg: Effects of scan direction, part placement and inert gas flow velocity on tensile strength. *J. Mater. Proc. Technol.* **2017**, *240*, 388–396. [CrossRef]
23. Read, N.; Wang, W.; Essa, K.; Attallah, M.M. Selective laser melting of AlSi10Mg alloy: Process optimisation and mechanical properties development. *Mater. Des.* **2015**, *65*, 417–424. [CrossRef]
24. Wei, P.; Wei, Z.; Chen, Z.; He, Y.; Du, J. Thermal behavior in single track during selective laser melting of AlSi10Mg powder. *Appl. Phys. A* **2017**, *123*, 604. [CrossRef]
25. Minasyan, T.; Liu, L.; Holovenko, Y.; Aydinyan, S.; Hussainova, I. Additively manufactured mesostructured $MoSi_2$-Si_3N_4 ceramic lattice. *Ceram. Int.* **2019**, *45*, 9926–9933. [CrossRef]
26. Hagihara, K.; Nakano, T.; Suzuki, M.; Ishimoto, T.; Suyalatu Sun, S.-H. Successful additive manufacturing of $MoSi_2$ including crystallographic texture and shape control. *J. Alloys Compd.* **2017**, *696*, 67–72. [CrossRef]
27. Minasyan, T.; Aydinyan, S.; Liu, L.; Volubujeva, O.; Toyserkani, E.; Hussainova, I. $Mo(Si_{1-x},Al_x)_2$-based composite by reactive laser powder-bed fusion. *Mater. Lett.* **2020**, *281*, 128776. [CrossRef]
28. Minasyan, T.; Aydinyan, S.; Toyserkani, E.; Hussainova, I. In Situ $Mo(Si,Al)_2$-Based Composite through Selective Laser Melting of a $MoSi_2$-30 wt.% AlSi10Mg Mixture. *Materials* **2020**, *13*, 3720. [CrossRef]
29. Wang, D.; Changhui, S.; Yang, Y.; Bai, Y. Investigation of crystal growth mechanism during selective laser melting and mechanical property characterization of 316L stainless steel parts. *Mater. Des.* **2016**, *100*, 291–299. [CrossRef]
30. Strano, G.; Hao, L.; Everson, R.M.; Evans, K.E. Surface roughness analysis, modelling and prediction in selective laser melting. *J. Mater. Process. Technol.* **2013**, *213*, 589–597. [CrossRef]
31. Aboulkhair, N.T.; Simonelli, M.; Parry, L.; Ashcroft, I.; Tuck, C.; Hague, R. 3D printing of Aluminium alloys: Additive Manufacturing of Aluminium alloys using selective laser melting. *Prog. Mater. Sci.* **2019**, *106*, 100578. [CrossRef]
32. Trivedi, R.; Kurz, W. Dendritic growth. *Int. Mater. Rev.* **1994**, *39*, 49–74. [CrossRef]
33. Tourret, D.; Karma, A. Growth competition of columnar dendritic grains: A phase-field study. *Acta Mater.* **2015**, *82*, 64–83. [CrossRef]
34. Basak, A.; Das, S. Epitaxy and Microstructure Evolution in Metal Additive Manufacturing. *Annu. Rev. Mater. Res.* **2016**, *46*, 125–149. [CrossRef]
35. Corrochano, J.; Lieblich, M.; Ibáñez, J. On the role of matrix grain size and particulate reinforcement on the hardness of powder metallurgy Al–Mg–Si/$MoSi_2$ composites. *Compos. Sci. Technol.* **2009**, *69*, 1818–1824. [CrossRef]
36. Soare, V.; Mitrica, D.; Constantin, I.; Badilita, V.; Stoiciu, F.; Popescu, A.-M.J.; Carcea, I. Influence of remelting on microstructure, hardness and corrosion behaviour of AlCoCrFeNiTi high entropy alloy. *Mater. Sci. Technol.* **2015**, *31*, 1194–1200. [CrossRef]

Curriculum vitae

Personal data

Name:	Tatevik Minasyan
Date of birth:	10.01.1994
Place of birth:	Armenia
Citizenship:	Armenia

Contact data

E-mail:	tatevik.minasyan@taltech.ee tatevik.minasyan@uwaterloo.ca tatminas@gmail.com

Education

2016–2020	Tallinn University of Technology – PhD
2014–2016	Yerevan State University – MSC
2010–2014	Yerevan State University – BSC

Language competence

Armenian	Native
Russian	Fluent
English	Fluent
Estonian	Good

Professional employment

01.01.2017–31.08.2018	Early-stage researcher, Tallinn University of Technology, School of Engineering, Department of Mechanical and Industrial Engineering, Tallinn, Estonia.
01.10.2016–31.12.2016	Early-stage researcher, Tallinn University of Technology, Faculty of Mechanical Engineering, Department of Materials Engineering, Tallinn, Estonia.
01.10.2014–31.08.2016	Laboratory assistant at the Institute of Chemical Physics of National Academy of Science of the Republic of Armenia.

Projects

IUT19-29 “Multi-scale structured ceramic-based composites for extreme applications (1.01.2014−31.12.2019)”, Jakob Kübarsepp, Tallinn University of Technology, Faculty of Mechanical Engineering, Tallinn University of Technology, School of Engineering, Department of Mechanical and Industrial Engineering.

PRG643 “Bio-replicating Engineering Structures for Tribo-applications (BEST) (1.01.2020−31.12.2024)”, Irina Hussainova, Tallinn University of Technology, School of Engineering, Department of Mechanical and Industrial Engineering.

PSG220 “Additive manufacturing of super-strong and lightweight ceramics for next generation high temperature compounds (1.03.2019−31.03.2023)”, Sofiya Aydinyan, Tallinn University of Technology, School of Engineering, Department of Mechanical and Industrial Engineering.

Patents

Invention: Self-functionalizing fibrous networks of Si_3N_4 with complex geometry and manufacturing thereof. Institution: Tallinn University of Technology. Authors: Le Liu, Tatevik Minasyan, Sofiya Aydinyan, Marina Aghayan, Irina Hussainova. Priority number: EP17174463.4. Priority date: 05.06.2017.

Invention: TiB_2 based complex structures by selective laser sintering. Institution: Tallinn University of Technology. Authors: Sofiya Aydinyan, Le Liu, Tatevik Minasyan, Irina Hussainova. Priority number: US62/677975. Priority date: 30.05.2018.

Invention: A method of direct laser shaping ceramic-intermetallic composites of $MoSi_2$ and/or $Mo(Si,Al)_2$ and Al and/or Al alloy. Institution: Tallinn University of Technology. Authors: Sofiya Aydinyan, Le Liu, Tatevik Minasyan, Irina Hussainova. Priority number: GB1908943.2. Priority date: 21.06.2019.

Research visits

07.11.2016–26.11.2016	Institute of Ceramics and Glass, Madrid, Spain
13.02.2017–13.03.2017	Institute of Ceramics and Glass, Madrid, Spain
02.04.2017–10.04.2017	Institute of Advanced Manufacturing Technology, Krakow, Poland
13.09.2017–19.09.2017	Institute of Advanced Manufacturing Technology, Krakow, Poland
10.09.2019–10.03.2020	University of Waterloo, Ontario, Canada

Elulookirjeldus

Isikuandmed

Nimi:	Tatevik Minasyan
Sünniaeg:	10.01.1994
Sünnikoht:	Armeenia
Kodakondsus:	Armeenia

Kontaktandmed

E-post:	tatevik.minasyan@taltech.ee tatevik.minasyan@uwaterloo.ca tatminas@gmail.com

Hariduskäik

2016–2020	Tallinna Tehnikaülikool – PhD
2014–2016	Jerevani Riiklik Ülikool – MSC
2010–2014	Jerevani Riiklik Ülikool – BSC

Keelteoskus

Armeenia keel	Emakeel
Vene keel	Kõrgtase
Inglise keel	Kõrgtase
Eesti keel	Hea

Teenistuskäik

01.01.2017–31.08.2018	Nooremteadur, Tallinna Tehnikaülikool, Inseneriteaduskond, Mehaanika ja Tööstustehnika Instituut, Tallinn, Eesti.
01.10.2016–31.12.2016	Nooremteadur, Tallinna Tehnikaülikool, Mehaanikateaduskond, Materjalitehnika Instituut, Tallinn, Eesti.
01.10.2014–31.08.2016	Laborant, Armeenia Vabariigi Riikliku Teaduste Akadeemia, Keemilise Füüsika Instituut.

Projektid

IUT19-29 “Mitmeastmeliselt struktureeritud keraamika-baasil komposiitmaterjalid kasutamiseks ekstreemtingimustes (1.01.2014−31.12.2019)”, Jakob Kübarsepp, Tallinna Tehnikaülikool, Mehaanikateaduskond, Tallinna Tehnikaülikool, Inseneriteaduskond, Mehaanika ja tööstustehnika instituut.

PRG643 “Biojäljendatud tehnostruktuurid triboloogilisteks rakendusteks (1.01.2020−31.12.2024)”, Irina Hussainova, Tallinna Tehnikaülikool, Inseneriteaduskond, Mehaanika ja tööstustehnika instituut.

PSG220 “Supertugeva ja kergekaalulise keraamika 3D printimine järgmise põlvkonna kõrgtemperatuursete materjalidena (1.03.2019−31.03.2023)”, Sofiya Aydinyan, Tallinna Tehnikaülikool, Inseneriteaduskond, Mehaanika ja tööstustehnika instituut.

Tööstusomand

Patentne leiutis: Self-functionalizing fibrous networks of Si_3N_4 with complex geometry and manufacturing thereof; Omanikud: Tallinna Tehnikaülikool; Autorid: Le Liu, Tatevik Minasyan, Sofiya Aydinyan, Marina Aghayan, Irina Hussainova; Prioriteedi number: EP17174463.4; Prioriteedi kuupäev: 5.06.2017.

Patentne leiutis: Meetod TiB_2-põhiste keeruka geomeetriaga detailide tootmiseks selektiivse laserpaagutuse abil; Omanikud: Tallinna Tehnikaülikool; Autorid: Sofiya Aydinyan, Le Liu, Tatevik Minasyan, Irina Hussainova; Prioriteedi number: US62/677975; Prioriteedi kuupäev: 30.05.2018.

Patentne leiutis: A method of direct laser shaping ceramic-intermetallic composites of $MoSi_2$ and/or $Mo(Si,Al)_2$ and Al and/or Al alloy; Omanikud: Tallinna Tehnikaülikool; Autorid: Sofiya Aydinyan, Le Liu, Tatevik Minasyan, Irina Hussainova; Prioriteedi number: GB1908943.2; Prioriteedi kuupäev: 21.06.2019.

Välismaal teadustöö

07.11.2016-26.11.2016	Institute of Ceramics and Glass, Madrid, Hispaania
13.02.2017-13.03.2017	Institute of Ceramics and Glass, Madrid, Hispaania
02.04.2017-10.04.2017	Institute of Advanced Manufacturing Technology, Krakow, Poola
13.09.2017-19.09.2017	Institute of Advanced Manufacturing Technology, Krakow, Poola
10.09.2019-10.03.2020	Waterloo Ülikool, Ontario, Kanada